Computational Studies of Enzymic Hydrogen Tunnelling

Thesis submitted for the degree of
Doctor of Philosophy
at the University of Leicester
by

Linus Johannissen

Department of Chemistry
University of Leicester, Leicester LE1 7RH

December 2006

UMI Number: U505931

UMI U505931

Abstract

The role of enzyme motions in hydrogen tunneling during catalysis is currently a very contentious subject. Experimental data, particularly of elevated kinetic isotope effects, has suggested a significant role for dynamics in the tunneling step. The importance of proton tunneling in the reaction catalysed by the heterotetrameric enzyme aromatic amine dehydrogenase (AADH) has been extensively studied both kinetically and computationally, and the availability of crystal structures for key reaction intermediates makes this an ideal system for studying the involvement of dynamics in catalysis. Multi-nanosecond molecular dynamics simulations revealed that the motions of the reacting groups are not correlated with motions within the enzyme, and that the overall motions of the donor and acceptor atoms are not focused towards each other. Nevertheless, certain key motions are required to achieve tunneling, and these were identified from spectral density analysis as corresponding to a $165 \, cm^{-1}$ promoting vibration. This vibration is not part of a large network of vibrations, but is instead inherent within the substrate, as confirmed by high-level frequency calculations of the isolated substrate. Comparing hybrid simulations of the heterotetramer and an isolated monomer of AADH revealed that this vibration is crucial for reducing the tunneling distance and the height of the barrier separating the reactant from product by moving the system up the potential energy surface. Numerical modelling of the experimental rates revealed that the promoting vibration is compatible with the reaction kinetics and compatible with the tunneling distance derived from a concomitant computational analysis, and that the presence or absence of such a vibration may not be easily identified experimentally. This represents the first example of a short-range oscillation acting as a promoting vibration, and opens the door to new experimental methods for studying enzymic tunneling and potentially for exploiting enzymes in biocatalysis by selectively exciting specific vibrational modes.

Acknowledgements

I would like to thank my supervisor Mike Sutcliffe, for all his help and support and, well, for just being a really good supervisor. I would also like to thank all the people I have collaborated with on in this project: the kineticists – Nigel, Jaswir, Parvi – the crystallographers – David, Anna – and my computational allies – Laura in Leicester and Adrian and Kara in Bristol. I also thank everyone from the multiple labs I have occupied over the last four years – I've had a great time. I am especially grateful to Jean-Didier for all his help on using lots of software which wasn't written with user friendliness in mind. I thank those people I've been hanging out with after moving to Manchester towards the end of this Ph.D., without whom my time in Manchester might have been better spent, but wouldn't have been so much fun, especially Chris for his help on the introduction and Sam for helping me wrap my head around some pretty complex theory.

Aside from the academics, I wish to thank all my friends, without whom the last four years would not have been so much fun. Thanks especially to Robin and Alison, Marc and Tasha, Emma and Peter for all their hospitality when I felt like visiting my London.

And finally, I would like to express my gratitude to all my family, especially my parents, for all their love and support over the years. But, in the words of those great French poets, "faudrais que j'invente des mots qui existent pas dans le dico".

Table of Contents

List of Figures

Chapter 4

Chapter 5

Chapter 6

Chapter 7

List of Tables

Abbreviations & Symbols

‡	Transition State
A	Arrhenius prefactor
Å	Ångström
AADH	Aromatic Amine Dehydrogenase
BSAO	Bovine Serum Amine Oxidase
cm^{-1}	Wavenumber, reciprocal of wavelength
ΔX	Change in parameter X
DCCM	Dynamical Cross-Correlation Map
DFT	Density Functional Theory
DFT	Discrete Fourier Transformation
DHFR	Dihydrofolate Reductase
E	Energy
E_a	Activation energy
E_X	Gating energy
F.C.	Franck-Condon
G	Gibbs free energy
h	Planck's constant
$\hbar$	h-bar, $h/2\pi$
HC	Hydrogen coordinate
HF	Hartree-Fock
HLADH	Horse Liver Alcohol Dehydrogenase
Ht-ADH	Thermophilic Alcohol Dehydrogenase
k	Rate constant
K	Kelvin
K	Thermodynamic equilibrium constant
KIE	Kinetic Isotope Effect
λ	Reorganisation energy
LCAO	Linear Combination of Atomic Orbitals
m	Mass
MADH	Methylamine Dehydrogenase
MC	Point of Minimum Coupling

MD	Molecular Dynamics
MEP	Minimum Energy Path
MM	Molecular Mechanics
MO	Molecular Orbital
MT	Multidimensional Tunneling
NAC	Near Attack Conformer
NAD	Nicotinamide Adenine Dinucleotide
NADH	Protonated NAD^+
NADPH	Nicotinamide Adenine Dinucleotide Phosphate
NDDO	Neglect of Diatomic Differential Overlap
NMA	Normal Mode Analysis
P	Product
PES	Potential Energy Surface
q	Environmental coordinate
QM	Quantum Mechanics
R	Universal gas constant
r	Distance
R	Reactant
RHF	Restricted Hartree-Fock
RMS	Root mean square
RTE	Representative Tunneling Energy
S	Entropy
SCT	Small Curvature Tunneling
SLO	Soybean Lipoxygenase
T	Absolute temperature (K)
TST	Transition State Theory
TTQ	Tryptophan Tryptophyl Quinone
ν	Frequency
VAF	Velocity Autocorrelation Function
VTST	Variational Transition State Theory
ω	Vibrational frequency
X	Gating coordinate
ZDO	Zero Differntial Overlap
ZPE	Zero Point Energy

1. Introduction

1.1. A Brief History of Models of Enzyme Catalysis

1.1.1. The Evolution of Transition State Theory

Enzymes are protein catalysts that achieve the greatest rate enhancements among all catalysts, up to a factor of 10^{21} (Lad *et al.* 2003), and in solution many of the reactions they catalyse would have half-times approaching the age of the earth (Wolfenden and Snider 2001). The precise methods by which enzymes achieve this tremendous feat are still far from understood, despite the tremendous evolution in our understanding of enzyme catalysis over the past 100 or so years. One of the first hypotheses was Emil Fischer's "lock and key" analogy (Fischer 1894). In this model, where the enzyme is the lock and the substrate the key, only a key of the correct size and shape can fit into the lock, and the reaction is promoted by the proximity of the reacting groups. To further explain how the substrate is activated, this model was later modified to one where "the key does not fit the lock quite perfectly but exercises a certain strain on it" (Haldane 1930). Further evolution of the model produced the "induced fit" model of enzyme catalysis (Koshland 1973; Bennet and Steitz 1978), in which the conformation of the enzyme changes in order to accommodate the substrate. In 1935 Eyring postulated the transition state theory (TST) to explain reactions in the gas phase, which later led to Pauling's hypothesis of enzyme-transition-state complementarity (Pauling 1948), in which the enzyme binds preferentially to the transition state, thus reducing the energy of the transition state relative to the reactant or product states. This model has been greatly successful, and is still used today as the text-book explanation for enzyme catalysis.

TST is the classical description of a chemical reaction, where the reactants and products are separated by a single, static potential energy barrier, at the top of which

lies the transition state, a high-energy configuration

with both reactant- and product-like character. To

be more specific, the overall phase space of the

system can be described by a potential energy

surface (PES) with the reactant lying in one

minimum and the product in the other, and the

transition state is a saddle point at the top of the
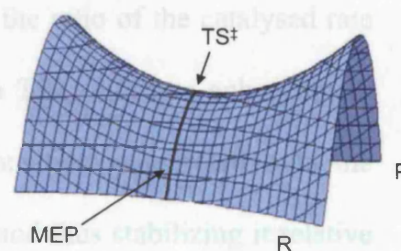
Figure 1.1. Illustration of a potential energy surface for a chemical reaction separating the reactant (R) and product (P) states. The transition state (TS‡) lies at the saddle point at the top of the minimum energy path (MEP).

minimum energy path (MEP) connecting the two (Figure 1.1). According to TST, the

rate of the reaction follows the MEP and can be described by the Arrhenius equation,

$$k = A \cdot \exp(-E_a / RT) \tag{1.1}$$

where k is the rate, E_a is the activation energy, R the universal gas constant, T the

temperature and the Arrhenius pre-exponential factor A is a system-specific constant.

Thus, the rate depends on the energy difference between the reactant and transition

states, and the energy of the system: the greater the temperature, the bigger the

probability of the system achieving the high-energy transition state configuration. The

activation energy for a reaction can be determined by converting Equation 1.1 to

$$\ln(k) = \ln(A) - \frac{E_a}{RT} \tag{1.2}$$

The activation energy can be obtained from a plot of $\ln(k)$ *versus* $1/T$, known as the

Arrhenius plot, where the gradient is equal to $-E_a/R$. The Arrhenius pre-factor can be

calculated from the y-intercept, $\ln(A)$.

The rate enhancement by catalysis is defined as the ratio of the catalysed rate to the uncatalysed rate in water at pH 7. According to TST, this rate enhancement achieved by reducing the potential energy of the transition state relative to the reactant, by binding more tightly to the transition state and thus stabilizing it relative to the reactant. For example, if the transition state has different electrostatic properties to the reactant, then the enzyme may stabilise it by the proximity of appropriately charged amino acids, which will complement the transition state more than the reactant.

Despite the appeal and success of this elegant model for enzyme catalysis, transition state complementarity is not the complete picture. For example, enzymes can raise the energy on the reactant side of the barrier (Jencks 1975; Wu *et al.* 2000) by deforming the reactants or promoting the formation of near attack conformers (NACs), thus reducing the energy difference between the reactant and the transition state. Furthermore, the potential energy barrier does not take into account the entropies of the reactant, transition state and product. A better representation of the barrier to the reaction is therefore the Gibbs free energy barrier:

$$\Delta G = \Delta H - T\Delta S \qquad (1.3)$$

where G is the Gibbs free energy, H the enthalpy and S the entropy. Transition state stabilisation can therefore also be achieved by an increase in the entropy at the transition state. The barrier height, $\Delta G^{\ddagger}$, is now the difference in free energy between the reactant and the transition state. The rate can be obtained from Equation 1.4, and the entropic and enthalpic contributions from Equation 1.5, the Eyring equation:

$$k = \frac{k_B T}{h} \cdot exp(-\Delta G^{\ddagger} / RT) \tag{1.4}$$

$$\ln(k / \mathrm{T}) = \ln(k_B / h) + \frac{\Delta S^{\ddagger}}{R} - \frac{\Delta H^{\ddagger}}{RT} \tag{1.5}$$

A poignant illustration of how enzymes employ the different tools at their disposal to lower the energy barrier is the recent comparison of two very similar intramolecular reorganisations catalysed by the enzymes chalcone isomerase and chorismate mutase (Hur and Bruice 2003). Molecular dynamics simulations revealed that these two enzymes use different approaches to catalysis. Chalcone isomerase speeds up the reaction relative to the reaction in water mainly by transition-state stabilisation, both by a stronger electrostatic interaction with a nearby amino acid and by an increase in entropy by the release of water molecules. Chorismate mutase, on the other hand, mainly uses the promotion of NACs to bring the energy of the reactant nearer to that of the transition state. The reason for these different approaches is that chalcone readily forms NACs in solution without the enzyme, while chorismate does not; on the other hand, the transition state of the chalcone reaction develops a partial charge which can be stabilised by a stronger electrostatic interaction with a nearby amino acid, while that of the chorismate reaction cannot be stabilised much relative to the reactant.

So far, the discussion of TST has assumed a single energy barrier with a single transition state. This approximation is acceptable for simple systems, such as small-molecule gas-phase reactions, but for complex systems like enzyme-catalysed reactions, there are many reactant conformations with different MEPs on the multidimensional potential energy surface. Therefore, it makes sense to replace the

transition state by a "dividing surface" or "hypersurface" that separates the reactant region from the product region of configuration space (Pechukas 1981). This plane is missing one degree of freedom, perpendicular to the plane, in configuration space. This missing degree of freedom is the reaction coordinate. The term transition state is still used, but it is important to realise that this does not refer to a single structure but to an ensemble of structures that lie on this surface.

1.1.2. The Importance of Dynamics in Enzyme Catalysis

Classical TST assumes that, while there is an equilibrium between the reactant and transition state, the system goes through the transition state towards the product only once. However, due to the complex dynamics of enzyme-catalysed reactions, barrier recrossings, which reduce the observed rate, are possible. Therefore, not only are equilibrium effects (such as the formation of NACs) important, but also dynamical effects, which affect the system's progress along the reaction profile. Barrier recrossings can be incorporated into TST by invoking so-called transmission coefficients, which reduce the rate according to the frequency of barrier recrossing events.

Ever since Careri proposed the idea of the "fluctuating enzyme" over 30 years ago (Careri 1974), it has been known that enzymes are dynamic entities, and in 1983 Karplus and McCammon first suggested that protein motions can affect the chemistry in the active site, in their example by optimising the donor-acceptor distances to enhance the probability of electron tunneling (Karplus and McCammon 1983). In 1988 Kraut suggested that enzyme motions can alter the transmission coefficients or barrier recrossing frequencies (Kraut 1988).

1.1.3. Semi-Classical Transition State Theory

So far, classical TST has been discussed: the reactant lies at the bottom of the potential energy well, and the system must overcome the potential energy surface. Classical TST does not take into account any quantum mechanical effects. However, these effects are not negligible when the transferring particle is light, such as a proton or hydrogen atom, for which the Heisenberg uncertainty principle becomes very important.

Due to the Heisenberg uncertainty principle, the lowest energy that a particle can occupy must be above the potential energy minimum (Figure 1.2). This energy is termed the zero point energy (ZPE), and the lighter the particle, the greater the ZPE. The ZPE is $\frac{1}{2}h\nu_X$, where ν_X is the vibrational frequency of particle X and h is Planck's constant. Isotopic substitution leads to different activation energies due to the different masses of the isotopes, and is therefore a useful tool to probe chemical mechanisms. The ratio of the rates is the kinetic isotope effect KIE = k_H/k_D for a hydrogen (or proton/hydride) transfer reaction. In semi-classical TST, which takes ZPE into account, the rate can be formulated as

$$k_H = A_H \exp-\frac{\left(\Delta E^{\ddagger} - \frac{1}{2}h\nu_H\right)}{RT} \tag{1.6}$$

In other words, the effect of the ZPE is to increase the rate by reducing the activation energy (Figure 1.2). It follows that the KIEs for protium and deuterium are related by

$$\frac{k_H}{k_D} = \left(A_H/A_D\right)\exp\frac{\left(\frac{1}{2}h\nu_H - \frac{1}{2}h\nu_D\right)}{RT} \tag{1.7}$$

Semi-classical TST makes certain predictions about hydrogen transfer reactions: KIE ≈ 7 at 300K; the ratio of Arrhenius pre-factors is near unity ($A_H/A_D ≈ 1$) because the KIE approaches 0 at infinite temperature; the rates for the three hydrogen isotopes follow the Swain-Schaad relationship, $k_H/k_T = (k_D/k_T)^{3.3}$.

The KIEs discussed so far are the primary (1°) KIEs, corresponding to isotopic substitution of the transferring particle. It is worth mentioning here that secondary (2°) KIEs can also be measured, and the so-called α type 2° KIEs, corresponding to the proximal atom of the group departing from or arriving at the isotope-bearing centre, has been found useful for measuring the Swain-Schaad exponent.
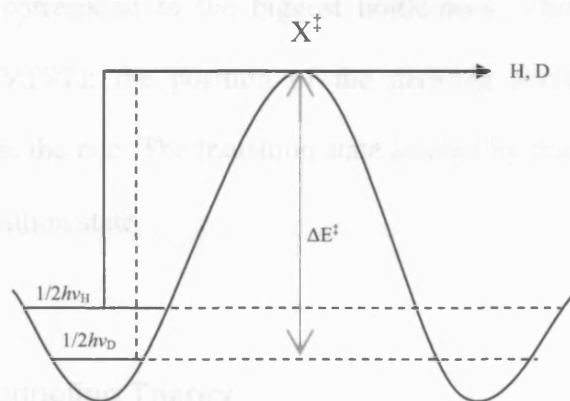
Figure 1.2. Hydrogen isotope transfer reaction profile for semi-classical TST. As with the classical TST both isotopes must have sufficient energy to surmount the barrier, but the energy required is reduced by the ZPE, which depends on the isotope. [Adapted from(Knapp and Klinman 2002)]

1.1.4. Variational Transition State Theory

In conventional TST, the transition state is the saddle point at the top of the MEP, which can be located using appropriate algorithms due to its mathematical characteristics (it has zero gradient and negative curvature). The rate is then calculated by calculating $\Delta G^{\ddagger}$ between the reactant and the saddle point. This is fine for systems with few degrees of freedom at sufficiently low temperatures, where all

reactive trajectories must pass through a narrow region around the saddle point, and are unlikely, once through it, to pass through this narrow region again. However, for large systems at physiological temperatures, the entropy term becomes more important and the energy at the saddle point might not control the rate, and the rate calculated from conventional TST will be an overestimation of the true rate (Pechukas 1981): $k_{TST} \leq k$. This is the variational theorem. Although this is a mathematical result, it can be understood conceptually: to calculate the true rate, the biggest bottle-neck for the reaction on the MEP has to be found, which will minimise the rate. In practice, therefore, the rate can be estimated by using the free energy maximum on the MEP, which will correspond to the biggest bottle-neck. This is the principle of Variational TST (VTST): the position of the dividing surface is (variationally) adjusted to minimise the rate. The transition state located by this method is known as the generalised transition state.

1.2. Quantum Tunneling Theory

Tunneling is the quantum mechanical transition through a classically forbidden energy state, and arises from the wave-particle duality. Heisenberg's uncertainty principle states that if the energy of a particle is known, then its position cannot be predicted reliably. At the quantum scale therefore, a particle of known energy cannot be said to exist in a specific location, but is instead described by the probability of the particle existing in certain locations. The particle is described by its wavefunction, the square of which corresponds to its probability function. Because its position is indeterminate, there is a finite probability of the particle occurring on the far side of an energy barrier that the particle does not possess sufficient energy to surpass. This

concept is illustrated in Figure 1.3. The de Broglie wavelength, λ, describes the relationship between the energy and the positional uncertainty of a particle:

$$\lambda = h/mv \tag{1.8}$$

where m is the particle's mass and v its velocity. The lighter the particle, the longer its de Broglie wavelength, and the higher the uncertainty in its position. In other words, the lighter the particle the wider the barrier it can tunnel through for a given tunneling probability. Biochemical electron transfers are known to occur over distances up to 25 Å, but a proton is 1840 times heavier than an electron. For an idealized rectangular energy barrier of height V and width ℓ the tunneling probability is:

$$P \propto \exp\left[(-2\ell\sqrt{2mV})/\hbar\right] \tag{1.9}$$

Thus, for the same tunneling probability as an electron, the transfer distance for a proton is 0.58 Å (Scrutton et al. 1999), although this distance will be increased for a more realistic curved barrier. This is similar to the width of the energy barrier one would expect in a reaction involving a proton transfer (Caldin 1969; Bell 1980), so the quantum tunneling contribution to such a reaction will be significant.
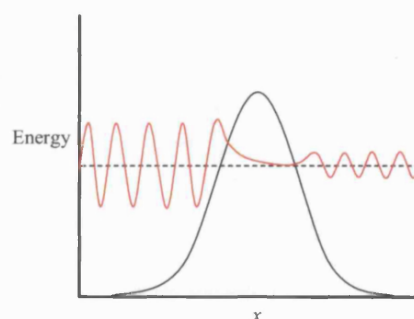
Figure 1.3. Schematic of the propagation of a wavefunction (red line) through a symmetrical energy barrier (solid black line) along a reaction coordinate x.

1.3. Incorporating Tunneling into Transition State Theory

One of the driving forces of the pursuit to understand the relationship between dynamics and catalysis is the recent realisation that quantum tunneling plays a major role in many enzymically catalysed hydrogen transfer reactions. Quantum tunneling has long been established for electron transfer reactions, but only recently has it become apparent that tunneling can also contribute to the transfer of light atoms in enzyme catalysis. The distance which a particle can tunnel is dependent on its de Broglie wavelength, which in turn depends on its mass. As mentioned in Section 1.2, the proton is much heavier than an electron, but its de Broglie wavelength is similar to the distance it is transferred during chemical reactions (Bell 1980). It is therefore not surprising that quantum tunneling should contribute to the chemical transfer of a proton, potentially coupled with one or two electrons as a hydrogen atom or a hydride.

The standard probe to determine the degree of tunneling in a hydrogen transfer reaction is isotopic substitution. As discussed in the Section 1.1.3, semi-classical TST makes certain predictions about the effects of isotopic substitution in such reactions, and deviations from these can be used to infer the degree of tunneling. Figure 1.4 is a general diagram describing the temperature-dependence of the rate of a hydrogen transfer reaction through a static potential energy barrier for both protium and deuterium, with an increasing extent of tunneling. In Regime I, the reaction follows semi-classical behaviour without any
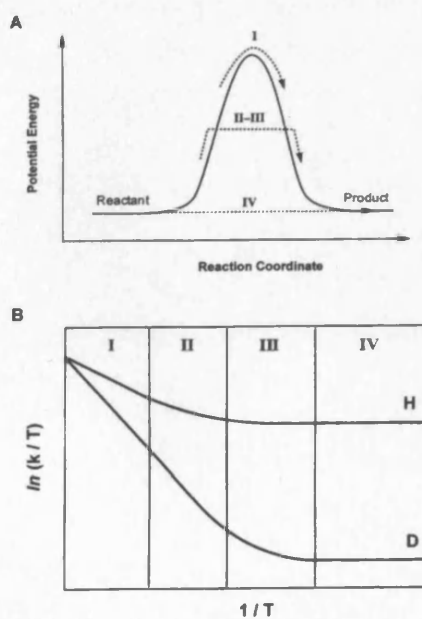
Figure 1.4. The effect on the KIE of tunneling through a static barrier (Scrutton *et al.* 1999).

tunneling contribution. The rate for deuterium increases more quickly with temperature than that for protium, leading to a temperature-dependent KIE. The ratio of Arrhenius pre-factors is equal to 1, since this ratio corresponds to the theoretical KIE at infinite temperature.

The first examples of tunneling in enzymes could be explained by incorporating a quantum tunneling correction factor into classical TST, allowing tunneling to occur below the peak of the energy barrier (Figure 1.5). This is known as the semi-classical Bell correction model (Bell 1980), and the behaviour of reactions that follow this model are described by Regime II of Figure 1.4. The temperature-dependence of the reaction rates comes from the energy required to move part-way up the barrier to the point of tunneling. The lower mass of protium means it can tunnel over longer distances than deuterium, so that it tunnels further below the top of the barrier than the heavier isotope, resulting in the higher curvature for protium in Figure 1.4. Note that the curvature in the Arrhenius plot is not observed in the experimentally accessible temperature range, so that linear, converging lines are obtained. The KIEs are elevated above the semi-classical range, and extrapolation of the plot gives a ratio of pre-factors of less than unity.
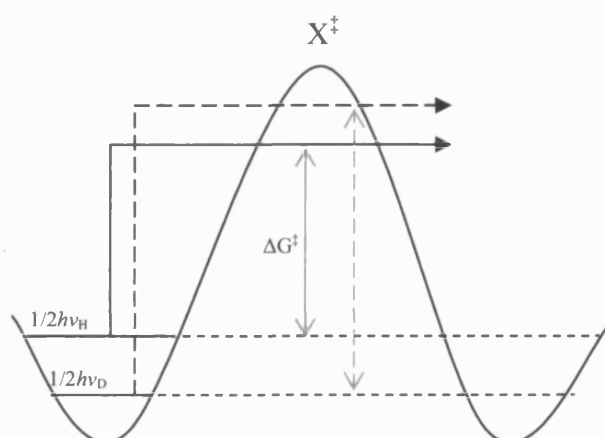
Figure 1.5. Hydrogen isotope transfer reaction profile for the Bell correction model. Tunneling occurs below the transition state. [Adapted from (Knapp and Klinman 2002)].

A different model for hydrogen tunneling in enzyme catalysis was proposed by Dogonadze and Kuznetsov in 1977 (Dogonadze and Kuznetsov 1977), in which an enzyme exists as a collection of thermally activated states, some of which have the correct donor-acceptor distance and internal thermodynamics for the transferring hydrogen to tunnel. This is analogous to Marcus theory for electron transfer (Marcus and Sutin 1985), where the particle transfer itself is a purely quantum-mechanical and therefore temperature independent event, and the temperature-dependence comes from molecular reorganisation. According to this model, which corresponds to Regime IV in Figure 1.4, the KIEs are very elevated and temperature independent, since the activation enthalpies are the same for protium and deuterium ($\Delta\Delta H^{\ddagger} = \Delta H^{\ddagger D}$ - $\Delta H^{\ddagger H} = 0$), and therefore A_H/A_D = KIE. This model was not deemed probable in the 1980s, because it contradicted existing empirical results from reactions studied in solution (Bell 1980), as well as the few enzyme reactions for which the activation energy for both isotopes were available (for example, see (Sumi and Ulstrup 1988; Cha *et al.* 1989; Grant and Klinman 1989)). Today, it is becoming widely accepted that this type of "extreme" tunneling does occur in enzymes, and that it can lead to both temperature dependent and independent KIEs, depending on the coupling between the tunneling event and the protein dynamics.

1.3.1. The Bell Tunneling Correction Model

Initial efforts to account for a tunneling contribution incorporated a tunneling correction into semi-classical TST. This was done using the aforementioned Bell correction model (Bell 1980), which accounts for tunneling that occurs just below the classical transition state (Figure 1.5). The model gives a correction for a symmetrical parabolic barrier and is a function of the curvature of the barrier along the reaction

coordinate, as well as the temperature. The Bell correction may be described by the following equations (Romesburg and Schowen 2005):

$$V = v^{\ddagger}K^{*}(X) = k(X) \tag{1.10}$$

$$k = v^{\ddagger}K^{*} = v^{\ddagger}\frac{Q^{T}}{Q^{R}} \tag{1.11}$$

where V is the reaction rate, $v^{\ddagger}$ is the imaginary frequency with which the transition state goes to product ($V = v^{\ddagger}[X^{\ddagger}]$), K^{*} is the true thermodynamic equilibrium constant for formation of the transition state $X^{\ddagger}$ from the reactant X, k is the experimental rate constant for the reaction of X, and the Q's are partition functions of the transition state (Q^{T}) and reactant (Q^{R}). If the vibrational partition function of the reaction coordinate, Q_{v}^{T}, is factored from Q^{T} to give the partition function $Q^{\ddagger}$ which lacks this vibrational degree of freedom (such that $Q^{T} = Q_{v}^{T}Q^{\ddagger}$) and if $K^{\ddagger}$ corresponds to this "defective" equilibrium constant (such that $K^{\ddagger} = \dfrac{Q^{\ddagger}}{Q^{R}}$), then

$$k = v^{\ddagger}\frac{Q^{T}}{Q^{R}} = v^{\ddagger}Q_{v}^{T}\frac{Q^{\ddagger}}{Q^{R}} = v^{\ddagger}Q_{v}^{T}K^{\ddagger} = v^{\ddagger}Q_{v}^{T}\exp\left(-\frac{\Delta G^{\ddagger}}{RT}\right) \tag{1.12}$$

The pre-exponential factor, $v^{\ddagger}Q_{v}^{T}$, may be described in terms of a harmonic-oscillator partition function:

$$v^{\ddagger}Q_{v}^{T} = v^{\ddagger}\left[1/\left(e^{u_{t}/2} - e^{-u_{t}/2}\right)\right] = \left(k_{B}T/h\right)\left[u_{t}/\left(e^{u_{t}/2} - e^{-u_{t}/2}\right)\right] \tag{1.13}$$

where $u_t \equiv hcv/k_B T$. If u_t is small, corresponding to a gently curved barrier, the pre-exponential factor becomes $k_B T/h$, which gives a simple model of TST with no account made for tunneling. For a more sharply curved barrier, where tunneling plays a role, the Bell correction gives (Caldin 1969):

$$Q_t = \frac{(u_t/2)}{\sin(u_t/2)} \qquad (1.14)$$

where Q_t is the tunnelling correction factor. This is a simplified version of the Bell correction and may only be applied when $u_t < 2\pi$. The most complete form of the tunneling correction is given (Melander and Sauders 1980) by

$$Q_t = \frac{\frac{1}{2}u_t}{\sin(\frac{1}{2}u_t)} - \sum_{n=1}^{\infty} (-1)^n \frac{\exp\left(\alpha \frac{u_t - 2n\pi}{u_t}\right)}{\frac{u_t - 2n\pi}{u_t}} \qquad (1.15)$$

where $\alpha = \Delta G^{\ddagger}/k_B T$. The Bell correction model allows tunneling to occur just below the transition state and exhibits certain characteristic deviations from the semi-classical model (Kim and Kreevoy 1992): an inflated KIE ($k_H/k_D > 7$), an inverse ratio of Arrhenius pre-exponential factors ($A_H/A_D < 1$), and a Swain-Schaad exponent greater than ~3.3.

1.3.2. Multidimensional Tunneling Correction to Variational Transition State Theory

The best model for dealing with reactions where the extent of tunneling is greater than can be accounted for by the Bell correction model is VTST with Multidimensional Tunneling corrections (VTST/MT) (Truhlar *et al.* 1985; Truhlar *et al.* 1996). A free energy surface is calculated along a MEP (as for reactions that follow TST) and tunneling is assumed to occur from a point on the MEP. The rate $k(T)$ at temperature T is given by:

$$k(T) = \kappa(T)k^{VTST}(T) \tag{1.16}$$

where $\kappa(T)$ is the transmission coefficient and $k^{VTST}(T)$ is the rate from VTST calculations. The transmission coefficient is calculated for various configurations along the MEP; the transmission coefficient for a configuration of energy E is given by

$$\kappa(T) = \beta \int_0^\infty dE P^G(E) \exp(\beta\{V[s*(T)] - E\}) \tag{1.17}$$

where $\beta = 1/k_B T$, $V[s*(T)]$ is the potential energy at the variational transition state and P^G is the ground state tunneling probability. The energy for which the integral in Equation 1.17 is maximised (i.e. from which the largest amount of tunneling occurs) is termed the representative tunneling energy (RTE).

1.4. Vibrationally Assisted Tunneling

Over the past decade or so many enzyme-catalysed hydrogen transfer reactions have been found to deviate considerably from the semi-classical tunneling correction predictions; instead, their behaviour seems to fit an extreme tunneling model where enzyme dynamics affect the tunneling probability. In recent years, the groups of Scrutton and in particular Klinman have studied the kinetics of a number of enzyme systems that seem to fit this model to gain insight into the precise nature of the dynamics that facilitate tunneling (see Section 1.3.2), with two key papers in 1999 marking a sea change (Basran *et al.* 1999; Kohen *et al.* 1999).

In 1999 Kuznetsov and Ulstrup published a simple model that incorporates thermal fluctuations into the tunneling framework (Kuznetsov and Ulstrup 1999), illustrating the potential for "gating", i.e. dynamics that compress the transfer distance, to explain apparent activation enthalpy differences for different isotopes. They note that the differences in transfer distances required in their model (~0.1Å) correspond to a gating frequency of 150-200 cm^{-1}, for effective masses for oscillation corresponding to individual residues. This illustrates an important difference between classical over-the-barrier transfer and tunneling: according to TST, only the height of the barrier is important (e.g. Equation 1.1); for tunneling, the distance that the transferring particle has to tunnel is important, as the tunneling probability depends on the overlap between the wavefunctions in the reactant and product configurations.

1.4.1. Failure of the Bell Tunneling Correction

The Bell correction model assumes that tunneling occurs just below the transition state. However, the proton is a very light particle with a de Broglie wavelength similar to the distance it is transferred during chemical transfer reactions. It is therefore

conceivable that H transfer reactions (where H = proton, hydrogen atom or hydride) can occur purely by tunneling, as long as heavy atom motion can reduce the transfer distance sufficiently for tunneling to occur. It has been suggested that such a deformation may be achieved by low-frequency protein motions (Basran et al. 1999; Kohen et al. 1999; Kohen and Klinman 1999; Scrutton et al. 1999; Knapp and Klinman 2002). On the other hand, it has also been suggested (Ball 2004) that enzymes are too soft to achieve such a high-energy configuration, although the experimental evidence is compelling. Furthermore, tunneling through a static barrier predicts enormous KIEs ($\sim 10^3$) and $E_a = 0$ (see Regime IV, Fig 1.4) (Bruno and Bialek 1992; Knapp et al. 2002).

Klinman and co-workers examined the kinetics and isotopic effects in thermophilic alcohol dehydrogenase (ht-ADH) over a wide temperature range, 5-65°C (Kohen et al. 1999). Such a range of temperatures is typically not experimentally accessible, since many enzymes will become denatured at temperatures above ~40°C. A Swain-Schaad exponent greater than 3.3, which agrees with tunneling according to the Bell correction model, was observed. However, the exponent was found to increase with temperature, indicating that the degree of tunneling increases with temperature, which is not consistent with a TST correction: semi-classically, as the temperature increases the system is more likely to have sufficient energy to surmount the barrier, and therefore relatively less likely to tunnel. The Arrhenius plots showed a break point at 30°C, below which k_{cat} gave an increased activation energy. Below 30°C, the 1° KIE gave an inverse A_H/A_D ratio ($A_H/A_D = 1 \times 10^{-5}$) but the KIE above 30°C (physiological temperatures) gave an elevated value ($A_H/A_D = 2$). A_H/A_D ratios below unity are allowed by the Bell correction, but not values above unity. The data appears to indicate that tunneling is more prevalent at high temperatures, which can

be explained by a model that incorporates the environmental fluctuations of the enzyme. Further support for this comes from deuterium exchange experiments (Kohen and Klinman 2000) which indicated a correlation between global enzyme flexibility and the extent of tunneling.

Another enzyme for which a model of environmentally-coupled tunneling was required is soybean lipoxygenase-1 (SLO). SLO exhibits a very large 1° KIE (>80) at room temperature as well as a small activation energy of H-transfer (E_a = 8.8 kJ mol$^-$^{1}) which cannot not be explained by a TST correction model (Rickert and Klinman 1999). The entropic barrier was found to be much larger than the enthalpic barrier ($-T\Delta S^\ddagger$ = 53.6 kJ mol^{-1}, $\Delta H^\ddagger$ = 6.3 kJ mol^{-1}) and the KIE is only weakly temperature-dependent (A_H/A_D = 18), which puts the isotope effect predominantly on the entropic term rather than the enthalpic term, contrary to semi-classical theory (Rickert and Klinman 1999). Further evidence came from the effect of various mutations (Rickert and Klinman 1999) on the Arrhenius prefactors. Mutations near the active site changed the temperature dependence of the KIE (A_H/A_D = 3) and a more distal mutation lead to an inverse ratio of Arrhenius prefactors (A_H/A_D = 0.2). However, the KIE for each of the mutants remained large (>80). This implicates a fundamental change in the tunneling coordinate in the mutants, but with similar tunneling components for all the systems (Knapp et al. 2002). This behaviour, where the nature of tunneling is a function of mutational position (from A_H/A_D > 1 to A_H/A_D < 1) is reminiscent of ht-ADH, where tunneling behaviour was observed as a function of temperature. The importance of the SLO reaction is the magnitude of the KIE, which precludes interpretation by a combination of tunneling and over the barrier transfer and requires that the reaction occurs by pure tunneling.

Methylamine dehydrogenase (MADH) is an enzyme that has been intensely studied by Scrutton and co-workers. One advantage of this system is that the reaction of interest can be separated into reductive and oxidative half-reactions and studied by stopped-flow spectroscopy, so that the proton transfer step may be studied directly, whereas the data for the two previous examples derive from steady-state kinetics. The reductive half-reaction of MADH involves proton abstraction from an iminoquinone intermediate, where the proton is transferred from a donor carbon to an oxygen acceptor. This proton transfer step for substrate methylamine exhibits a large, temperature independent KIE $(k_H/k_D = 16.8)^1$, with a comparable ratio of Arrhenius prefactors $(A_H/A_D = 13.3)$ (Basran et al. 1999), which is far beyond the values allowed by a tunneling correction to TST. This is strongly indicative of extreme tunneling, without any initial C-H bond stretching (see Section 1.1.4), which is supported by the computational work of Truhlar and co-workers revealing that 99% of the reaction occurs by tunneling (Alhambra *et al.* 2001). However, while the relative activation energies are zero $(\Delta\Delta H^{\ddagger} = \Delta H^{\ddagger D} - \Delta H^{\ddagger H} \approx 0)$, leading to the temperature-independent KIE, the activation energies are not $(\Delta H^{\ddagger H} = -44.6 \text{ kJ/mol}; \Delta H^{\ddagger D} = -45.0 \text{ kJ/mol})$, i.e. the rates are strongly temperature-dependent. Scrutton and coworkers rationalise this by invoking a fluctuating, temperature-dependent potential energy surface through which quantum tunneling occurs.

1.4.2. Models of Vibrationally Assisted Tunneling

Experimental observations such as those discussed in the previous section have led to the formulation of several models of tunneling linked to internal enzyme motion. The

---

[1] This is consistent with the KIE of 17.2 previously reported by Davidson and co-workers (
Brooks, H. B., L. H. Jones and V. L. Davidson (1993). "Deuterium kinetic isotope effect and stopped-flow kinetic-studies of quinoproptein methylamine dehydrogenase." <u>Biochemistry</u> **32**: 2725-2729.)

Vibrationally Enhanced Ground State Tunneling model (Bruno and Bialek 1992) was developed because of an apparent discrepancy in using tunneling corrections to semiclassical TST to describe hydrogen-transfer reactions, highlighted by the kinetic data of Grant and Klinman (Grant and Klinman 1989) for the reaction catalysed by bovine serum oxidase (BSAO). The vibrational frequency of a C-H bond ($\omega/2\pi c$) is ~3000 cm^{-1}, which translates to an energy ($\hbar\omega$) of ~36 kJ/mol (8.6 kcal/mol). The observed activation energy for the BSAO reaction, which sets an upper limit to the classical barrier height, is ~56 kJ/mol (13 kcal/mol). If the semi-classical tunneling correction model were correct, then there would only be one excited state below the barrier. This means that the vibrational quanta of the C-H bond are similar to the barrier height, and therefore a classical approach cannot be appropriate. Tunneling through a static barrier would give KIEs that are far too large and temperature independent (Bruno and Bialek 1992), which does not agree with the temperature-dependent KIEs observed in BSAO (Grant and Klinman 1989), and therefore a fluctuating barrier, where the transfer distances are modulated, was invoked. This allowed the model to fit the data for BSAO (Grant and Klinman 1989). However, the model was too simple to account for the temperature-independent KIEs observed since then (see section 1.4.1).

Kuznetsov and Ulstrup presented a more sophisticated model incorporating varying degrees of gating motion that squeezes the donor-acceptor distance to explain the KIEs in different enzymes (Kuznetsov and Ulstrup 1999). This model employs the Franck-Condon principle, that a light particle transition (such as electron or proton transfer) only occurs at heavy nuclear configurations where the light particle energies in the reactant and product states match. This is a corollary of the Born-Oppenheimer approximation, where the fast motion of the light particle can be decoupled from

heavy atom motion. This model was adapted by Klinman and co-workers, who formulated the model of environmentally coupled hydrogen tunneling (Knapp and Klinman 2002), where the dynamics of the system can be partitioned into two types: passive (reorganisation), which leads to degenerate reactant and product states, i.e. a nuclear configuration compatible with tunneling, and active (gating or vibrational enhancement) which enhances the probability of tunneling at this configuration by bringing the reactant and product wells closer together. In this model, passive dynamics are similar to the nuclear reorganisation required for tunneling in the Marcus theory for electron tunneling (Marcus and Sutin 1985), while the active dynamics are akin to those that lead to a fluctuating barrier in the Bruno and Bialek model (Bruno and Bialek 1992).

The model of environmentally coupled hydrogen tunneling, illustrated in Figure 1.6, has allowed the derivation of a tunneling rate expression incorporating both active and passive dynamics. By divorcing the Franck-Condon nuclear overlap from gating, the rate of tunneling becomes (Masgrau *et al.* 2004):

$$k_{tunnel} = (const.) \times \left[\exp\left\{ \frac{-\left(\Delta G^0 + \lambda\right)^2}{4\lambda RT} \right\} \right]$$
$$\times (F.C.\,Term) \times (Active\,Dynamics\,Term)$$

(1.18)

where *const.* is an isotope-independent term; the exponential term is an environmental term which relates the driving force of the reaction, ΔG^0, and the reorganisation energy, λ; *F.C. Term* is the Frank-Condon nuclear overlap along the hydrogen coordinate. When only the lowest vibrational level is occupied by the hydrogen, the
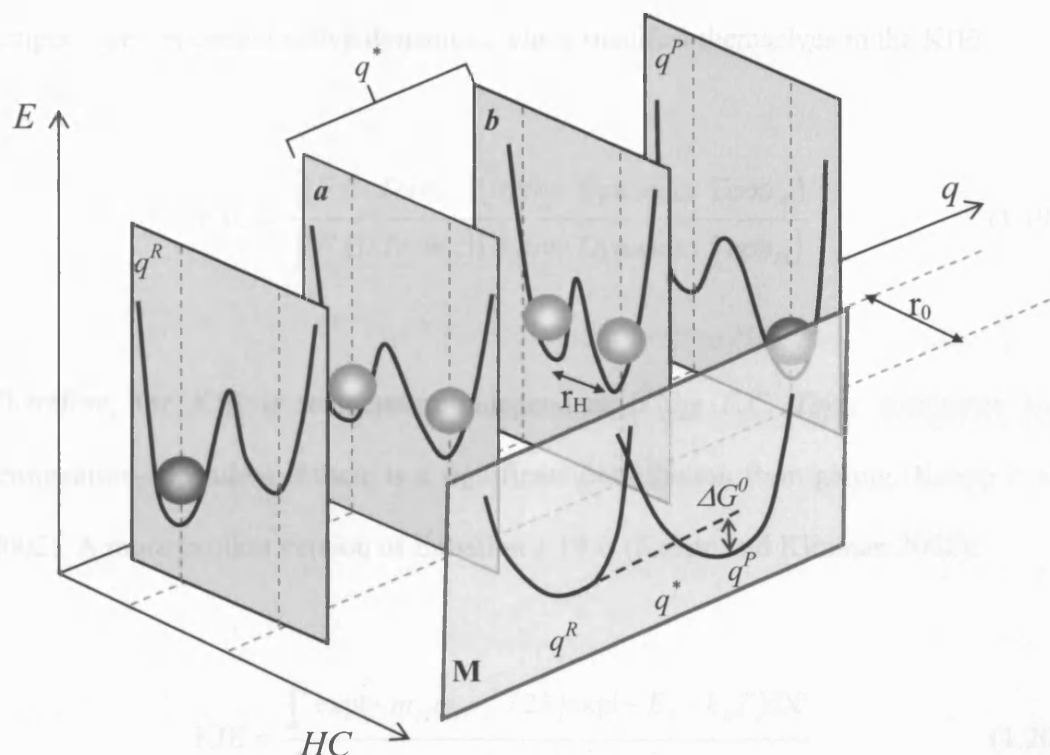
Figure 1.6. Illustration of vibrationally coupled H-tunneling. The axes are E, energy; q, environmental coordinate and HC, the hydrogen coordinate. The vertical panels show the potential energy curves at 4 points on the environmental coordinate: q^R represents the reactant, q^* the transition state with degenerate reactant and product wells, and q^P the product. The grey spheres represent the ground state vibrational wavefunction of the hydrogen nucleus. Panel M shows a Marcus like view of the free energy curves as a function of the environmental coordinate. The motions of the environment modulate the double well allowing the wavefunctions to reach degenerate quantum states. Panels **a** and **b** show two different senarios. In **a** there is no motion along the HC coordinate, the two potential wells being at the equilibrium distance, r_0, while in **b** there is a gating motion which reduces the distance along the HC axis (r_H), between the two degenerate potential wells. This gating increases the probability of tunneling at q^*. [Taken from (Masgrau et al. 2004)]

F.C. Term is independent of temperature. The *F.C. Term* is modulated by temperature-dependent active dynamics, which manifest themselves in the KIE:

$$\text{KIE} = \frac{\int (F.C.\ Term_H)(Active\ Dynamics\ Term_H)}{\int (F.C.\ Term_D)(Active\ Dynamics\ Term_D)} \qquad (1.19)$$

Therefore, the KIE is temperature-independent if the *F.C. Term* dominates and temperature-dependent if there is a significant contribution from gating (Knapp et al. 2002). A more explicit version of Equation 1.19 is (Knapp and Klinman 2002):

$$\text{KIE} = \frac{\int_{r_1}^{r_0} \exp(- m_H \omega_H r_H^2 / 2\hbar)\exp(- E_X / k_B T)\partial X'}{\int_{r_1}^{r_0} \exp(- m_D \omega_D r_D^2 / 2\hbar)\exp(- E_X / k_B T)\partial X'} \qquad (1.20)$$

where r_0 is the equilibrium and r_1 the minimum hydrogen transfer distance, $\omega_{H/D}$ is the vibrational frequency of the reacting bond, and $m_{H/D}$ is the mass of the transferred particle. The transfer distance, $r_{H/D}$ ($r_{H/D} = r_0 - r_X$) depends on the gating coordinate X ($X = r_X \sqrt{m_X \omega_X / \hbar}$); E_X is the energetic cost of gating,

$$E_X = \frac{1}{2}\hbar\omega_X X^2 = \frac{1}{2}m_X \omega_X^2 r_X^2 \qquad (1.21)$$

From these equations, it follows that if $\hbar\omega_X < k_B T$ (i.e. fairly low gating frequency) then the gating term dominates, and the KIE may be temperature-dependent, since the resulting transfer distance for different isotopes will be different. In this case, the A_H/A_D ratio will be less than unity (Knapp and Klinman 2002). On the

other hand, if $\hbar\omega_x > k_B T$ (i.e. a high gating frequency), then the *F.C. Term* dominates, and the KIE will be temperature-independent, since the tunneling distance is temperature independent. Occupation of excited vibrational levels could result in some temperature dependence (Knapp and Klinman 2002), but the Boltzmann distribution at 298K suggests that tunneling should be from the vibrational ground state (Masgrau et al. 2004). Finally, in the regime where $\hbar\omega_x \approx k_B T$, gating plays some role in the probability of tunneling. In this case KIEs will be temperature-dependent and the A_H/A_D value will be lower than for $\hbar\omega_x > k_B T$ and may approach unity. While this is an elegant and fairly successful model, the exact nature of the enzymic motions which give rise to the temperature dependency of KIEs are currently poorly understood, and it is difficult conceptually to distinguish between active and passive vibrations since a motion that affects the relative energies of the reactant and product wells is unlikely to have no effect on the tunneling distance as well.

A similar model was proposed by Schwartz and co-workers (Antoniou and Schwartz 1997), to explain the anomalous KIEs in BSAO, although they employ substrate oscillations rather than protein dynamics. The authors explain that tunneling must be coupled to dynamics: tunneling is a time-reversible event so the reaction could not progress without dynamics to break the symmetry between the reactant and product wells. Thus the protein dynamics bring the system to and away from the degeneracy between the reactant and product wells required for tunneling to occur. This is similar to the passive dynamics discussed above. The dynamics alter the coupling constant between the tunneling particle and the environment, which is electrostatic in nature. Since the different hydrogen isotopes have the same charge, this leads to temperature-independent KIEs.

At the same time, this model invokes so-called promoting vibrations which modulate the donor-acceptor distance (Antoniou and Schwartz 1997) to explain the temperature-dependent KIEs observed in the reaction catalysed by BSAO (Grant and Klinman 1989). For such a vibration to be thermally excited and promote tunneling, it must have an energy below k_BT, which places an upper limit of ~220 cm^{-1} for a typical intramolecular substrate oscillation. If this vibration has a higher frequency, then it is not likely to be thermally activated at room temperature, which leads to a temperature independent KIE. This model incorporates more complex coupling between the promoting vibration and the tunneling probability than the Kuznetsov and Ulstrup model, but crucially it reaches the same conclusions about the effect of the promoting vibration on the KIE.

1.4.3. The Role of Dynamics in Enzymic H-Tunneling: a Case Study

The link between protein dynamics and H-tunneling has been extensively studied for the enzyme dihydrofolate reductace (DHFR), which catalyses hydride transfer between dihydrofolate and nicotinamide adenine dinucleotide phosphate (NADPH). The role of tunneling in this enzymic hydride transfer was suggested by steady-state kinetic studies that exposed temperature-independent KIEs (Maglia and Allemann 2003; Sikorski et al. 2004; Kim et al. 2005), supported by QM/MM calculations that revealed a significant tunneling contribution (Agarwal et al. 2002a; Garcia-Viloca et al. 2003; Pu et al. 2005). Farnum and co-workers published evidence that the rate of hydride transfer from NADPH to 7,8-dihydrofolate(H$_2$F) in DHFR is directly affected by the motion of the flexible M20 loop region (which contains residue Met20) (Farnum et al. 1991). Later, Radkiewicz and Brooks carried out a cross-correlation analysis of MD simulations of three complexes from the catalytic cycle of DHFR

(Radkiewicz and Brooks 2000). Of particular interest is the anti-correlation (i.e. motion in opposite direction) between residues ~40-80 and the M20 and FG loops (residues 14-24 and 116-125 respectively) that is observed in the reactant complex. This strongly coupled motion disappears in the post-hydride-transfer complexes, suggesting that there is a link between hydride transfer and dynamics. Later, Benkovic and co-workers carried out site-directed mutagenesis experiments to study the role of certain highly conserved distal residues (Rajagopalan *et al.* 2002). Their results showed that Gly-121 and Met-42, which are about 19 Å apart, directly affect the rate of hydride transfer, with double mutations showing a non-additive effect, meaning that the double mutation is more detrimental to the rate of hydride transfer than the sum of the individual mutations. This indicates that despite their large separation, these residues are somehow interacting and sensitive to changes in the volume of each-other's side-chain, which can be explained by their involvement in a network of coupled motions.

Computational techniques were used by Benkovic, Hammes-Schiffer and co-workers (Agarwal *et al.* 2002b) to identify a network of coupled promoting motions in DHFR. Candidate residues for such a coupled network were identified from genomic analysis that revealed sequence conservation across 36 species of DHFR. To determine whether these residues are in fact conserved for structural purposes or because they are involved in a network of promoting motions, the effect of enzyme motion on hydride transfer was studied using an in-house hybrid quantum/classical technique for molecular dynamics simulations, which includes the dynamics of the entire solvated enzyme as well as the nuclear quantum effects of the transferring hydride (Agarwal *et al.* 2002a). These simulations use a collective reaction coordinate, defined as the difference between the energies of the product and reactant

valence bond states averaged over the ground state hydrogen vibrational wave function (Warshel 1991). Analysis of the simulations revealed that movement of Phe-31 in the active site seems to push the donor and acceptor groups towards each other (Agarwal *et al.* 2002b) which is consistent with previous mutagenesis studies where the F31Y and F31V mutations were found to decrease the rate of hydride transfer (Chen *et al.* 1987). Furthermore, the motion of Asp122 on the exterior of the enzyme was found to be important to catalysis, as its motion relative to Gly15 is coupled to the global reactions coordinate. The adjacent Ile14 is believed to direct the donor to the acceptor through backbone hydrogen bonding to NADPH, and the simulations also suggest that the motion of the side-chain of Ile14 pushes the donor towards the acceptor (Agarwal *et al.* 2002b). In accord with the previous mutagenesis studies of Benkovic and co-workers (Rajagopalan et al. 2002), analysis of the relative motion between the side-chains of Met42 and Gly121 suggest that they are also involved in the network of coupled motion, since at the transition state, when the donor-acceptor distance is at a minimum, the distance between Met42 C_β and Gly121 C_α is also near its minimum (Agarwal *et al.* 2002b).

1.5. Aromatic Amine Dehydrogenase

Aromatic amine dehydrogenase is the second enzyme known to possess the tryptophan tryptophylquinone (TTQ) prosthetic group after MADH (Govindaraj *et al.* 1994). These enzymes are very similar, mechanistically and structurally, both catalysing the oxidative deamination of primary amines. The only major difference appears to be the substrate specificities, with MADH favouring very small amines (e.g. its physiological substrate methylamine), and AADH favouring large aromatic amines. The kinetics of tunneling in these quinoproteins has been extensively studied

(Basran et al. 1999; Basran et al. 2001; Masgrau et al. 2004), and high-resolution x-ray data of the enzyme with bound substrate tryptamine became available by Leys's group (Masgrau et al. 2006) at the start of this project. This system is therefore ideal for the computational study of hydrogen tunneling in enzymes and its link to catalysis.

1.5.1. Structure and Chemistry

AADH was first purified and characterised from the soil bacterium *Alcaligenes faecalis,* by Iwaki *et al.* (Iwaki *et al.* 1983). AADH catalyses the oxidative deamination of a primary amine to its corresponding aldehyde and ammonia, and the two electrons that are derived from the amine are subsequently transferred to its physiological electron acceptor enzyme azurin:

$$RCH_2NH_2 + H_2O \rightarrow RCHO + NH_3 + 2e^- + 2H^+ \qquad (1.22)$$
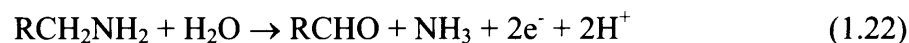
This reaction employs the TTQ prosthetic group (Figure 1.7), which is formed from post-translational modification of two tryptophan amino acids (Chistoserdov *et al.* 1990). TTQ is involved both in catalysis and in the subsequent electron transfer, but a precise mechanism was not proposed until 1995 (Hyun and Davidson 1995), and a more complete mechanism was recently published, which is supported by crystallography of several intermediates (Figure 1.8) (Masgrau et al. 2006). Nucleophilic attack by the amine substrate on one of the TTQ carbonyls is initiated by deprotonation
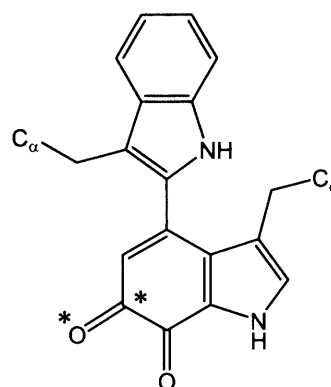
Figure 1.7. Schematic of the TTQ prosthetic group. The amine substrate bonds to the marked C, and replaces the marked O.
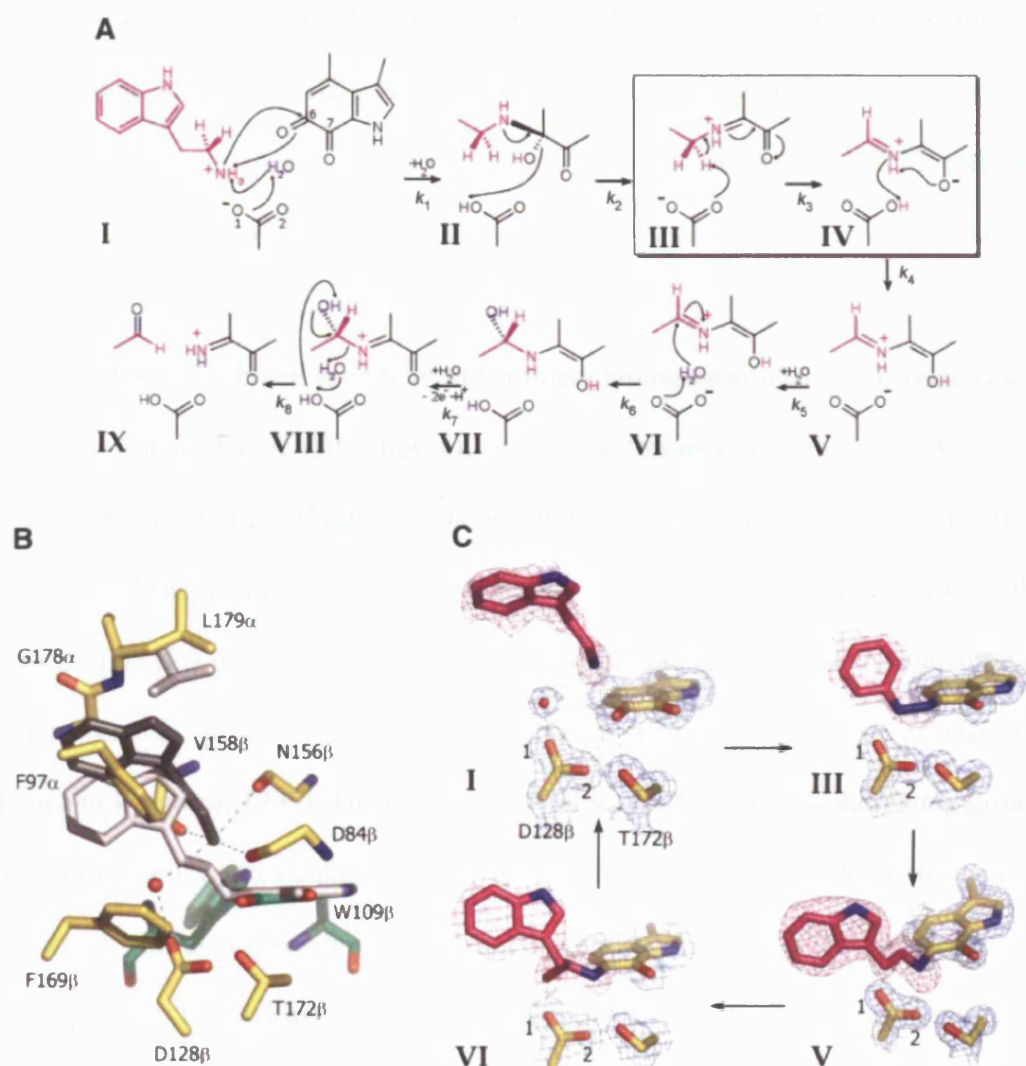
Figure 1.8. Reductive half reaction of AADH with tryptamine. (**A**) Proposed reaction mechanism, with the tunneling step (k_3) shown in the box. (**B**) AADH active site structure for the ligand-free protein (green carbon atoms (TTQ) and yellow carbon atoms), the position occupied by the substrate in complex with the reduced AADH (dark grey) and the positions in intermediate V of substrate Leu179α and TTQ (light gray); putative hydrogen bonds are shown as green dashed lines. (**C**) Structure of selected active site groups with corresponding electron density for intermediates with available crystal structures. [Taken from (Masgrau et al. 2006)].

of the substrate by an active site aspartate, Asp128β, via a bridging water molecule (I). This forms a carbinolamine intermediate (II), which loses water and becomes an iminoquinone Schiff base (III). Asp128β then abstracts a proton from the α position of the iminoquinone, thus reducing the TTQ to form intermediate (IV). This step, k_3, is known to proceed via tunneling (Section 1.5.2). Finally, the aldehyde product is released by hydrolysis of the imine bond (V-IX).

AADH has a broad specificity for primary amine substrates, but Davidson and co-workers found that AADH shows a preference towards aromatic substrates over simple aliphatic amines (Hyun and Davidson 1995). They also observed that for p-substituted benzylamine substrates the rate of proton abstraction from the iminoquinone (k_3) increases with the electron-withdrawing ability of the substituents on the aromatic group, which is consistent with a proton abstraction mechanism (Hyun and Davidson 1995). The quinone is a delocalised electron-withdrawing group, whose effect will be to weaken the C-H bond to be broken by the proton abstraction step, which will also allow the transferring proton to get closer to the acceptor atom. This appears to be, at least in part, the catalytic effect of the TTQ prosthetic group (Siebrand and Smedarchina 2004).

A high-resolution crystal structure of AADH with bound substrate tryptamine became available from Leys's group at the beginning of the project (PDB ID: 2AGX) (Masgrau et al. 2006). AADH has a heterotetrameric $\alpha_2\beta_2$ structure (Figure 1.9A), with subunit molecular weights of 39 and 18 kDa. The α subunits have a 7-bladed beta-propeller structure, with two of the blades connected by a 2-turn α-helix. The first strand of the propeller comes from a loop region that hydrogen-bonds to the β-sheet of the β subunit from the other heterodimer. The main feature of the β-subunit is

this twisted, three-stranded antiparallel β-sheet, with a β-hairpin loop connecting the first two strands of the sheet.

The TTQ is part of the β subunit, with the substrate binding site lying between the α and β subunits of one heterodimer. One face of the aromatic group of the bound amine – an indole in the case of tryptamine – is packed against β subunit residues Val158β and Asn159β, while the opposite face is covered by Phe97α, which covers the binding site (Figure 1.9B). In order for the substrate to enter or leave the active site, Phe97α has to change conformation. Asp128β, which abstracts the proton from iminoquinone intermediate III, is positioned close to the imine nitrogen, N1, and donor carbon, C1. This Asp residue is hydrogen-bonded to the backbone amine of Trp160β (the tryptophan part of TTQ) and the sidechain hydroxyl of neighbouring Thr172β. The quinone is hydrogen bonded to the backbone carbonyl of Ala82β and the backbone amine of Asp84β, and N1 is hydrogen-bonded to the backbone carbonyl of Asp84β.

A crystal structure for the iminoquinone intermediate – the reactant in the tunneling step – could not obtained, but the structure for the analogous

Figure 1.9. Structure of AADH with bound substrate tryptamine, intermediate V. **(A)** Structure of heterodimer, showing the α (blue) and β (red) subunits, and the iminoquinone (orange sticks). **(B)** Active site structure showing the hydrogen bonding to the quinone and Asp128β, and the position of the indole ring, with relevant atoms labeled.

phenylhydrazine inhibitor was (Masgrau et al. 2006). The phenylhydrazine nitrogen, which mimics C1 (Figure 1.8C, III), lies sufficiently close to both Asp128β carbonyl oxygens (O1 2.8 Å, O2 3.2 Å) for either oxygen to be a potential H-tunneling acceptor. However, the next step in the mechanism, coupled with the crystal structure of intermediate V, sheds some light on which oxygen is the most likely proton acceptor: the next step in the catalytic cycle involves proton transfer from Asp128β to N1, and the geometry of intermediate V appears compatible with this transfer occurring from O2. If the transfer was to occur from O1, then a significant rotation round the N1-C6 bond would be required, which would in turn require significant repositioning of Asp84β (Figure 1.7C) (Masgrau et al. 2006). While this is not conclusive evidence for proton transfer to and subsequently from O2, it does appear that O2 is mechanistically the most likely tunneling acceptor. This is further supported by the computational results discussed in Section 1.5.3.

1.5.2. Experimental Evidence for Tunnelling in AADH

Kinetic data for the proton transfer step (k_3) in AADH with tryptamine, benzylamine and dopamine was obtained by Scrutton and co-workers using stopped-flow techniques, which revealed that this step typically occurs by tunneling (Basran et al. 2001). For dopamine ($k_3^H = 102 \pm 1.0$ s^{-1} at 25°C), an elevated temperature-independent KIE (12.9 ± 0.2) with a similar ratio of Arrhenius prefactors ($A_H/A_D = 9.4 \pm 1.6$) was observed. Furthermore, the enthalpies of activation ($\Delta H^\ddagger$, from the Eyring equation) were found to be essentially identical (within experimental error) for both protiated and deuterated dopamine $\Delta H^{\ddagger H} = 50.9 \pm 0.7$ kJ/mol, $\Delta H^{\ddagger D} = 51.6 \pm 0.7$ kJ/mol). This strongly indicates an extreme tunneling scenario, with, in the

environmentally coupled hydrogen tunneling formalism (Knapp and Klinman 2002), a passive dynamics regime.

In initial experiments (Basran et al. 2001), the tunneling step for protiated tryptamine was too rapid for a similarly detailed study of the temperature-dependence ($k_3{}^H = 503 \pm 5$ s^{-1} at 4°C). Nevertheless, a highly inflated KIE (54.7 $\pm$ 1.0) was obtained at 4°C. This large KIE means that temperature dependence studies of deuterated tryptamine were possible, thanks to its lower rate. The activation enthalpy thus obtained (53.5 $\pm$ 1.2 kJ/mol) was identical to those for dopamine: $\Delta H^{\ddagger D}{}_{tryptamine} = \Delta H^{\ddagger D}{}_{dopamine} = \Delta H^{\ddagger H}{}_{dopamine}$. If this step was an over-the-barrier proton transfer or tunneling from an excited state, then $\Delta H^{\ddagger D}{}_{tryptamine}$ would be expected to be greater than $\Delta H^{\ddagger D}{}_{dopamine}$. From this data, it was concluded that the proton transfer for tryptamine also occurs via vibrationally assisted tunneling. This has since been confirmed by temperature-dependence data for protiated tryptamine (Masgrau et al. 2006), which revealed an identical enthalpy of activation, within experimental error ($\Delta H^{\ddagger H}{}_{tryptamine} = 57.3 \pm 3.4$ kJ/mol).

Benzylamine was the slowest of the three substrates ($k_3{}^H = 1.81 \pm 0.02$ s^{-1} at 25°C), but the same tunneling mechanism was observed: the activation enthalpies for benzylamine ($\Delta H^{\ddagger H} = 68.1 \pm 1.4$ kJ/mol) and deuterated benzylamine ($\Delta H^{\ddagger D} = 67.1 \pm 0.9$ kJ/mol) are identical, and the ratio of Arrhenius prefactors ($A_H/A_D = 3.7 \pm 2.0$) was similar to the temperature-independent KIE (4.8 $\pm$ 0.2). The larger activation enthalpies compared with the other two substrates suggests that there is a larger energetic cost for the structural deformations required to achieve tunneling.

1.5.3. Computational Studies of the Tunneling Step for Tryptamine

The work presented in this thesis focuses on the dynamics involved in promoting the tunneling step, i.e. the dynamics of the iminoquinone intermediate III. This is an iminoquinone formed by condensation of a tryptamine and a quinone, and will henceforth be referred to as the tryptiminoquinone. Concurrently with this work, the tunneling event itself was studied collaboratively, using computational methods, by the Sutcliffe and Mullholland groups (Masgrau et al. 2006). They employed a QM/MM (PM3/CHARMM22) modelled tryptiminoquinone, built from a 1.1 Å crystal structure of intermediate V, where the iminoquinone and Asp128β sidechain were treated quantum mechanically. The free energy for classical proton transfer was calculated along the reaction coordinate z defined as [d(C-H) - d(O-H)], using a 25 Å radius sphere simulation system centred on N of the iminoquinone (i.e. atoms outside this radius were fixed). Each z-value window was sampled for 30 ps using stochastic boundary molecular dynamics. The height of the resulting classical free energy barrier was then corrected using higher level QM results obtained for the similar MADH system (Tresadern et al. 2003), to give the classical free energy of activation ($\Delta G^{\ddagger,classical}$). The free energy correction for tunneling ($\Delta G^{\ddagger,tunneling}$) was estimated using VTST/MT calculations. The phenomenological free energy of activation ($\Delta G^{\ddagger,act}$) was obtained by correcting the classical energy to account for H-tunneling ($\Delta G^{\ddagger,act} = \Delta G^{\ddagger,classical} + \Delta G^{\ddagger,tunneling}$). The Eyring equation was then employed to estimate the rate constants for each isotope (Masgrau et al. 2006).

After the initial energy minimisation of the iminoquinone, it was found that transfer of H1 could occur to either O1 or O2 (modelled d(O1-H1) = 1.74 Å, d(O2-H1) = 2.67 Å), and therefore both transfers were studied (Masgrau et al. 2006). Note that without any knowledge of how heavy atom motion might modulate these

distances, proton transfer to O1 would seem more likely. However, proton transfer to

O2 is favoured by a lower free energy of activation ($\Delta G^{\ddagger,classical}$ = 20.0/18.1 kcal/mol

for O1/O2), and by a stronger thermodynamic driving force ($\Delta G_{reaction}$ = 4.8/-7.8

kcal/mol) (Masgrau et al. 2006), in agreement with the previous mechanistic

discussion (Section 1.5.1). The proton transfer is facilitated by the strong polarisation

of the C–H bond, which arises from the cationic nature of the iminoquinone, and the

elevated pK_a of Asp128β in the presence of the iminoquinone (Masgrau et al. 2006).

The H-tunneling correction was similar for proton transfer to both oxygens

($\Delta G^{\ddagger,tunneling}$ = -4.6/-4.9 kcal/mol), so that the experimentally observed free energy of

activation (~12.7 kcal/mol, k_3 ~ 3500 s^{-1}) agrees well with that calculated for proton

transfer to O2 (13.2 kcal/mol, k_3 = 1500 s^{-1}), but less well with that calculated for O1

(15.4 kcal/mol, k_3 = 38 s^{-1}) (Masgrau et al. 2006). The tunneling profiles for O1 and

O2 are shown in Figure 1.10.

The simulations of proton transfer indicated a clear preference for proton

transfer to O2, and revealed that a large tunneling component is required to explain
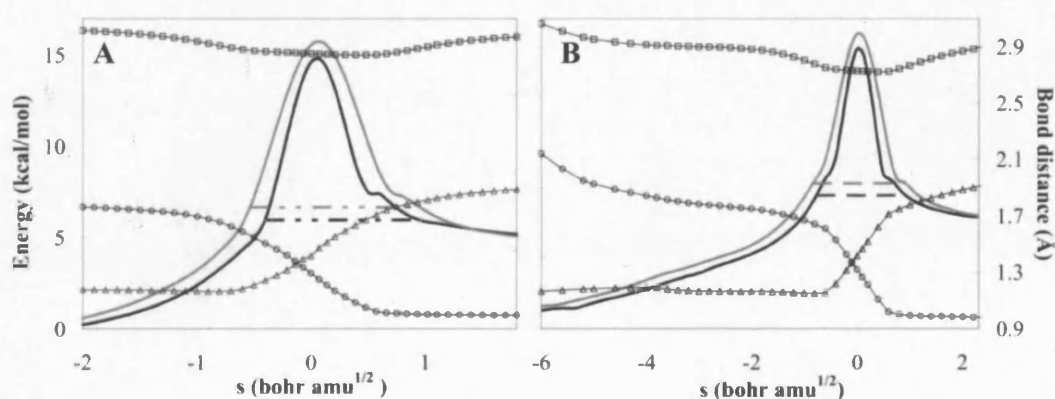
Figure 1.10. Reaction profiles for proton tunneling to (**A**) O1 and (**B**) O2 at 300 K: minimum energy paths (including zero point energies) obtained for tunneling calculations for (solid lines) and representative tunneling energies (dashed lines). The black and grey lines are for perprotio- and perdeuterotryptamine respectively. The reaction coordinate, s, is the mass-weighted difference in position from the transition state, with negative values on the reactant side and positive on the product side (1 bohr = 0.529 Å). Selected distances for the perprotio reaction path are also shown (right hand axis): C-O (squares), H-O (circles) and C-H (triangles). [Taken from (Masgrau et al. 2006)]

the observed free energy of activation – it was estimated that 99.9% of the reaction proceeds via tunneling. Furthermore, the KIEs obtained if no tunneling was considered (5.0/5.8 for O1/O2) are below the semi-classical limit, while those obtained when tunneling was incorporated (42/93) are of the same order of magnitude as the experimentally determined values (Section 1.5.2) (Masgrau et al. 2006).

Analysis of the reaction profiles for proton transfer to both potential oxygen acceptors revealed that heavy atom motion is more important for proton transfer to O2 than to O1 (Figure 1.10). For transfer to O2, the RTE is reached purely by heavy atom motion, with the O2-H1 distance rapidly shortening to ~2.0 Å at a relatively low energetic cost (< 2 kcal/mol). For O1, on the other hand, achieving the RTE requires some initial C–H bond stretching. The reason for this difference can be understood from the orientation of C1/H1 relative to O1 and O2 in the reactant (Figure 1.11): in the reactant, C1/H1 is more aligned with O1 than O2, which means that a rotation of C1/H1 can help bring H1 closer to O2. Tunneling occurs once the H1–O1/O2 separations are reduced by classical activation to ~1.51/1.64 Å, respectively, at which point the proton tunnels a distance of ~0.49/0.59 Å through the barrier (Masgrau et al. 2006).
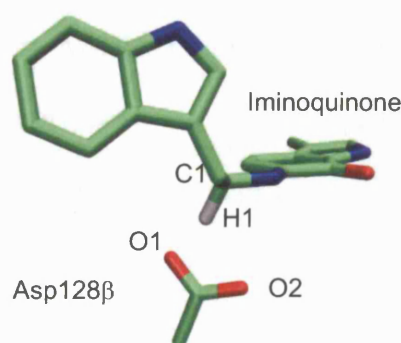
Figure 1.11. Reactant structure for proton transfer from C1 of the iminoquinone intermediate to either O1 or O2 of Asp128β.

1.6. Perspectives and Aims

It is clear that the link between enzyme dynamics and tunneling is far from understood, and that this field is surrounded by controversy (Ball 2004). For example, the term vibrationally enhanced ground-state tunneling (Bruno and Bialek 1992) suggests that by utilising its vibrational energy an enzyme increases the amount of tunneling that occurs relative to over-the barrier transfers. In this view, tunneling is part of the catalytic effect of enzymes. On the other hand there is experimental and computational evidence that the degree of tunneling in solution is identical to that in the enzyme (Hwang and Warshel 1996; Doll et al. 2003; Doll and Finke 2003). Furthermore, the distinction between active and passive dynamics are essentially phenomenological, a translation of the observed kinetics into mathematical terms in a relatively simple model: as previously mentioned, it is conceptually difficult to imagine a vibration that alters the relative energies of the reactant and product states without affecting the tunneling distance, and vice-versa.

The work reported in this thesis focuses on the proton transfer step from the tryptiminoquinone intermediate to an aspartate residue during the oxidative deamination of tryptamine by AADH. Two conclusive aspects of this proton transfer are that the experimental observations can only be explained by an extreme tunneling regime, and that the rate is temperature dependent. Therefore, the dynamics must promote, although not necessarily enhance, the non-energetic tunneling event. At this point, it is important to distinguish between the terms "enhance" and "promote" as used in this thesis: the term "enhance" refers to an increase in the amount of tunneling relative to over-the barrier transfers, whereas for the purposes of the current work, "promote" will be used to indicate that the probability of tunneling is increased (thus

increasing the amount of tunneling in absolute terms). Vibrations that promote

tunneling may very well also increase the probability of over-the barrier reactions.

The aim of this research is therefore to understand, at the atomic level, the nature of

the promoting dynamics in the proton transfer from the tryptiminoquinone

intermediate to the neighbouring aspartate. The main questions that this work will

attempt to answer are:

(1) Is there a specific vibration of a specific frequency that promotes

tunneling, or does the tunneling probability depend on Brownian /

stochastic motion?

(2) If such a vibration exists, is it the result of a large-scale network of

vibrations or just local fluctuations?

(3) How does the nature of any such promoting vibration relate to the concept

of vibrationally coupled tunneling of Kuznetsov and Ulstrup (Kuznetsov

and Ulstrup 1999)?

Since these questions are concerned with dynamics, the main computational

technique employed is molecular dynamics (MD). The first section of the research

employs nanosecond-timescale MD simulations to study the global motions within the

enzyme and the overall motions of the atoms of interest (Chapter 3), and analyse how

these impact on the donor-acceptor and hydrogen-acceptor distances critical to

tunneling probability. The next section focuses on the picosecond to sub-picosecond

timescale (Chapter 4), using spectral density analysis (Caratzoulas and Schwartz

2001; Caratzoulas *et al.* 2002) to investigate specific vibrations within the active site

and determine whether tunneling may be promoted by specific atomic motions.

Potential energy surfaces for the proton transfer for snapshots taken from an MD

simulation are also calculated (Chapter 5) to analyse how internal enzyme motions

affect the reaction profile. In particular, a comparison will be drawn between the potential energy surfaces for proton transfer in the $\alpha_2\beta_2$ hetereotetramer and in the isolated β monomer. Finally, the kinetics for the tunneling in tryptamine will be discussed within the framework of the Kuznetsov and Ulstrup model (Chapter 6).

2. Computational Methods

2.1. Preface

In many cases, chemical and biochemical processes occur on a scale much smaller than can be observed directly by experimental methods. Computational chemistry is therefore essential, as a complement to other techniques, for studying the behaviour of chemical systems and the mechanisms by which reactions occur. The underlying physical laws, governed by quantum mechanics, are understood to such a degree that very accurate representations of molecular systems are possible using so-called *Ab initio* methods, where the wavefunctions of individual electrons are computed. Unfortunately, such a high degree of precision is limited to very small molecules; as the number of atoms increases, the complexity of the system rises too rapidly for modern computational power to keep up.

When dealing with large chemical systems systems, it is therefore necessary to simplify the models by using varying degrees of approximation, for example by assuming that only the outermost shell of electrons is important or that the energy of a system only depends on its nuclear configuration. Furthermore, as the complexity of the system increases, so too does the difficulty of extracting useful information from e.g. molecular dynamics simulations. For instance, large systems such as proteins have such a huge number of degrees of freedom that understanding which motions are important or coupled and which are not is no trivial task. A range of analytical tools are therefore employed to reduce the dimensionality and extract the important information from complex simulations.

2.2. Molecular Mechanics Force Fields

Molecular Mechanics (MM) force fields are used to calculate the potential energy of a system based on its nuclear coordinates. The electrons are disregarded, and their electrostatic effects are treated implicitly in the force field. MM is based on the Born-Oppenheimer approximation, that the immense difference in mass between electrons and nuclei allows the electrons to respond almost instantaneously to the motions of the nuclei. Atoms are therefore treated as hard spheres, and bonds as springs. Parameter sets define the atomic charges and the force constants that specify the bond strengths and the energy required to deform a bond angle or rotate about a bond (i.e. change the dihedral angle). The approximations made by MM allow the modelling of large systems such as enzymes, and it is possible for force fields to provide simulations as accurate as those generated using the highest-level quantum mechanical calculations (Leach 2001). On the other hand, since MM cannot be used to calculate properties that are dependent on the electronic distribution in a molecule, and bonds are treated as solid springs, it cannot be used for simulations involving bond formation or bond breaking.

The potential energy function of a system is a sum of the individual energy functions that describe the forces governing atomic motions. These are the bonded terms, V_{bonded}, and non-bonded terms, $V_{non-bonded}$. The V_{bonded} terms describe the energies contained in the bonds, angles, and bond rotations. The $V_{non-bonded}$ terms account for the interactions between atoms separated by three or more covalent bonds. The total energy is then given by

$$V_{tot} = V_{bonded} + V_{non-bonded} \qquad (2.1)$$

There are a number of MM force fields currently available for use with biological macromolecules. Among the most commonly used are AMBER (Cornell *et al.* 1996), CHARMM22 (MacKerell *et al.* 1998) and GROMOS (van Gunsteren and Berendsen 1987). The CHARMM22 force field as implemented in the CHARMM program (Brooks et al. 1983), version 27, was used for all MM simulations documented in this thesis. The CHARMM22 force field potential energy function can be described by the following equation:

$$V_{tot} = V_{bonds} + V_{angles} + V_{dihedrals} + V_{impropers} + V_{vdW} + V_{el} + V_{UB} \qquad (2.2)$$

The first four terms describe the bonded interactions, and the last three the non-bonded interactions. Each term will now be described in more detail.

The bond stretching term, V_{bonds} represents the contribution to the potential energy of bond stretching/compression away from the optimum bond lengths. The bond energy is based on Hooke's law:

$$V_{bonds} = \sum_{bonds} k_b (r - r_0)^2 \qquad (2.3)$$

where k_b is the force constant representing the stiffness of the bond, r is the bond distance and r_0 the optimum bond length. Each pair of bonded atoms is assigned unique k_b and r_0 parameters based on the atom types.

The angle bending term, V_{angles}, represents the contribution of the energy associated with a deformation about the equilibrium bond angle. This is also based on Hooke's law:

$$V_{angles} = \sum_{angles} k_\theta (\theta - \theta_0)^2 \qquad (2.4)$$

where k_θ is the force constant for the angle spring, θ is the angle and θ_0 is the equilibrium angle. Unique parameters are assigned for each bonded triplet of atoms based on the atoms types.

The torsion energy term, $V_{dihedrals}$, describes the energy associated with the rotations about bonds, which is modeled by a simply periodic function:

$$V_{dihedrals} = \sum_{dihedrals} A[1 + \cos(n\tau - \phi)] \qquad (2.5)$$

where ϕ is the dihedral angle, n is an integer which represents the multiplicity of the dihedral, and A is the force constant.

Improper torsion angles are torsion angles where the atoms are not sequentially bonded to one another. This $V_{impropers}$ term is necessary to ensure that the correct stereochemistry is maintained, as chirality may change during geometry optimisations due to inversion of atomic position, and to maintain planarity about sp^2 hybridised atoms:

$$V_{impropers} = \sum_{impropers} k_{imp} (w - w_0)^2 \qquad (2.6)$$

where k_{imp} is the force constant and w and w_0 are the improper torsion angle and equilibrium improper torsion angle, respectively.

The van der Waals term describes the interplay between the attractive interactions that arises between non-bonded atoms due to induced dipole-dipole

moment interactions at short distances and the repulsive interactions at distances shorter than their contact radii when the electronic orbitals of the atoms start to repel each other. The combination between these attractive and repulsive interactions are described by the Lennard-Jones potential:

$$V_{vdW} = \sum_{ij} 4\varepsilon_{ij} \left[\left(\frac{\sigma_{ij}}{r_{ij}} \right)^{12} - \left(\frac{\sigma_{ij}}{r_{ij}} \right)^{6} \right] \tag{2.7}$$

where i and j are two adjacent atoms, ε_{ij} is the energy parameter and sets the depth of the potential energy well, r_{ij} is the distance between the two atoms and σ_{ij} is the distance between the atoms at which the potential energy is at its minimum. The term $(\sigma_{ij}/r_{ij})^{12}$ models the repulsive force and the term $(\sigma_{ij}/r_{ij})^{6}$ the attractive force.

The electrostatic contribution to the potential energy is modeled using a Coulombic potential:

$$V_{el} = \sum_{ij} \frac{q_i q_j}{\varepsilon_{ij} r_{ij}} \tag{2.8}$$

where q_i and q_j are the net atomic charges of atoms i and j, r_{ij} is the interatomic distance and ε is the dielectric constant between the interacting atoms for a particular medium. The dielectric constant is often set to the value for a vacuum ($\varepsilon = 1$), but a higher value or a distance-dependent value may be used to account for the screening effect when other atoms or solvent molecules enter the space between the two charges. For example, if solvent molecules are treated explicitly in the model, then a

dielectric constant of 1 is typically used, while a distance-dependent value is often used to mimic the screening effect of the solvent if the solvent is treated implicitly.

The last term in the CHARMM potential energy function is the Urey-Bradley term, which describes the interaction between atoms separated by two bonds, known as the 1,3 interaction:

$$V_{UB} = \sum_{UB} k_{UB}(S - S_0)^2 \tag{2.9}$$

where k_{UB} is the force constant and S the distance between atoms I and K in the bonded triplet I-J-K, and S_0 is the equilibrium distance.

2.3. Quantum Mechanical Methods

Molecular modelling methods that employ Quantum Mechanics (QM) attempt to solve the Schrödinger equation:

$$H\Psi = E\Psi \tag{2.10}$$

where H is the Hamiltonian, Ψ is the wavefunction and E is the energy. Using the Born-Oppenheimer approximation, these terms can partitioned into electronic and nuclear terms, so that solving the Schrödinger equation boils down to solving for the electronic energy, E_c. The electronic energy can be obtained from

$$E_e = \int \Psi^* H_e \Psi d\tau = \langle \Psi | H_e | \Psi \rangle \tag{2.11}$$

where τ represents all the spatial dimensions. QM methods use the Linear Combination of Atomic Orbitals (LCAO) approximation, where each molecular orbital (MO), ψ_i is a linear combination of M atomic orbitals ϕ_i:

$$\psi_i = \sum_{j=1}^{M} c_{ji}\phi_j \qquad (2.12)$$

where c_{ji} represents the contribution of atomic orbital j to the molecular orbital i.

2.3.1. Hartree-Fock Methods

The most accurate description of a quantum mechanical system would contain an infinite number of MOs; in practice, this is clearly not possible. QM methods therefore use the basis set approximation of the Roothaan-Hall equation (Leach 2001):

$$\mathbf{FC} = \mathbf{SCE} \qquad (2.13)$$

where $\mathbf{F}$ is the Fock matrix, $\mathbf{C}$ the matrix of basis function coefficients, $\mathbf{S}$ the overlap matrix, and $\mathbf{E}$ the matrix of orbital energies (a diagonal matrix). The elements of the $\mathbf{F}$ and $\mathbf{S}$ matrices for electron e are given by:

$$\mathbf{F}_{ij} = \int \phi_i^*(e) f_e \phi_j(e) d\tau \qquad (2.14)$$

$$\mathbf{S}_{ij} = \int \phi_i^*(e) \phi_j(e) d\tau \qquad (2.15)$$

where f_1 is the fock operator of electron e:

$$f_e = \mathbf{H}^{core}(1) + \sum_{j=1}^{n} \left[2\mathbf{J}_j(e) - \mathbf{K}_j(e) \right] \qquad (2.16)$$

where $\mathbf{H}^{core}$ is core Hamiltonian for electron 1, n is the total number of orbitals $\mathbf{J}_j$ is the Coulomb operator, defining the repulsive force between electrons e and j, and $\mathbf{K}j$ is the exhange operator, defining the effect of exchanging the two electrons. The sum of Coulombic repulsions is composed of a net repulsion energy for each electron, which is achieved by treating all of the other electrons as a smooth distribution of negative charge. In other words, electron-electron repulsion is only included as an average value, because electron correlation is not taken into account. This is the weakness of the Hartree-Fock (HF) method, which employs the equations discussed thus far.

The Hartree-Fock (HF) method is the starting point for all QM methods: both more approximate and more accurate treatments build on this method. The method used in Chapter 1, for MM parameteristation, is restricted Hartree-Fock (RHF), where each spatial orbital must have two electrons with opposite spin (this works only for singlet systems, i.e. closed shells).

2.3.2. Density Functional Theory

A more accurate method, which takes electron correlation into account, is density functional theory (DFT). This is based on a proof (Hohenberg and Kohn 1964) that electronic energy is determined by the electron density, independent of the number of

electrons, because the wavefunction is a functional[1] of the density. The energy E of the system is a functional of the density $\rho(r)$, where r are the electron coordinates ("functional of" is denoted by square brackets):

$$E[\rho(r)] = \int V_{ext}(r)\rho(r)dr + F[\rho(r)] \qquad (2.17)$$

where V_{ext} represents the interaction of the electrons with an external potential (typically the interaction with the nuclei), and $F[\rho(r)]$ is the sum of the kinetic energy of the electrons and the interelectronic interactions. The energy can then be solved using the variational theorem – the true density will give the minimum energy and any incorrect density will give an energy above the true energy. This expression was later expanded (Kohn and Sham 1965):

$$E[\rho(r)] = E_{KE}[\rho(r)] + E_H[\rho(r)] + E_{XC}[\rho(r)] + E_{EN}[\rho(r)] \qquad (2.18)$$

$$E_{KE}[\rho(r)] = \sum_{i=1}^{N} \int \psi_i(r)\left(-\frac{\nabla^2}{2}\right)\psi_i(r)dr \qquad (2.19)$$

$$E_H[\rho(r)] = \frac{1}{2}\iint \frac{\rho(r_1)\rho(r_2)}{|r_1 - r_2|}dr_1 dr_2 \qquad (2.20)$$

$$E_{EN}[\rho(r)] = -\sum_{i=1}^{N} \int \frac{Z_A}{|r - R_A|}\rho(r)dr \qquad (2.21)$$

$$\rho(r) = \sum_{i=1}^{N} |\psi_i(r)|^2 \qquad (2.22)$$

$E_{KE}[\rho(r)]$ is the kinetic energy, $E_H[\rho(r)]$ the electron-electron Coublombic energy, $E_{EN}[\rho(r)]$ the electron-nuclear energy, and $E_{XC}[\rho(r)]$ is the electronic exchange and

---

[1] A functional is a function of a function

correlation energy. R_A are the nuclear coordinates for atom A, and Z_A is the atomic number. By combining Equation 2.18 with Equation 2.22, the one-electron equation becomes:

$$[\varepsilon_{KE}(i) + \varepsilon_{EN}(i) + \varepsilon_H(i) + \varepsilon_{XC}(i)]\psi_i = \varepsilon(i)\psi_i \qquad (2.23)$$

where ε are the orbital energies. Equation 2.23 therefore gives the wavefunction ψ_i. An important aspect of this method is that the exchange energy is included implicitly as the energy is computed iteratively: $\varepsilon_{XC}(i)$ depends on $\rho(r)$, which depends on ψ_i, which in turn depend on $\varepsilon(i)$. In Chapter 4, DFT is used to energy minimise a tryptiminoquinone analogue and subsequently calculate its vibrational frequencies, using the B3LYP functional. This is the most popular DFT functional, a hybrid functional where the DFT exchange-correlation energy is calculated explicitly by including a term calculated from HF theory (Lewars 2003).

2.4. Semi-Empirical Quantum Mechanical Methods

The computational cost of HF calculations rises as the 4th power of the number of basis functions due to the number of 2-electron integrals. One approach to simplify the calculation is to only consider the valence electrons – those that are responsible for chemical processes. The core electrons are then included either by simply reducing the nuclear charge or by introducing functions to model the combined repulsion due to the nuclei and the core electrons. Semi-empirical methods further simplify the calculations by using only a minimum basis set – the minimum number

of functions necessary for accommodating the electrons is used for the valence electrons.

Semi-empirical QM methods utilise the Zero Differential Overlap (ZDO) approximation (Leach 2001), whereby most two-electron integrals are ignored. For four atomic orbitals (designated μ, v, λ, and σ) centred on four atoms (A, B, C, and D) the two electron integrals are of the form

$$\langle \mu v \mid \lambda \sigma \rangle = \iint \phi_\mu^A (1) \phi_v^B (1) \frac{1}{r_{12}} \phi_\lambda^C (2) \phi_\sigma^D (2) d\tau d\tau \qquad (2.24)$$

ZDO ignores integrals that contain $\phi_\mu^A (1) \phi_v^B (1)$ where $\mu \neq v$. Equation 2.24 thus becomes

$$\langle \mu v \mid \lambda \sigma \rangle = \delta_{\mu v} \delta_{\lambda \sigma} \langle \mu \mu \mid \lambda \lambda \rangle \ , \ \delta_{\mu v} = \begin{Bmatrix} 0, \mu \neq v \\ 1, \mu = v \end{Bmatrix} \qquad (2.25)$$

This approximation requires that the missing integrals be treated empirically. The effect of this simplification is that the overlap matrix **S** becomes a unity matrix, which simplifies the Roothaan-Hall equation from **FC = SCE** to **FC = CE**. For an N-electron system, this reduces the number of integrals from [N(N+1)/2][N(N+1)/2+1]/2 to N(N+1)/2 – from $\sim N^4/8$ to $\sim N^2/2$.

The calculations involving semi-empirical QM methods presented in this thesis were carried out using CHARMM (Brooks et al. 1983), version 27, using the built-in AM1 (Austin Model 1) semi-empirical QM method (Dewar *et al.* 1985). The AM1 method uses the Neglect of Diatomic Differential Overlap (NNDO)

approximation, which employs ZDO, except in cases where $A = B$ and $C = D$, i.e. when the basis functions for the first electron are on the same atom and the basis functions for the second electron are on the same atom. In other words, the products of basis functions that depend on the same electron coordinates are neglected when located on different atoms.

Other methods based on the NNDO approximation are MNDO (Modified Neglect of Diatomic Differential Overlap) and PM3 (Parametric Model 3). These all have certain common weaknesses; for example, weak interactions such as van der Waals interactions or hydrogen bonds are poorly predicted, and the rotational barriers for bonds with partly double bond character are significantly too low (Jensen 2001). MNDO was the first NNDO method, which resulted in certain systematic errors. This led to the development of AM1, which includes slightly different core-core potentials, and predicts much improved activation energies. The parametrisation of MNDO and AM1 were done manually, so relatively few reference compounds could be included. Later, parameterisation was automated (Stewart 1989) so that much larger training sets could be used. The resulting method was PM3 (Parametric Method 3), which includes more atom types than AM1 or MNDO, and contains the best set of parameters for the given set of experimental data (Jensen 2001). Nevertheless, PM3 has several known limitations, notably that almost all sp^3 nitrogens are predicted to be pyramidal, hydrogen bonds are ~0.1Å too short, and (most worryingly for simulations of the tryptiminoquinone intermediate) the charge on nitrogen atoms is often of "incorrect" sign and "unrealistic" magnitude (Jensen 2001). For potential-energy type calculations, some of these limitations can be overcome by using corrections based on higher levels of theory (as was done for the calculations reported in Section 1.5.3).

2.4.1. *Hybrid Quantum Mechanical / Molecular Mechanical Simulations*

When dealing with large molecular systems such as enzymes, it is necessary to treat most of the system molecular mechanically, but at the same time treat the reacting groups (e.g. the substrate and catalytic residues) quantum mechanically – typically using semi-empirical methods. In Chapter 5, QM/MM simulations are run on the AADH:tryptiminoquionone intermediate, with the tryptiminoquionone and catalytic aspartate residue treated quantum mechanically, so that the proton transfer event can be simulated within the enzyme environment. In these simulations, the QM region is treated using the AM1 method, while the rest of the system is treated using the CHARMM22 MM force field. There are bonds between the QM and MM regions, which means that there will be a cut-off between the QM and MM atoms. However, the bond orders of the atoms needs to be maintained. In other words, the electron density is terminated along the QM/MM bonds, while the interactions between bonded QM and MM atoms and their electron densities should resemble the interactions in a QM simulation of the entire system. In the QM/MM calculations reported in this thesis, HQ-type link atoms (Field *et al.* 1990) were employed to treat this QM/MM interface. These atoms behave exactly as QM hydrogen atoms in the QM scheme, and are invisible to the MM region, i.e. they are phantom atoms within the MM scheme.

2.5. Energy Minimisation

The potential energy surface (PES) can be thought of as a mountain range, with peaks and troughs representing maxima and minima in the energy landscape. For most simulations, it is necessary to locate the potential energy minimum, for example when

calculating the energy involved in a process such as a chemical reaction or a conformational change or when initiating an MD simulation. The enzyme-bound substrate used in this work is a model built from the crystal structure from a previous step in the mechanism (Section 3.3), so energy minimisation is required to remove any strain caused by changing the substrate structure and to ensure that the model is as accurate as possible. Energy minimisation – also known as geometry optimisation – is the process by which the system moves down-hill on the PES toward a minimum. For large molecules energy minimisation will not seek out the global minimum, but one of the nearer local minima.

A minimum on the PES corresponds to a stationary point where, for all atoms, the gradient g_i (the first derivative) of the potential energy V with respect to Cartesian coordinates x_i for atom i is equal to zero:

$$g_i = \frac{dV}{dx_i} = 0 \qquad (2.26)$$

The second derivative of the potential energy with respect to the coordinates represents the curvature of the PES in each gradient direction. For a system of N atoms, a $3N \times 3N$ matrix represents the forces between all pairs of atoms i and j – the so-called Hessian matrix:

$$H_{ij} = \frac{d^2V}{dx_i dx_j} \qquad (2.27)$$

Energy minimisation methods are classified as first derivative or second derivative methods on the basis of the highest derivative method used. Each type of

method has advantages and disadvantages, and it is common practice to use methods from each class in conjunction. The two methods used in this work are the steepest descent (SD) algorithm (Wiberg 1965), a first derivative method, and adopted-basis Raphson-Newton (ABNR) (Brooks et al. 1983), a second derivative method.

The SD algorithm minimises in the direction of the steepest slope on the PES. This is done by calculating the energy change caused by a small change in the position of each atom along one coordinate to derive an approximate value for the slope along that coordinate, and then changing each coordinate by a certain step size in the direction which reduces the energy. For every coordinate, if the step taken causes a decrease in the energy, the next step taken along that coordinate will be larger, while if the energy is increased the next step will be smaller. SD is a simple, rapid method for energy minimisation while the gradient is steep, and works well for the initial minimisation when the conformation is far from the minimum. However, this method does not converge very quickly, as progress becomes slower near the minimum

The ABNR algorithm (Brooks et al. 1983), developed from the Newton-Raphson method (Boyd 1968), approximates the potential energy function $V(x)$ in each iteration by the quadratic function given by the Taylor expansion:

$$V(x) = V(x_0) + (x - x_0)V'(x_0) + \frac{1}{2}(x - x_0)^2 V''(x_0) + \dots \qquad (2.28)$$

where $V(x)$ is the potential energy with respect to coordinates x, x_0 are the current coordinates, $V'(x_0)$ is the first derivative (the gradient) and $V''(x_0)$ the second derivative (the Hessian matrix) at x_0. At a minimum stationary point, $V'(x_0)$ is equal to

zero and $V''(x_0)$ is positive. The next set of coordinates x are found from the current coordinates x_0:

$$x = x_0 - \frac{V'(x_0)}{V''(x_0)} \qquad (2.29)$$

For large systems, where the function $V(x)$ has a large number of variables, the Newton-Raphson method becomes computationally expensive, as the Hessian matrix must be calculated at each step, but the ABNR algorithm limits the matrix equations to a subspace of smaller dimensionality, thus simplifying the computation.

2.5.1. Calculating Potential Energy Surfaces

For an N-atom system, the potential energy surface (PES) is 3N-dimensional (it is a function of the Cartesian coordinates of every atom). However, for a chemical reaction the dimensions of primary interest are those along the reaction coordinate, i.e. those coordinates that change as the system evolves from reaction to product. Therefore, it is useful to calculate the PES specifically along the reaction coordinate to obtain the energy barrier separating the reactants from the products and to observe any structural changes that occur as the system moves over this barrier. In Chapter 5, this is carried out by employing a stiff harmonic restraint to fix the reaction coordinate at consecutive, equally spaced values from reactant to product and energy minimising the system at each value. Since the reaction studied is a proton transfer reaction, the reaction coordinate, z, can be defined as:

$$z = d(\text{D-H}) - d(\text{A-H}) \qquad (2.30)$$

where $d(X\text{-}Y)$ is the distance between atoms X and Y, and D and A are the donor and acceptor atoms, respectively. This is a simplified reaction coordinate, but it does allow the remaining degrees of freedom in the system to change according to the changes in $d(\text{D-H})$ and $d(\text{A-H})$. This make it possible to study specifically the effects of bond-cleavage and bond-formation on the structure and potential energy of the system, but since only two degrees of freedom – $d(\text{D-H})$ and $d(\text{A-H})$ – are fixed, it becomes difficult to study the effect of the other degrees of freedom on the PES. These effects can be observed by calculating PESs for multiple structures obtained from an MD simulation (Section 2.6).

2.6. Molecular Dynamics Simulations

Molecular dynamics (MD) simulations are performed using classical mechanics, described by Newton's laws of motion. Newton's second law relates the force F_i exerted on a particle i to its mass m_i and acceleration a_i:

$$F_i = m_i a_i \qquad (2.31)$$

The force can be expressed as the derivative of the potential energy with respect to atomic coordinates, and the acceleration as the second derivative. The equation of motion then becomes:

$$-\frac{dV}{dr_i} = m_i \frac{d^2 r_i}{dt^2} \qquad (2.32)$$

MD simulations require an initial assignment of velocities – the MD simulations carried out in this work use a Gaussian distribution of velocities that conform to the total kinetic energy of the system, as determined by the initial temperature.

There is no analytical solution to Newton's law of motion, so these are solved numerically using finite difference methods where the coordinates and velocities at time t are used to calculate new values for time $t + dt$ where dt is the timestep. This is based on a Taylor expansion:

$$r(t + dt) = r(t) + v(t)dt + \frac{1}{2}a(t)dt^2 + ... \tag{2.33}$$

$$v(t + dt) = v(t) + a(t)dt + \frac{1}{2}b(t)dt^2 + ... \tag{2.34}$$

$$a(t + dt) = a(t) + b(t)dt + ... \tag{2.35}$$

where the velocity $v(t)$ at time t is the first derivative of the coordinates $r(t)$ and the acceleration $a(t)$ is the second derivative. The numerous MD algorithms differ in how they implement this basic expansion.

The MD simulations in this work use the leap-frog algorithm (Hockney and Eastwood 1981) using the CPT method of CHARMM (Constant Temperature and Pressure) based on the Berendsen method for temperature coupling (Berendsen *et al.* 1984). The leap-frog algorithm uses the equations:

$$r(t + \delta t) = r(t) + v\left(t + \frac{1}{2}\delta t\right)\delta t \tag{2.36}$$

$$v\left(t + \frac{1}{2}\delta t\right) = v\left(t - \frac{1}{2}\delta t\right) + a(t)\delta t \tag{2.37}$$

The velocities are first calculated at time $t + \frac{1}{2}\delta t$, and these are used to calculate the positions, r, at time $t+\delta t$. In this way, the velocities *leap* over the positions, then the positions *leap* over the velocities. The advantage of this algorithm is that the velocities are explicitly calculated – unlike, for example, the Verlet algorithm which uses the coordinates and accelerations, which leads to a loss of precision. However, the disadvantage is that they are not calculated at the same time as the positions, which means that a small timestep is required. The velocities at time t can be approximated by the relationship:

$$v(t) = \frac{1}{2}\left[v\left(t - \frac{1}{2}\delta t\right) + v\left(t + \frac{1}{2}\delta t\right)\right]$$
(2.38)

Another advantage of the leap-frog algorithm is that Berendsen temperature-coupling can be easily incorporated (Berendsen et al. 1984). In any MD simulation, the velocities have to be corrected at certain time intervals due to errors introduced by the limited precision of the algorithms. One way of correcting the velocities is using regular *ad hoc* rescaling based on the average temperature of the system, but this leads to discontinuities (Berendsen et al. 1984). The Berendsen method uses a weak coupling to an external bath with a reference temperature, and the algorithm is based on the equations governing collisions between the system and the external bath. The velocities are scaled at every step according to a coupling constant, τ_T:

$$\lambda = \left[1 + \frac{\delta t}{\tau_T}\left\{\frac{T_0}{T(t - \frac{1}{2}\delta t)}\right\}\right]^{1/2}$$
(2.39)

$$v'(t + \frac{1}{2}\delta t) = \lambda v(t + \frac{1}{2}\delta t)$$
(2.40)

where T_0 is the temperature of the bath, and T the temperature of the system. The velocity scaling factor λ is based on the temperature at t - $\frac{1}{2}\delta t$, but it can be used to scale the velocity $v(t + \frac{1}{2}\delta t)$ because of the slow variation of λ.

2.7. Methods of Analysis for MD Simulations

2.7.1. *Principal Components Analysis*

Principal Components Analysis (PCA) is a method for simplifying a data set by identifying the dimensions that represent as much of the data as possible. In essence, PCA reorients a multidimensional data matrix along orthogonal axes – the principal components – that represent consecutively smaller amounts of the overall data (Figure 2.1). A simple application would be the reorientation of a 3-dimensional protein structure, so that it can be displayed as a 2-dimensional image while retaining as much of the total structural information as possible. In this way, analysis of the original data set becomes much simpler, as the first principal components contain the most variability, and the principal components with little variability can be discarded.
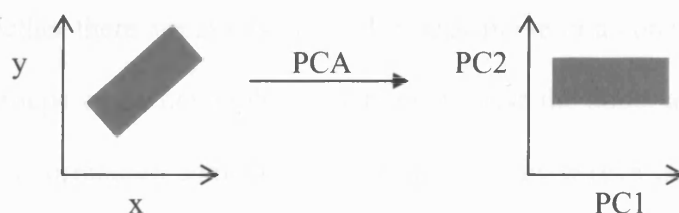
Figure 2.1. Illustration of PCA. The data set (grey rectangle) is reoriented along its principal components (PC1 and PC2).

PCA works by matrix diagonalisation. In general, a matrix A is related to its diagonal matrix by the equation:

$$A = P^{\mathrm{T}}DP \qquad (2.41)$$

where D is the diagonal matrix, P the transformation matrix relating A and D. P^{T} is the transposed (inverse) matrix of P. The columns of P ($p_{1,1\text{-}1,N}$, $p_{2,1\text{-}2,N}$ ...$p_{N,1\text{-}N,N}$) are the eigenvectors – i.e. the principal components – of A, and the diagonal elements of D ($d_{1,1}$, $d_{2,2}$...$d_{N,N}$) are the eigenvalues. The eigenvalue $d_{X,X}$ relates to how much of the total information of A is represented by the corresponding eigenvector $p_{1,X\text{-}N,X}$, and represent the projections of the original data onto this eigenvector.

2.7.2. Cross-Correlation Analysis

The degree to which the motions within a protein or enzyme are correlated can be used to identify regions that move in a concerted fashion, whether in opposite direction (negative correlation) or in the same direction (positive correlation). Cross-correlation is a technique by which the many-dimensional motions within an enzyme can be reduced to a 2-dimensional representation. In Chapter 3, this analysis is used to determine whether there are atoms or residues that move in a concerted fashion with the reacting groups, and whether these are likely to push the donor and acceptor atoms together. Cross correlation compares two vectors as they evolve through time during an MD simulation, and assigns a correlation coefficient between -1 (perfectly anti-correlated) and +1 (perfectly correlated) depending on how similar these vectors are over time. For two Cartesian positional vectors r_i and r_j for atoms i and j, the correlation coefficient $C(i,j)$ is given by:

$$C(i,j) = \frac{\langle r_i \cdot r_j \rangle - \langle r_i \rangle \langle r_j \rangle}{\left(\langle r_i^2 \rangle - \langle r_i \rangle^2 \right)^{1/2} \left(\langle r_j^2 \rangle - \langle r_j \rangle^2 \right)^{1/2}} \qquad (2.42)$$

The numerator is the covariance between the two vectors, and the denominator serves to normalize the value to within the -1 to +1 range. The vectors can correspond to individual atoms or centroids or centres of mass for groups of atoms, such as residues. The $C(i,j)$ elements can be collected in a matrix form, which can be displayed as a two-dimensional contour plot – a dynamical cross correlation map (DCCM) (Swaminathan *et al.* 1991) – where the contours indicate the magnitude of the $C(i,j)$ elements.

2.7.3. Spectral Density Analysis

A spectral density represents the frequencies present in a signal and their relative contributions to the signal, and can be used to analyse atomic velocities. The spectral density is based on the Fourier transform (FT) of the velocity autocorrelation function (VAF) for the signal. For a set x of N data points, the VAF is calculated as

$$C(\tau) = \frac{\sum_t x(t) \cdot x(t + \tau)}{\sum_t x(t) \cdot x(t)} \qquad (2.43)$$

The autocorrelation $C(\tau)$ measures the similarity between data points separated by the time intervals τ. The Spectral density is then obtained by the discrete FT of the $C(\tau)$, which converts it from the time domain to the frequency domain:

$$J(k) = \frac{1}{N} \sum_{n=0}^{N-1} C(\tau) e^{2\pi i n k / N} \quad ; \quad k = 0 \dots , N\text{-}1 \qquad (2.44)$$

where N is the total number of frames sampled during the MD simulations. The frequency ω, in cm^{-1}, is equivalent to k/N, where k is an integer value between 0 and N-1. The spectral density $J(\omega)$ is in fact the magnitude of $J(k)$, which is a complex number. The real and imaginary parts of $J(k)$ are calculated separately by using the following equivalence:

$$e^{i\theta} = \cos(\theta) - i \sin(\theta) \qquad (2.45)$$

In Chapter 4, several types of spectral densities are discussed, which use different data sets. To determine the vibrational frequencies involved in the three-dimensional motions of specific atoms, atomic velocity spectral densities are calculated, where x_n is a set of velocities calculated from the difference in coordinates sampled at regular intervals during an MD simulation. The frequencies at which two atoms are pushed towards each other is determined from a so-called relative velocity spectral density, obtained by the FT of the VAF for the projected velocity $r_{1,2}$ obtained by projecting the relative velocity $v_{1,2}$ onto the unit vector $u_{1,2}$ along their interatomic axis ($r_{1,2} = v_{1,2} \cdot u_{1,2}$). Finally, the frequencies at which the reaction coordinate is modulated are analysed by the spectral density for the reaction coordinate, s, defined as

$$s = r_H - \frac{m_D r_D + m_A r_A}{m_D + m_A} \qquad (2.46)$$

This analysis is based on that developed by Schwartz and co-workers to diagnose a promoting vibration in enzymes (Caratzoulas and Schwartz 2001; Caratzoulas et al. 2002). Their analysis is based on the theory that a vibration that is symmetrically coupled to the reaction coordinate will increase in magnitude with s, and vanish at (or close to) the transition state. This follows from the fact that the transition state is missing one degree of freedom along the reaction coordinate (Section 1.1.1.). In their analysis, Schwartz and co-workers compare the spectral densities for the reactant and product states to that of the point of minimum coupling – the point at which the coupling between the gating mode and the reaction coordinate is minimised – where, in their case, the proton is half-way between the donor and acceptor atoms. This is to ensure that the gating frequency does in fact disappear as the system approaches the transition state, and that it is strongly coupled to the reaction coordinate on either side of the transition state. In the analysis presented in Chapter 4 of this thesis, however, only the reactant spectral densities are obtained, since this avoids the time-consuming process of re-parameterising the charges and force constants for the point of minimum coupling and the product, and because of the practical difficulty of restraining the system at the point of minimum coupling without simultaneously dampening the vibrations involving the donor, acceptor and transferring proton. Instead, whether or not a particular vibration is symmetrically coupled to the reaction coordinate can be determined by analysing the vectors obtained from digital filtering by frequency deconvolution (Section 2.7.4) of the velocities of the atoms of interest, as discussed in Chapter 4.

2.7.4. Digital Filtering by Frequency Deconvolution

To analyse motions of specific frequencies, an algorithm based on the method by Osguthorpe and co-workers (Sessions *et al.* 1989) was employed. This method uses the discrete Fourier transform to convert the velocities along the x, y and z axes into separate spectral densities, then removes unwanted frequencies and converts the resulting spectral densities into new velocities by inverse Fourier transformation. These velocities are converted to coordinates by applying the velocities to selected atomic coordinates. The equations for the discrete FT for a set $x(n)$ of N data points, and the corresponding inverse FT are:

$$\text{FT: } J(k) = \frac{1}{N} \sum_{n=0}^{N-1} x(n) e^{2\pi i n k / N} \tag{2.47}$$

$$\text{Inverse FT: } x(n) = \frac{1}{N} \sum_{n=0}^{N-1} J(k) e^{-2\pi i n k / N} \tag{2.48}$$

This method allows a three-dimensional representation of motions occurring within a particular frequency range, and is therefore complementary the spectral density analysis discussed in Section 2.7.3. In particular, comparing the motions of the reacting atoms in the same frequency range will reveal whether they move in phase towards and away from the transition state, which is required for a gating mode since it must be symmetrically coupled to the reaction coordinate (Caratzoulas and Schwartz 2001).

3. Long Timescale Molecular Dynamics Simulations

3.1. Preface

As discussed in Section 1.5.2, the kinetic data suggests that the abstraction of H1 (Figure 1.8) from C1 of the tryptiminoquinone adduct by neighbouring Asp128β occurs by a vibrationally assisted tunneling mechanism. VTST/MT calculations of the proton transfer event support this conclusion and revealed that one of the two carboxyl oxygens of Asp128β, O2, is the preferred proton acceptor, and that 99.9% of the proton transfer to O2 occurs by tunneling following an initial structural rearrangement (Masgrau et al. 2006). Proton transfer to O1 is also possible, although this requires an initial stretching of the C1-H1 bond, and is less favourable both kinetically and thermodynamically (Masgrau et al. 2006). These calculations confirm the tunneling mechanism, and the necessary structural rearrangement explains the strong temperature dependence of the rate of proton transfer, but they do not explain how this structural rearrangement occurs.

To fully understand the mechanism of vibrationally assisted tunneling in enzymes, it is necessary to determine how enzyme motion affects the structure of the active site, and in particular the distance between the proton and the acceptor atom. This distance is critical for the tunneling probability, and therefore motions that reduce this distance are good candidates for motions that promote tunneling. These motions can lie anywhere from the sub-picosecond timescale (vibrations of individual atoms and functional groups) to the nanosecond timescale (domain motions). There is evidence for the involvement of both of these timescales in driving chemical reactions in enzymes, even within the same enzyme, e.g. (Radkiewicz and Brooks 2000; Agarwal et al. 2002b). Therefore, to study the motions in AADH:tryptiminoquinone on the picosecond to nanosecond timescale, and in particular their impact on the proton-acceptor distance, unrestrained multi-nanosecond molecular dynamics (MD)

simulations were run. Since *ab-initio* quantum mechanical (QM) methods or semi-empirical QM methods are computationally too expensive for running MD simulations on such long timescales, molecular mechanics (MM) was used in their stead.

3.2. Parameterisation of Tryptiminoquinone for the Molecular Mechanics Force Field

All MM calculations were carried out using CHARMM (Brooks et al. 1983), version 27, with the CHARMM22 force field (MacKerell et al. 1998). Molecular mechanics treats atoms as solid particles with constant charge and bonds as rigid springs, with specific force constants for the bond lengths, bond angles and dihedral angles. The CHARMM force field uses specific charges and force constants for specific atoms and atom combinations. The 20 natural amino acids are pre-parameterised, as are certain other common groups, but it is necessary to parameterise the tryptiminoquinone. The force constants were defined by analogy, by comparing the atom types and bonding to those defined in existing amino acid residues. The charges, on the other hand, were parameterised independently, since the electronic properties of the quinone, which pulls electron density away from the donor carbon, are not analogous to any of the existing parameterised groups.

To determine the best charges for the tryptiminoquinone, *ab initio* quantum mechanical (QM) calculations of iminoquinone **A** (Figure 3.1a) were first performed using Gaussian 98 (Frisch *et al.* 2002) using the restricted Hartree-Fock level of theory with the 3-21G* basis set. The MM charges were then manually optimised iteratively so that the calculated energies of interaction with a single water molecule in various positions and orientations agree with those from the QM calculations.
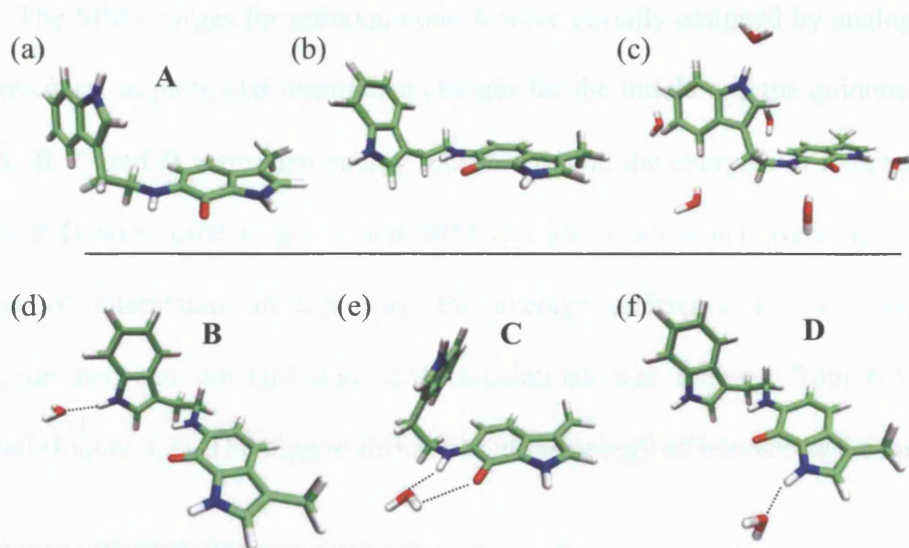
Figure 3.1. Iminoquinone structure used for parameterization calculations. (a) Coordinates from crystal structure, with protons added; (b) structure after QM energy minimization; (c) relative orientation of water molecules used to calculate the energies of interaction; (d,e,f) the three structures, **B**, **C** and **D** from minimising **A** with a single water molecule.

The first QM minimisation was carried out using the coordinates obtained from the crystal structure. (Figure 3.1a). The energy minimised structure of **A** (Figure 3.1b) is quite different from that in the enzyme, but this is not important since the parameterisation aims to obtain MM parameters that will allow the MM force field to mimic the QM calculations, not to mimic the effect of the enzyme on the structure. A water molecule was then placed in seven different positions around the iminoquinone (Fig. 3.1c), to give seven structures with one water molecule for energy minimisation. These yielded three different energy minimised structures with the water molecule interacting with one of the hydrogen bond donor/acceptor groups – structures **B**, **C** and **D** (Figure 3.1d,e,f). By comparing the energy of a minimised water molecule and minimised molecule **A** with the energies of these three structures, the energies of interaction were obtained, and these were then used as the points of reference for the MM charge parameterisation.

The MM charges for iminoquinone **A** were initially assigned by analogy from other residues, in particular tryptophan charges for the indole and the quinone (Table 3.1). **A**, **B**, **C** and **D** were then energy minimised, and the energies of interaction for **B**, **C** and **D** were used to guess new MM charges, from which were derived new energies of interaction. In this way, the average difference in the energies of interaction between the QM and MM calculations was reduced from 6.4 to 1.0 kcal/mol (Figure 3.2). The biggest difference in the energy of interaction was obtained

	G98 Mull	MM Initial	MM Final
C1	-0.50699	-0.27	-0.27
H1	0.20563	0.09	0.09
H2	0.198449	0.09	0.09
H3	0.198365	0.09	0.09
C2	-0.02845	-0.03	-0.03
C3	0.06474	0.035	0.035
H4	0.269316	0.115	0.115
N1	-0.76183	-0.61	-0.61
H5	0.439432	0.38	0.48
C4	0.209667	0.13	0.03
C5	-0.07717	-0.02	-0.02
C6	-0.07457	-0.115	-0.115
H6	0.283075	0.115	0.115
C7	-0.27842	-0.115	-0.115
H7	0.267535	0.115	0.115
C8	0.543826	0.31	0.63
O1	-0.5292	-0.31	-0.35
C9	0.39549	0.57	0.2
N2	-0.74025	-0.5	-0.55
H8	0.471672	0.45	0.3
C10	-0.1353	0.3	0.49
H9	0.219678	0.09	0.14
H10	0.236752	0.09	0.14
C11	-0.37141	-0.18	-0.18
H11	0.205828	0.09	0.09
H12	0.227708	0.09	0.09
C12	-0.09875	-0.03	-0.12
C13	0.04909	0.035	-0.015
H13	0.235733	0.115	0.115
N3	-0.82995	-0.61	-0.355
H14	0.408175	0.38	0.38
C14	0.33064	0.13	0.035
C15	-0.03894	-0.02	-0.04
C16	-0.20879	-0.115	-0.115
H15	0.222703	0.115	0.115
C17	-0.21724	-0.115	-0.115
H16	0.214026	0.115	0.115
C18	-0.20739	-0.115	-0.115
H17	0.220499	0.115	0.115
C19	-0.20961	-0.115	-0.115
H18	0.196215	0.115	0.115
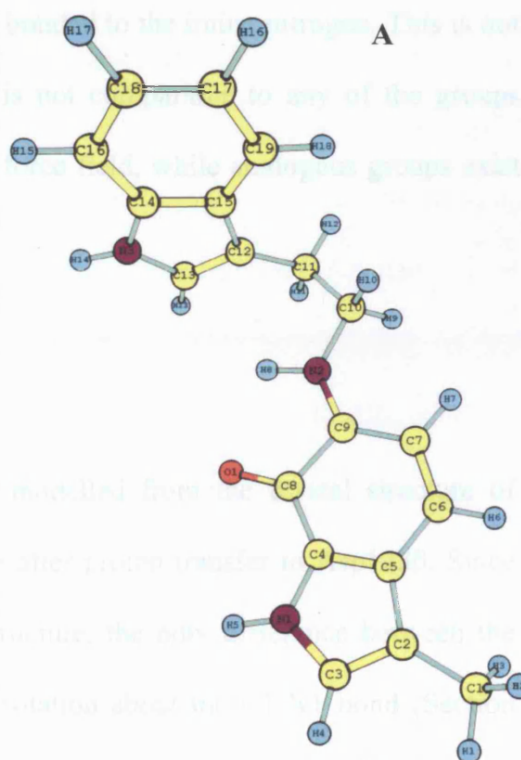
Table 3.1. Charges for iminoquinone analogue **A**: Mulliken charges from RHF/3-21G* minimization (G98 Mull), the initial guess for the MM charges (MM Initial) and the final charges (MMFinal) after iteratively deriving new charges. The enclosed areas represent groups with integer charges in the CHARMM topology.

(a)

(b)
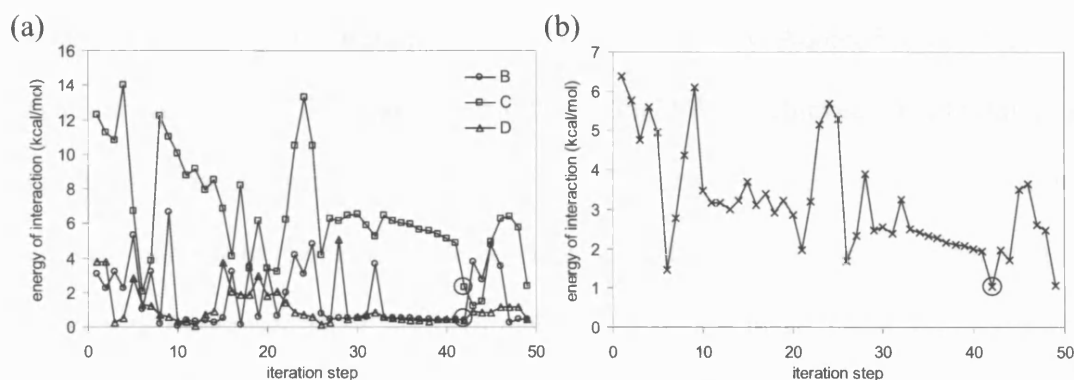
Figure 3.2. Difference in the energies of interaction calculated using RHF/3-21G* and the CHARMM22 force field with different atomic charges. (a) The absolute difference for iminoquinone **A** and a single water molecule in positions **B**, **C** and **D** (Figure 3.1); (b) the average absolute difference in energy of interaction for **B**, **C** and **D**. The energy differences for the selected charges are circled.

for structure **C**, where the water is hydrogen bonded to the imine nitrogen. This is not surprising, as this electron deficient imine is not comparable to any of the groups already parameterised for the CHARMM22 force field, while analogous groups exist for the rest of the structure.

3.3. System Setup

The AADH-bound tryptiminoquinone was modelled from the crystal structure of intermediate V (Section 1.5.1), the structure after proton transfer to Asp128β. Since hydrogens are not present in this crystal structure, the only difference between the tryptiminoquinone and intermediate V is a rotation about the C1-N1 bond (Section 1.5.1). Therefore no change in the structure and bonding was required – by defining the correct atom types and bonding the automatic addition of hydrogen atoms by CHARMM and the subsequent energy minimisation forces the structure to the correct tryptiminoquinone geometry.

The enzyme system for all MM simulations was set up according to the same general protocol, at a temperature of 300 K and using a non-bonded cut-off of 13 Å (all energy minimizations, unless otherwise specified, are by steepest descent (SD)

until a gradient of 0.2 kcal/mol/Å is achieved then by Adopted Basis Newton-Raphson (ABNR) until a gradient of 0.01 kcal/mol/Å is achieved): (1) building all hydrogen atoms according to the internal coordinates (IC) tables for each residue and applying patches to create disulfide bonds and the TTQ adduct (see next paragraph); (2) energy minimisation of the hydrogen atoms (i.e. with all other atom positions fixed); (3) addition of the water sphere for solvation, removing all water molecules for which the oxygen atom lies within 2.6Å of another heavy atom to avoid any steric clashes; (4) energy minimisation of the water molecules; (5) 5 ps Langevin molecular dynamics of the water molecules using the leapfrog algorithm, with initial 1 ps heating to 300 K; (6) further energy minimisation of the water molecules by ABNR until a gradient of 0.01 kcal/mol/Å is achieved; (7) energy minimisation of everything except the backbone atoms; (8) energy minimisation with a harmonic constraint of 50 kcal/mol/Å^2 on the backbone atoms and a constraint of 25 kcal/mol/Å^2 on the sidechain heavy atoms; (9) energy minimization of the entire system with no constraints. For a system that did not include solvation water, steps (3) to (6) were omitted.

A patch was used to create the TTQ adduct from the iminoquinone and Trp160β. This removes H6 of the iminoquinone (see Figure 3.1) and the appropriate hydrogen of Trp160β, evenly distributes the charges from the two hydrogens among the corresponding carbons, and adds a bond between C6 of the iminoquinone and the appropriate carbon of Trp160β.

3.4. MD Simulations of a Solvated AADH Heterodimer

Ideally, MD simulations would be run for the entire solvated enzyme. However, AADH is a very large $\alpha_2\beta_2$ heterotetrameric enzyme, with 939 residues in the crystal structure, and running a simulation with the entire enzyme plus solvation water would be computationally very expensive. The first simulation therefore involved only one $\alpha\beta$ heterodimer, including the crystal waters that are within 5Å of residues of this dimer, solvated in a solvation sphere of 90 Å diameter. Unfortunately, the two heterodimers are not entirely structurally independent, as the N-terminus residues from each α subunit are hydrogen-bonded to a β-sheet from the β subunit from the other heterodimer (Figure 3.3a). Before setting up the heterodimer system, it is necessary to remove the first 8 residues of the α subunit (Figure 3.3b) since this strand will not behave as in the $\alpha_2\beta_2$ heterotetramer and will stick out of the solvation sphere.

After the initial set-up a 3 ns MD simulation was run at 300 K using the CPT algorithm (Constant Temperature and Pressure, based on the Berendsen algorithm),
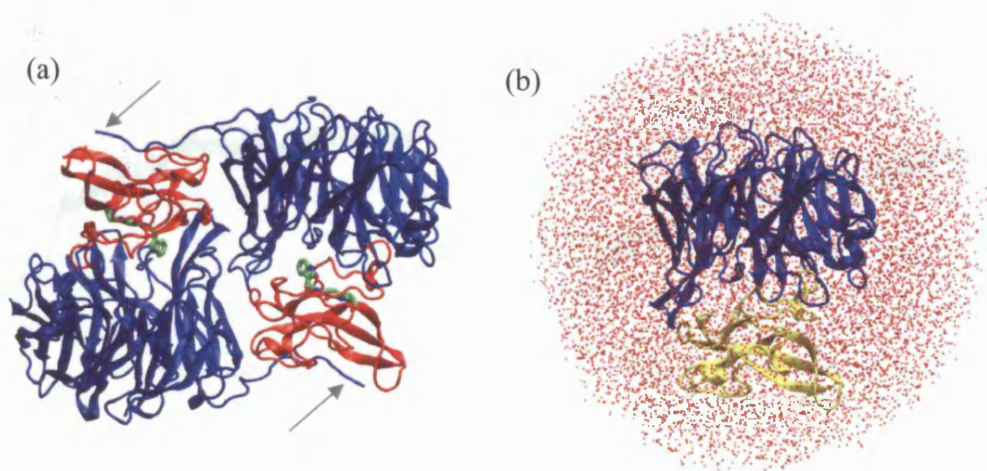
Figure 3.3. (a) Crystal structure of the AADH $\alpha_2\beta_2$ heterotetramer (α, blue; β, red) with tryptiminoquinone shown as sticks; the N-terminus of the α subunits are indicated by arrows. (b) Energy minimised solvated $\alpha\beta$ heterodimer (α, blue; β, yellow)

using a non-bonded cut-off of 14 Å and a timestep of 1 fs. Since this is different from the 12 Å cut-off used in the set-up, the system was first energy minimised using SD until a gradient of 0.2 kcal/mol/Å was achieved then by ABNR until a gradient of 0.01 kcal/mol/Å was achieved. The system was then thermalised from 100 K to 300 K for 20 ps, increasing the temperature by 5 K every 50 fs. The analysis run after thermalisation was 3 ns, and a temperature coupling constant of 5.0 ps was used for the entire simulation.

Initial analysis of the all-C_α RMS deviation during this MD simulation suggested that the system was equilibrated after about 1 ns, when the RMS deviation settles at about 1.6 Å (Figure 3.4a). However, after calculating the C_α RMS deviations for the β subunit, it became clear that this was not the case (Figure 3.4b), as this RMS deviation increases steadily during the entire simulation. It is not very surprising that the β subunit is the most problematic for this simulation, since a part of the tertiary structure is missing (see above). Indeed, this RMS "drift" appears to correspond to an "unzipping" from this β-sheet of the now-exposed strand which, in the heterotetramer, would be hydrogen-bonded to the N-terminus residues from the α subunit of the other dimer (Figure 3.5).
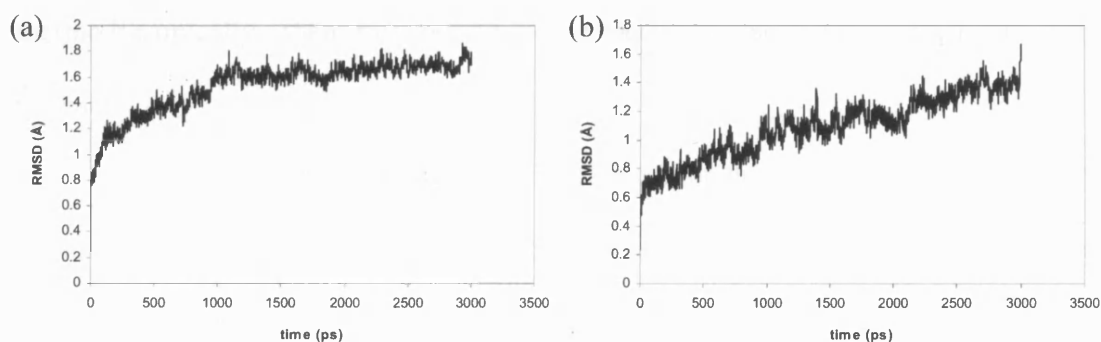
Figure 3.4. (a) all-C_α and (b) β subunit C_α RMS deviation for 3 ns MD simulation of a solvated AADH αβ heterodimer.
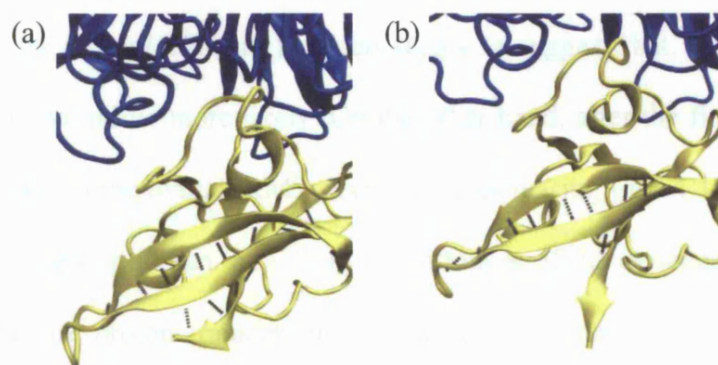
Figure 3.5. Hydrogen bonding (black broken tubes) in the β-sheet of the β subunit (a) in the minimized structutre and (b) after 3 ns of MD simulation.

3.4.1. *Donor/Proton-Acceptor Distances*

Taking this RMS drift into account, it is still interesting to study the active site motions to gain insight into the nature of the local motions that might compress the donor-acceptor distance. As discussed in the Preface, O2 has been shown by computational analysis of the proton transfer step to be the preferred acceptor, and mechanistically proton transfer to O2 will facilitate the next step in the reaction cycle (see Section 1.6.1). However, to study how the enzyme dynamics might promote the reaction, both Asp128β carboxyl oxygens will be considered, since it is expected that, if proton transfer to O2 is preferred dynamically as well as kinetically and thermodynamically, then this would be reflected in the relative C1/H1-O1/O2 distances.

The C1/H1-O1/O2 distances were measured for the full 3 ns simulation after thermalisation (Figure 3.6a,b). The equilibrium C1-O1/O2 distances are longer than the crystallographic distances (3.0/3.4 Å *c.f.* 2.8/3.0 Å), and the equilibrium C1/H1-O1/O2 distances are all longer than the values for the reactant structure from VTST/MT simulations of the proton transfer (Section 1.5.3) (Masgrau et al. 2006). The C1/H1-O1 distances are on average shorter than the C1/H1-O2 distances (in

accord with the crystal structure), which seems to suggest that, on average, proton transfer to O1 would be more likely. On the other hand, after the first nanosecond of MD (before which the overall RMS deviation is increasing), the C1/H1-O2 distances fluctuate more strongly than the C1/H1-O1 distances. If the dynamics did play a role in promoting the proton transfer, then it makes sense that there would be larger fluctuations in the distance for the favoured proton acceptor – although shorter C1/H1-O2 distances would also be expected.

Another significant difference between the H1-O1 and H1-O2 distances is the correlation between the H1-O2 distance and the indole-quinone angle that describes the orientation of the indole relative to the quinone, which is absent for H1-O1 (Figure 3.6c,d). It is therefore possible that the motion of the indole that reduces this angle somehow pushes C1/H1 towards O2. However, the spread of H1-O2 distances at any given indole-quinone angle is very large; for example, the lowest distances of ~2.2Å are achieved when the angle is < ~110°, but these angles also corresponds to distances up to ~3 Å. Therefore, the indole-quinone angle does not drive the minimisation of the H1-O2 distance: a relatively low angle is necessary, but not sufficient, to minimise the distance. In other words, reducing the angle to ~110° ensures that the H1-O2 distance will lie mainly below ~3 Å, but reducing it further will not further reduce the distance.
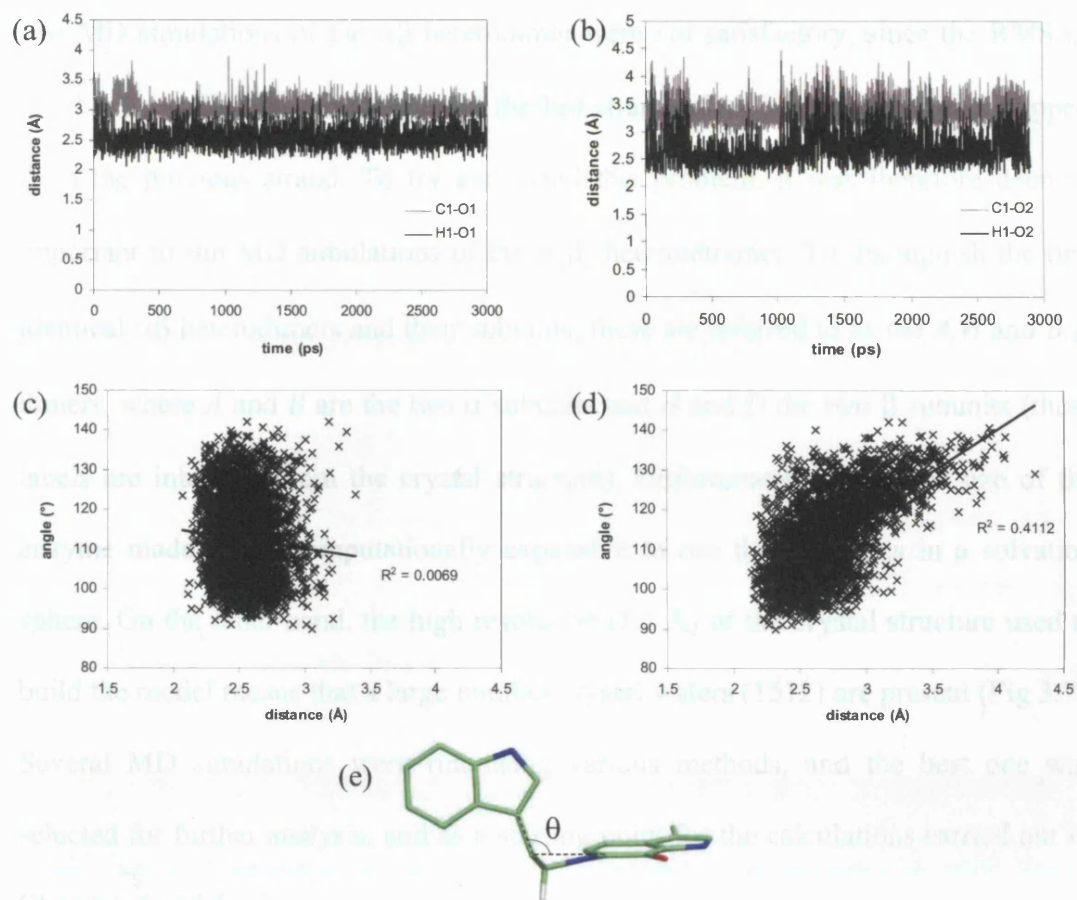
Figure 3.6. (a) C1/H1-O1 and (b) C1/H1-O2 distances *versus* time and indole-quinone angle (θ) versus (c) H1-O1 and (d) H1-O2 distances; (e) definition of the indole-quinone angle.

3.5. MD Simulations of the AADH Heterotetramer

The MD simulations of the αβ heterodimer were not satisfactory, since the RMS of the β subunit did not equilibrate and the last strand of its β-sheet becomes unzipped from the previous strand. To try and avoid this problem, it was therefore deemed important to run MD simulations of the $\alpha_2\beta_2$ heterotetramer. To distinguish the two identical αβ heterodimers and their subunits, these are referred to as the *A,H* and *B,D* dimers, where *A* and *B* are the two α subunits and *H* and *D* the two β subunits (these labels are inherited from the crystal structure). Unfortunately, the large size of the enzyme made it too computationally expensive to run the dynamics in a solvation sphere. On the other hand, the high resolution (1.1 Å) of the crystal structure used to build the model means that a large number crystal waters (1512) are present (Fig 3.7).

Several MD simulations were run using various methods, and the best one was selected for further analysis, and as a starting point for the calculations carried out in Chapters 4 and 5.

The best MD simulation was obtained using the CPT algorithm with a distance dependent dielectric ($\propto r_{ij}$), using an ε_{ij}-value of 1.0 (ε_{ij} is the dielectric constant at
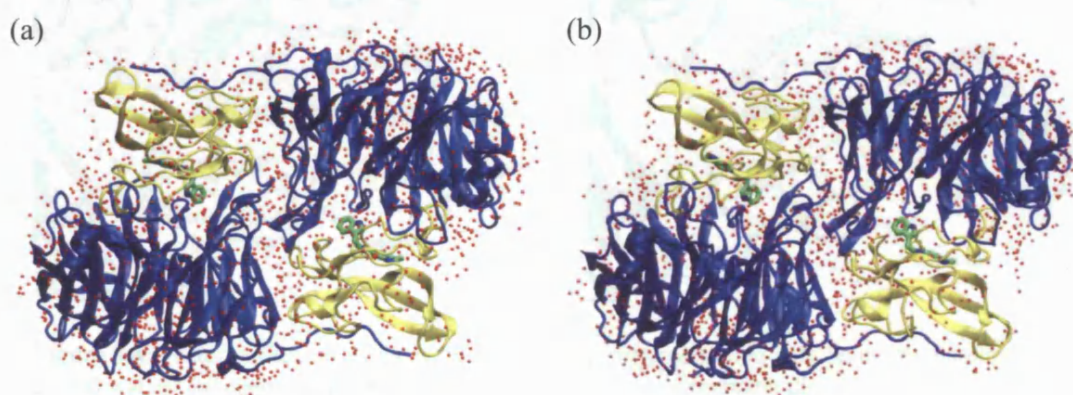
Figure 3.7. Structure of AADH heterotetramer model with bound tryptamine and crystal waters, (a) energy minimized with a distance-dependent dielectric ($\varepsilon = 1$) and (b) after 7ns of CPT MD simulation. The tryptiminoquinones are shown as green sticks.

zero separation; see Equation 2.8), employing SHAKE so that a 2 fs timestep could be employed, with thermalisation from 0 to 300 K over 24 ps, increasing the temperatureby 5 K every 400 fs. Using a higher ε_{ij}-value of 2.0, most of the water molecules rapidly escaped from the enzyme due to the weaker electrostatic interactions, and the A subunit α-helix unfolds within 1 ns and both β subunit β sheets start to "unzip" within 2 ns. Furthermore, both tryptiminoquinones undergo a radical conformational change in both dimers, because the sidechain of Phe97α rotates away from the active site (Figure 3.8b). This rotation does not occur if water is present, presumably because of the hydrophobicity of Phe97α. Using a dielectric constant of 1.0, all crystal waters remained around the enzyme (Figure 3.7b) and this conformational change was avoided.
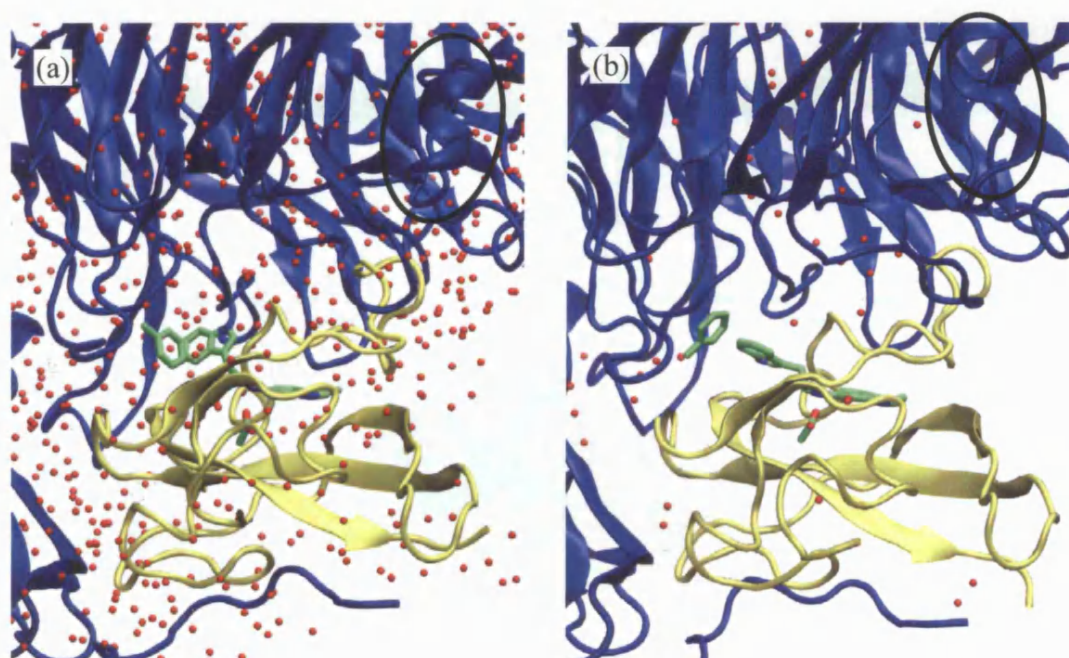
Figure 3.8. Focus on the A,H dimer of the AADH $\alpha_2\beta_2$ heterotetramer with bound tryptamine and crystal waters: (a) energy minimised structure with a distance-dependent dielectric ($\varepsilon = 2$) and (b) after 2.5 ns CPT MD. The simulation. The iminoquinone, Asp128β and Phe97α sidechains are shown as sticks. The α-helix of the A subunit is indicated by the black ovals.
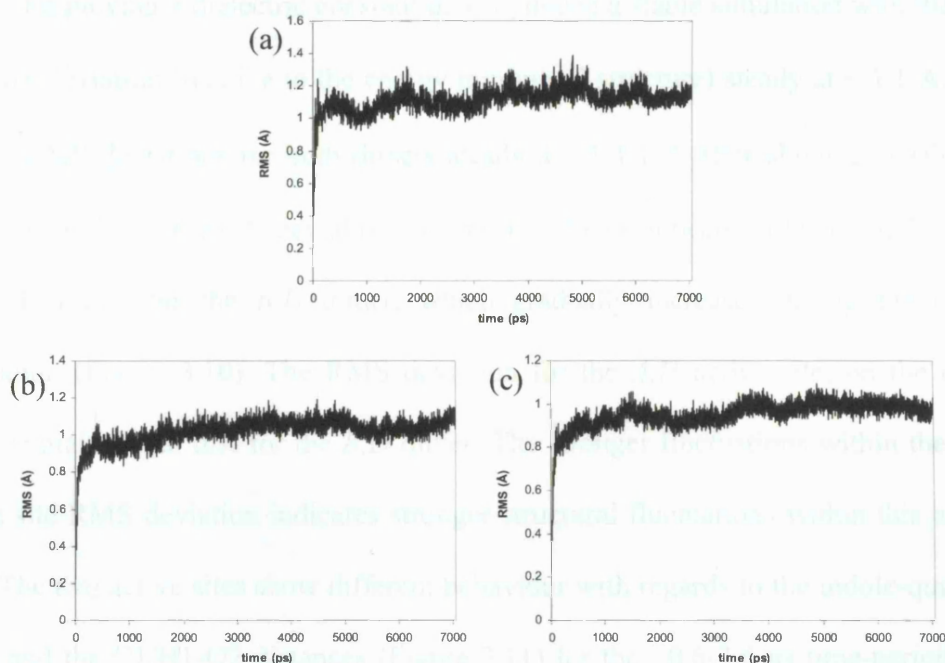
Figure 3.9. RMS deviations for 7 ns MD simulation of the AADH:tryptiminoquinone heterotetramer, including thermalisation: (a) All-Cα, (b) *A,H* Cα, (c) *B,D* Cα.
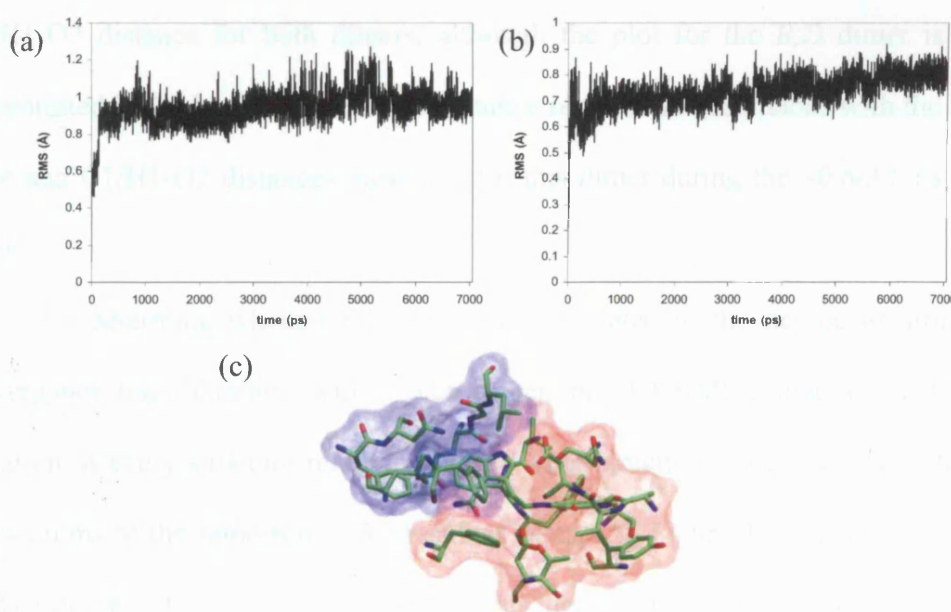
Figure 3.10. Active site RMS deviations for the two αβ heterodimers during the 7 ns MD simulation of the AADH:tryptiminoquinone heterotetramer, including thermalisation: (a) the *A,H* dimer , (b) the *B,D* dimer, (c) active site residues used in the analysis (illustration from *A,H*), with the solvent accessible surfaces for the α and β subunits (except the tryptiminoquinone) shown in blue and red respectively: D128β, T172β, F169β, W160β, Y126β, V158β, N159β, A82β, V83β, D84β, F97α, F100α, F123α, N124α, Q177α, G178α, L179α.

Employing a dielectric constant of 1.0 yielded a stable simulation with the all-C_α RMS deviation (relative to the energy minimised structure) steady at ~ 1.1 Å, and the C_α RMS deviations for both dimers steady at ~1-1.1 Å after about 2 ns (Figure 3.9). The active site RMS deviation for the *A,H* dimer appears to have equilibrated more than that for the *B,D* dimer, which gradually increases during the entire simulation (Figure 3.10). The RMS deviation for the *A,H* active site, on the other hand, is higher than that for the *B,D* dimer. The stronger fluctuations within the *A,H* active site RMS deviation indicates stronger structural fluctuations within this active site. The two active sites show different behaviour with regards to the indole-quinone angle and the C1/H1-O2 distances (Figure 3.11) for the ~0.6-3.6 ns time-period, the *A,H* active site showing similar behaviour to that for the dimer (Section 3.4.2). Measuring the indole-quinone angle (Figure 3.11e,f) reveals a similar correlation with the H1-O2 distance for both dimers, although the plot for the *B,D* dimer is more concentrated in the lower-angle, lower-distance region, in concordance with the lower angle and C1/H1-O2 distances measured for this dimer during the ~0.6-3.6 ns time-period.

To determine whether this difference is related to the degree of structural convergence (equilibration) within each dimer, the 2D RMSD matrix – the RMS deviation of every structure relative to every other structure – was calculated for the heavy atoms of the same active site residues as used in Figure 3.12, sampled every 2 ps. The degree of structural convergence can then be determined by comparing the first principal component (PC1) vector for subsequent segments from the 2D RMSD matrix. In essence, these vectors represent the similarity between the structures represented by each segment of the simulation and all the structures; if this vector is different for different segments, then the structures within these segments are
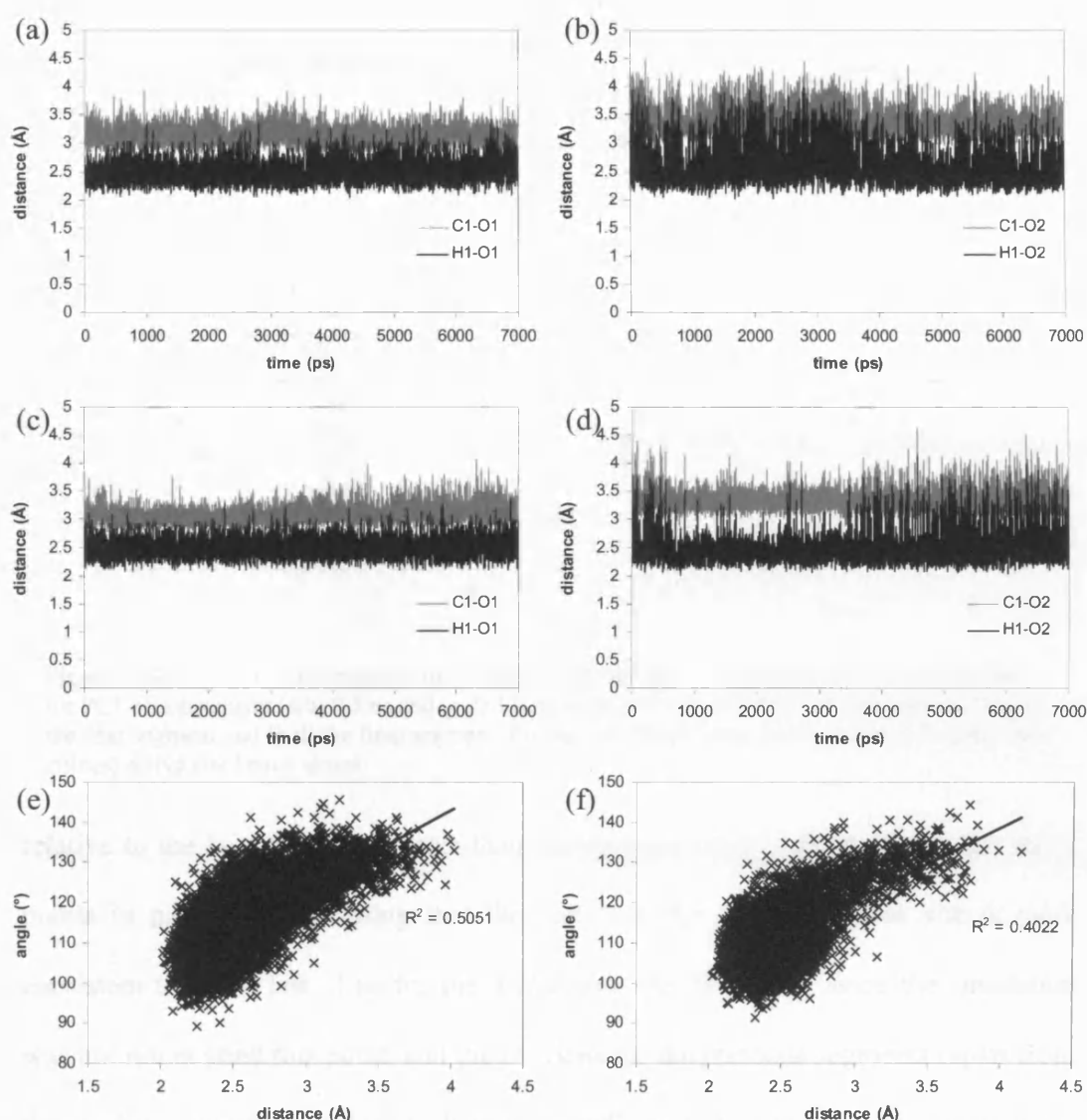
Figure 3.11. (a,b,c,d) C1/H1-O1/O2 distances for both dimers of AADH: (a) *A,H* C1/H1-O1, (b) *A,H* C1/H2-O2, (c) *B,D* C1/H1-O1, (d) *B,D* C1/H2-O2; (e,f) indole-quinone angle *versus* H1-O2 distances for the (a) *A,H* and (f) *B,D* dimer (the angle is defined in Figure 3.6e).

different. The vector overlap (normalised cosine) for each of these vectors relative to the vector for the next segment, as well as the overlap relative to the final segment were calculated, the former representing how similar each segment is to the next, and the latter how similar each is to the last. The results are shown in Figure 3.12 for 0.5 and 1.0 ns segments. For each segment of both active sites, PC1 represents ~17-20% of the data for the 1.0 ns segments and ~20-25% for the 0.5 ns segments. In each case the *A,H* active site is the most strongly converged; the overlap for the *B,D* vectors

83
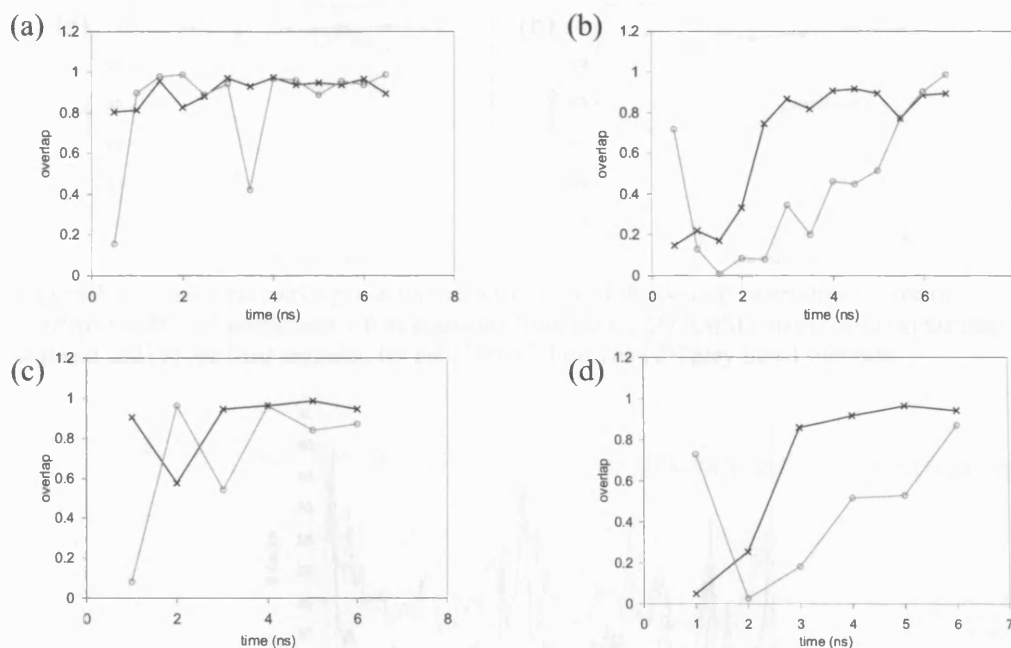
Figure 3.12. Structural convergence for C_α motion for the two $\alpha\beta$ heterodimers: vector overlaps for PC1 of subsequent (a,b) 0.5 ns and (c,d) 1.0 ns segments from the 2D RMSD matrix with (a,c) the next segment and (b,d) the final segment, for the *A,H* (black lines, crosses) and *B,D* (grey lines, cirlces) active site heavy atoms.

relative to the last vector is greater than the corresponding *A,H* vector for the last 2 points in panel (b), indicating that the last 1 ns for the *B,D* active site is more consistent than the last 1 ns for the *A,H* active site. However, since the simulation was not run beyond this point, and the overlaps for the previous segments (apart from the first) are significantly lower, there is no indication that this last 1 ns has actually converged. For the *A,H* active site, on the other hand, the last 5 ns show strong convergence.

The structural convergence for the β subunits were also measured, using 1 ns segments from the C_α 2D RMSD matrix (Figure 3.13), since cross-correlation analysis of the β subunit is carried out in Section 3.5.1. PC1 for the *H* subunit represent ~37-45% of the data and ~18-21% for the D subunit. The plots show the same trends as those for the active sites, with the *H* subunit strongly converged but not the *D* subunit. That the *H* subunit and *A,H* active site are more strongly converged

84
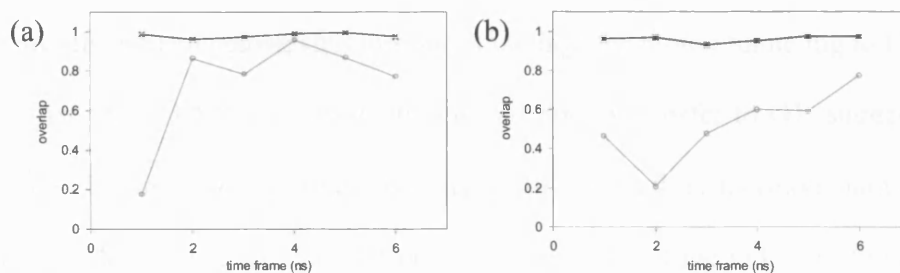
Figure 3.13. Structural convergence for the active sites of the two αβ heterodimers: vector overlaps for PC1 of subsequent 1.0 ns segments from the C_α 2D RMSD matrix with (a) the next segment and (b) the final segment, for the H (black lines) and D (grey lines) subunits.
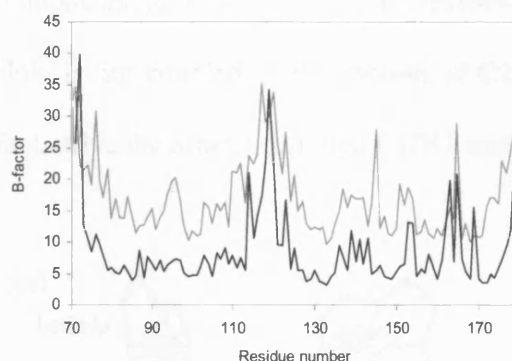
Figure 3.14. Computed b-factors (back line) and crystallographic b-factors (grey lines).

than the D subunit and B,D active site is further supported by unrestrained QM/MM MD simulations, started from a structure taken after 2 ns of the current MD simulation (Chapter 5) where the indole-quinone angle and O2-C1/H1 distances for both dimers show spreads of values similar to the A,H dimer. In view of this, the A,H dimer was chosen for all subsequent analyses. Comparing the H subunit crystallographic B-factors, which represent the mobility of each residue, with the computed B-factors (from the diagonal elements in the covariance matrix) for the 2-7 ns time period further validates the MD simulation (Figure 3.14).

The three-dimensional motions of the reacting atoms (for the A,H dimer) was analysed by plotting the coordinates, sampled every 1 ps, over the minimised AADH:tryptiminoquinone structure (Figure 3.15). The motions of C1/H1 correspond to a rotation of this group very similar to that required to achieve tunneling in the VTST/MT calculations (Masgrau et al. 2006). In other words the motions of C1/H1 are very similar in nature to those required to go from the reactant to the RTE

85

structure (the representative structure for tunneling) for proton tunneling to O2. At the same time, this C1/H1 rotation would not aid proton transfer to O1, suggesting that O2 is the favoured proton acceptor dynamically as well as thermodynamically and kinetically (Masgrau et al. 2006). Note that the motion of the indole in Figure 3.15b, where PC1 for this motion is most clearly visible, corresponds to the motion required to reduce the indole-quinone angle. However, as shall be discussed in the next section, the motion of the indole is not coupled to the motion of C1/H1, so that this indole motion does not, in fact, drive the aforementioned C1/H1 rotation.
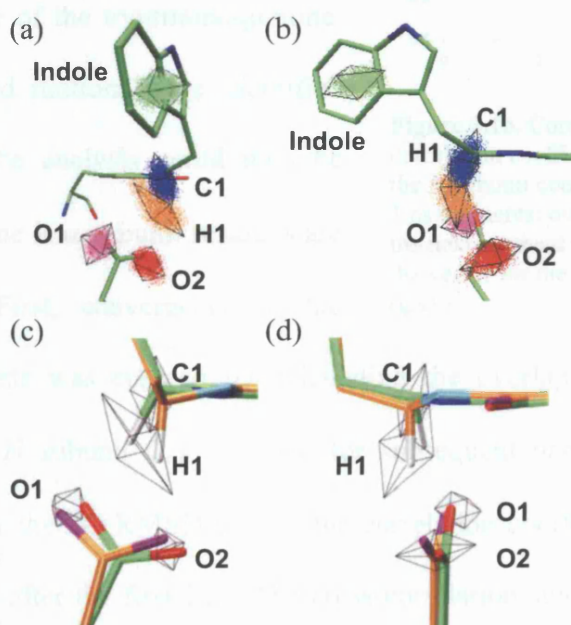
Figure 3.15. Comparing motions from the MM MD simulation to the motions from the VTST/MT calculations: (a,b) orthogonal views illustrating the motions of C1, H1, O1, O2 and the indole heavy-atom centroid in the *A,H* active site, superimposed over the energy minimized structure; the coloured dots represent the coordinates sampled at 1 ps intervals and the cages represent the principal components of the motions; (c,d) orthogonal views of the motions of C1, H1, O1 and O2 superimposed on the R (green carbon atoms) and RTE structures from the VTST/MT calculations.

3.5.1. Cross-Correlation Analysis

In view of the stronger structural convergence for the *A,H* dimer, the cross-correlation analysis is presented only for this dimer. Of particular interest is the correlation within the β subunit, since this encompasses the reacting iminoquinone and aspartate. If there are correlated motions involving the α subunit that affects the active site then these will propagate either through residues in the β subunit or the indole of the tryptiminoquinone. If strongly correlated motions were identified for this selection, the analysis could then be expanded to determine if α subunit residues are involved as well. First, convergence of the
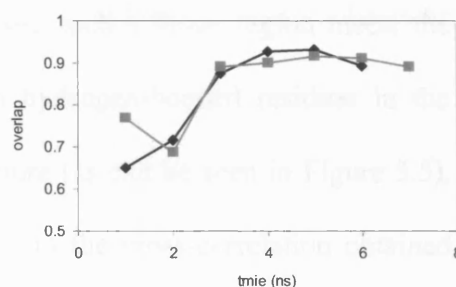
Figure 3.16. Convergence of the C_α correlation coefficients: vector overlaps for the *H* subunit coefficients for consecutive 1 ns segments: overlap with the vector for the next segment (black) and overlap with the vector for the correlations of the last 5 ns (grey).

correlation coefficients was ensured by calculating the overlap for the vector of coefficients for the *H* subunit C_αs obtained for subsequent nanosecond segments (Figure 3.16). As for the 2D RMSD values, the correlation coefficients for the *A,H* dimer are converged after the first 2 ns. The cross-correlation analysis will therefore employ the 2-7 ns time period. The dynamical cross-correlation map (DCCM) for the β subunit C_αs and heavy atom centroids, as well as the α subunit residues closest to the indole – F97α, F123α, N124α and L179α – are shown in Figure 3.17. The correlation coefficients were calculated following structural alignment to the C_αs of the β subunit, rather than the entire enzyme or the *A,H* dimer, so that the relative motions within the subunit become maximised.

Cross-correlation coefficients range from -1 to +1, and using a low cut-off of ±3 similar to that used in the analysis of DHFR by Radkiewicz and Brooks (Radkiewicz and Brooks 2000) there are no regions of strong correlation within the β subunit. The only regions of significant positive correlation (0.3 – 0.6) correspond to adjacent hydrogen-bonded strands within the β sheet – the mainly linear yellow regions in the DCCM which are nearly perpendicular to the diagonal. For example, the region near the middle of the C_α DCCM where such a linear region meets the diagonal corresponds to the correlation between hydrogen-bonded residues in the strands before and after the β hairpin in the structure (as can be seen in Figure 3.5). Comparing the aforementioned analysis of DHFR to the cross-correlation obtained here suggests that long-range motions are likely to be less significant in AADH than in DHFR: a long-range network of promoting motions was diagnosed in DHFR (see Section 1.5.3), which coincides with the regions of strong positive and negative correlation (Agarwal *et al.* 2002b).
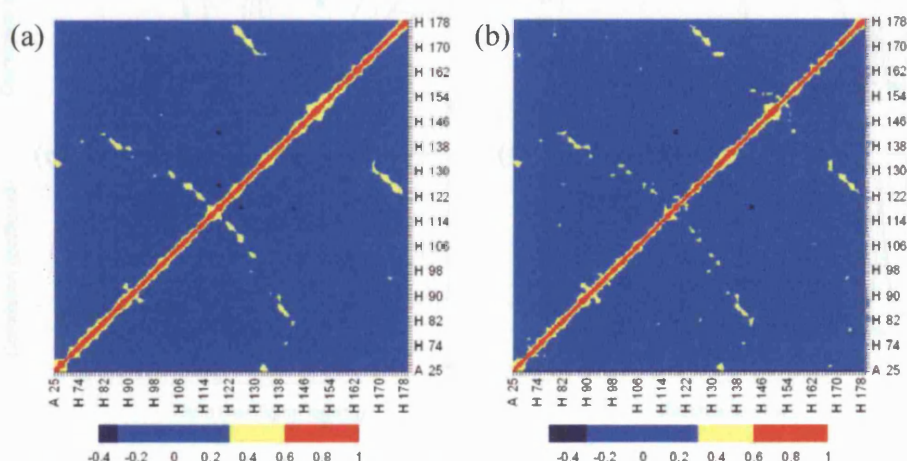
Figure 3.17. Dynamical cross-correlation maps (DCCMs) for the last 5 ns of the MM MD simulation: (a) C_α and (b) heavy atom centroid DCCMs for the β subunit (residues labeled H) and the four α residues (A) closest to the indole. The correlations range from significantly negative (< -0.3, dark blue), insignificant (-0.3 – +0.3, blue), significantly positive (> +0.3, yellow), to strongly positive (> +6, red).

The probability of tunneling is strongly dependent on the relative positions of and distance between the donor, acceptor and transferring proton. Therefore, a promoting network of correlated motions would be expected to drive the motions of these atoms, and ideally push C1/H1 towards O2. To determine whether such a network exists, the cross-correlation coefficients for C1, H1, O1 and O2 were calculated, with the motions of the indole and quinone heavy atom centroids treated separately (Figure 3.18). For simplicity, the four α subunit residues employed previously (see Figure 3.10) are ignored, since they are not in direct contact with the atoms under scrutiny, and if they were involved in a correlated motion with any of
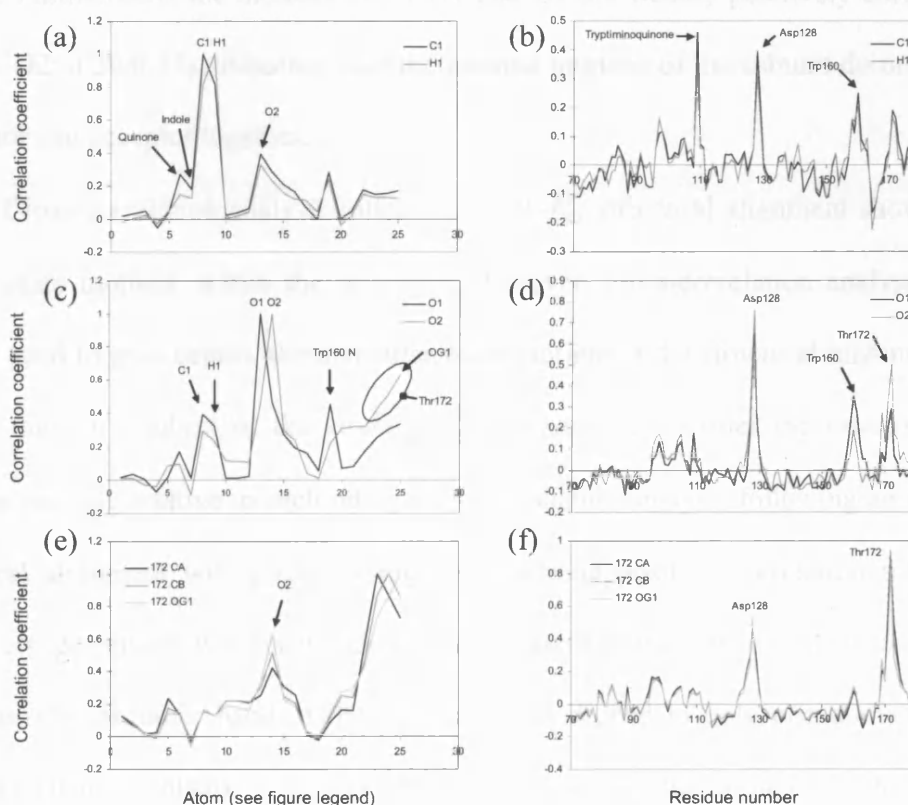
Figure 3.18. Cross-correlation coefficients for specific active site atoms: (a,b) iminoquinone C1/H1; (b,c) Asp128β O1/O2; (c,d) Thr172β. The coefficients for (a,c,e) are for atoms and groups of atoms around the active site and those for (b,d,f) are for β subunit residue heavy atom centroids. Atoms and groups around the active site used for (a,c,e): 83β CB; 2. 83β CG1; 3. 85β CA; 4. 88β N; 5. 88β SG; 6. 109β quinone; 7. 109β indole; 8. 109β C1; 9. 109β H1; 10. 126β CB; 11. 126β CG; 12. 126β CD2; 13. 128β O1; 14. 128β O2; 15. 129β CA; 16. 129βCB; 17. 159β OD1; 18. 159β ND2; 19. 160β N; 20. 169β CZ; 21. 169βCE1; 22. 171β CA; 23. 172β CA; 24. 172βCB; 25. 172β OG1O1Thr172β (atom names are given using the standard RCSB Protein Data Bank format)

these atoms then the correlation would be propagated either through β subunit residues or the indole. The motions of O1 and O2 are, unsurprisingly, significantly correlated with each other (coefficient 0.46), and are correlated with their hydrogen-bonding partner atoms (O1-Trp90β N: 0.45, O2-Thr172β $O_{\gamma1}$: 0.64) and residue centroids (O1-Trp90β: 0.19, O2-Thr172β: 0.50). O1 and O2 are not, however, significantly correlated with any other surrounding atoms or residues within the subunit. Thr172β is only strongly correlated with O2, so there is no network of correlated motion pushing O2. Therefore, in terms of pushing the donor (C1/H1) and acceptor atoms (O2) there does not appear to be any network of correlated promoting motion. Furthermore, the motions of C1/H1 and O2 are weakly positively correlated (C1/H1-O2: 0.29/0.23), indicating that the internal motions of the subunit do not push the donor and acceptor together.

Cross-correlation analysis following an all-C_α structural alignment shows the largest-scale motions within the selection. However, cross-correlation analysis can also be used to give details about smaller scale motions if the structural alignment is carried out on a subset of the structures. For example, consider the case of two domains moving relative to each other: cross-correlation analysis following an all-C_α structural alignment will give two regions of strong positive correlation that are negatively correlated with each other, and this will mask any motion *within* the domains. On the other hand, if the structures are aligned to only one domain, the cross-correlation analysis will reveal the motions within this domain. In this way, cross-correlation analysis can be used to zoom in on groups of particular interest. In the case of the AADH reaction, the groups of major interest are Asp128β and the iminoquinone. If a network of correlated motions were to contribute to a donor-acceptor compression, then it would likely correspond to a relative motion of

Asp128β and the iminoquinone. It therefore makes sense to measure the cross-correlations that correspond to this relative motion, by first aligning the structures from the MD simulation to the iminoquinone and Asp128β heavy atoms, so that the small scale motions within this selection are revealed (note that information on the internal motions within regions outside this selection is lost). Due to this structural alignment, the iminoquinone and Asp128β centroids are perfectly negatively correlated (Figure 3.19a,b); however, they are not strongly correlated with any other residues in the subunit. C1/H1 and O2 are positively correlated with each other (Figure 3.19c,d), and C1/H1 are only weakly anti-correlated with the indole and quinone centres of mass, while O2 is strongly positively correlated with the Asp128β centroid (0.67). It therefore appears that the linker region connecting the indole and quinone is inherently flexible, so that C1/H1 moves independently of either the indole or the quinone. This result is further supported by principal components analysis
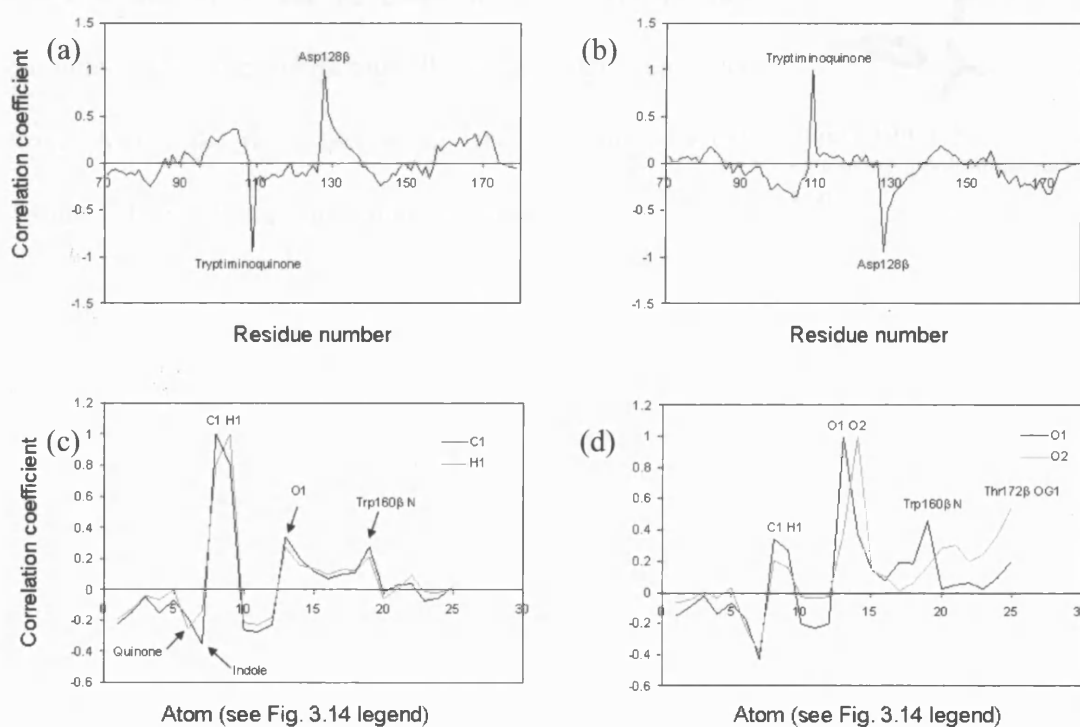
Figure 3.19. Correlation coefficients for the reacting groups and atoms following structural alignment to the iminoquinone and Asp128β heavy atoms: (a) Asp128β and (b) iminoquinone heavy atom centroids, (c) iminoquinone C1/H1, (b) Asp128β O1/O2. The atom selection for (c,d) is the same as in Fig,. 3.14.

(PCA) of the covariance matrix for C1, H1, O1, O2 and the Asp128β, indole and quinone heavy atom centroids. The covariances for each of these seven atoms/centroids produce seven seven-dimensional vectors, and comparison with the principal component vectors revealed that PC1 corresponds entirely to the covariance vector of C1 and H1 (PC1-C1/H1 overlap = 0.99 and 0.98, respectively) but not to the vectors of the other atoms/ centroids. For example, the overlap between PC1 and the covariance vector for the indole and quinone was -0.18 and 0.19 respectively. This reinforces the view that the indole-quinone angle does not directly modulate the C1/H1-O2 distance (Sections 3.5.1 and. 3.6).

In view of the fact that C1/H1 move independently of the indole and quinone, the relation between the indole-quinone angle (Figure 3.11e,f) can be explained thus: at low angles, the the flexibility of the linker region allows the H1-O2 distance to fluctuate between its minimum value of ~2 Å and ~3 Å; on the other hand, at large indole-quinone angles, the indole pulls the linker region up away from Asp128β, thus increasing the average H1-O2 distance. This effect is illustrated in Figure 3.20.
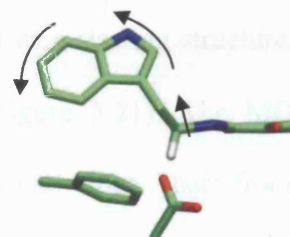
Figure 3.20. Effect of increasing indole-quinone angle

3.6. MD Simulation of the Solvated AADH β Monomer

Kinetic experiments have been carried out on the isolated β monomer in solution[1], which revealed that the monomer is catalytically active, but with the rate of the tunneling step three orders of magnitude lower than that in the $\alpha_2\beta_2$ heterotetramer (obtaining a precise rate that is comparable to that of the heterotetramer is not possible due to the pseudo-second order nature of the reaction). For the reaction with tryptamine, the KIE is 2.7 at 298 K, which indicates a much lower degree of tunneling. To gain insight into possible reasons for this, QM/MM MD simulation and potential energy calculations are carried out in Chapter 5. Unfortunately, no crystal structure of the isolated monomer is available. Therefore, an MM MD simulation was run, using the β monomer from the minimised heterotetramer as a starting structure, solvated in a 25 Å water sphere and minimised again (Figure 3.21). The MD simulation was run using the same protocol as for the heterotetramer, apart from employing a constant rather than a distance-dependent dielectric.
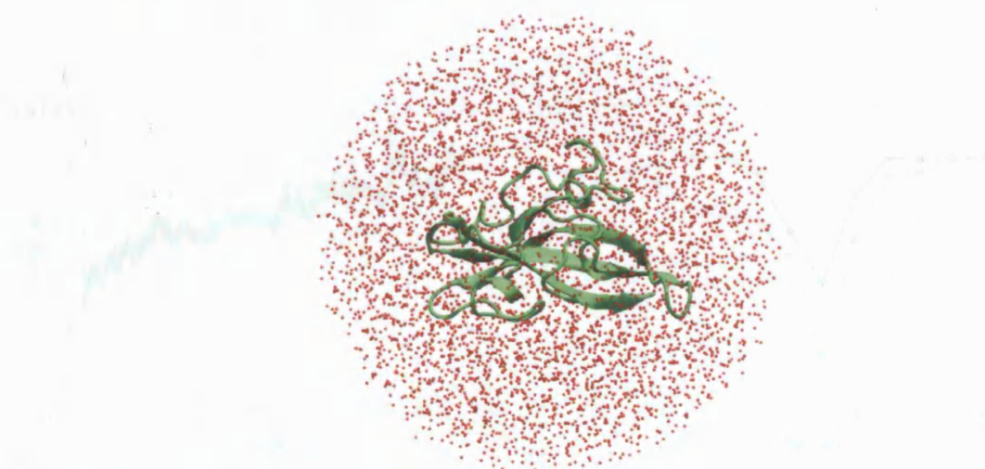
Figure 3.21. Structure of β monomer, solvated and energy minimised.

---

[1] Personal communication with Nigel S. Scrutton and Parvinder Hothi; work in progress.

The C_α RMS deviation for this MD simulation is shown in Figure 3.22a, which suggests that the system has not reached equilibration. However, comparing PC1 for sequential 0.5 ns segments of the C_α 2D RMSD matrix for structures sampled every 2 ps suggests that the structure has in fact converged for the last 2 ns (the last four points in the plots in Figure 3.22b), after a conformational change at ~3-4 ns (Figure 3.22b). This seems at variance with the RMS deviation, but can be understood from a 2D surface plot for the 2D RMS matrix for structures sampled every 25 ps (Figure 3.23) – the larger time between sampling is so that the matrix is small enough to plot. Squares of similar colour in a 2D RMSD surface plot represent clusters with consistent structural fluctuations (this is the principle employed by clustering algorithms), and here two such regions can be observed, indicated by the dotted boxes, which correspond to the time periods before and after the aforementioned conformational change at ~3.5 ns. Therefore, the system does indeed appear to have reached structural convergence. The structure that is used for the analyses in Chapter 5 is one after 5 ns of MD simulation, which lies inside the region of structural convergence after the conformational change in Figure 3.22b and Figure 3.23.
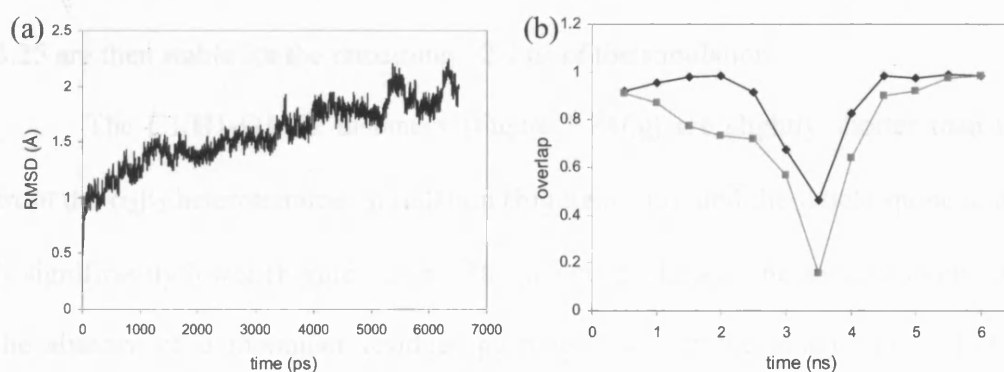
Figure 3.22. (a) C_α RMS deviation for MM MD simulation of the β monomer; (b) vector overlap for consecutive 0.5 ns segments from the C_α 2D RMSD matrix with the next segment (black) and the final segment (grey).

The previously mentioned conformational change is accompanied by structural changes in the active site (Figure 3.24). There is a change in the conformation of Phe169β at ~3.5 ns, which corresponds to a rotation of the Phe169β side chain away from Asp128β (Figure 3.24b). This conformational change does not occur in the heterotetramer, because the neighbouring α subunit residues prevent it (see Figure
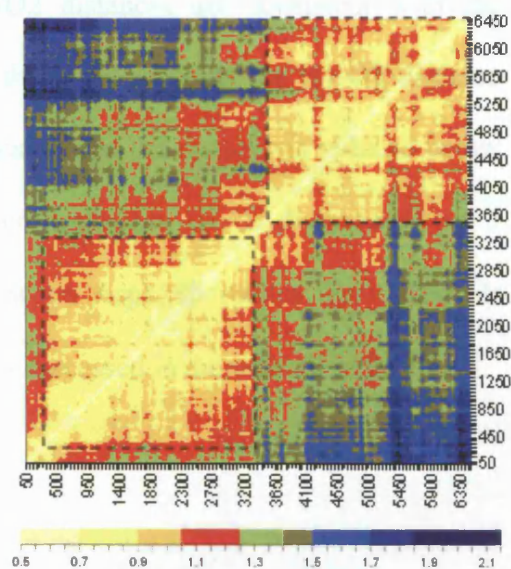
Figure 3.23. 2D RMSD matrix for MM MD simulation of the β monomer; the axes are time (ps). Squares of similar colour, which represent clusters with internally consistent structural fluctuations, are outlined.

3.10f). As Phe169β changes conformation, this allows a temporary breakage of the hydrogen bond between O2 and Thr172β, coupled with a rotation of the Asp128β and Thr172β side chains (Figure 3.24c,d). The large rotation of Asp128β at ~4.2 ns causes a sharp increase in the H1-O2 distance (Figure 3.25b). However, after ~4.3 ns, the hydrogen-bond between O2 and Thr172β reforms and both Asp128β and Thr172β return to their initial conformations. The structural measurements in Figs. 3.24 and 3.25 are then stable for the remaining ~2.2 ns of the simulation.

The C1/H1-O1/O2 distances (Figure 3.24f,g) are slightly shorter than those from the $\alpha_2\beta_2$ heterotetramer simulation (Figure 3.11a), and the indole-quinone angle is significantly lower (Figure 3.24h). This lower indole-quinone angle is likely due to the absence of α monomer residues pushing down on the indole. The C1/H1-O1 distances show similar fluctuations to their $\alpha_2\beta_2$ heterotetramer counterparts (Figure 3.11), while the C1/H1-O2 distances and the indole-quinone angle show less pronounced fluctuations than the heterotetramer values. The lower fluctuations in

both the indole-quinone angle and C1/H1-O2 distances are consistent with the previous view (Section 3.4.1) that reducing the angle prevents the H1-O2 distance from being greater than ~3 Å, but does not ensure that the distance is reduced below ~3 Å. The few points in Figure 3.11d which correspond to H1-O2 distances above 3 Å occur during the conformational change when Asp128β rotates away from its normal position. This conformational change is discussed in more detail in Section 5.
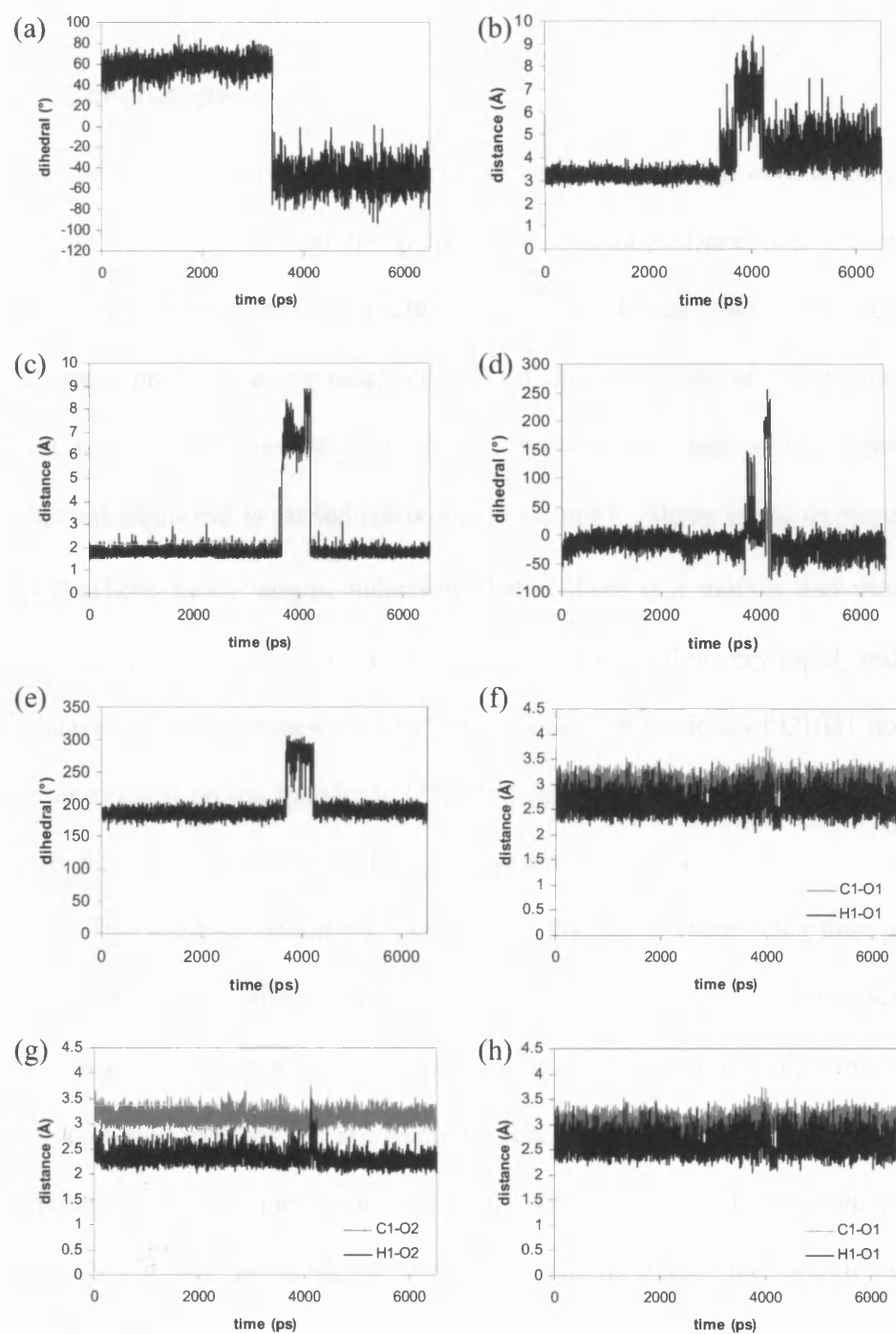
Figure 3.24. Conformational change during MM MD simulation of β monomer: (a) dihedral angle for rotation about Phe169β C_α-C_β bond; (b) O2-Phe169β distance; (c) O2-Thr102β $H_{\gamma 1}$ distance; (d) dihedral angle for rotation about Asp128β C_β-C_γ bond; (e) dihedral angle for rotation about Thr102β C_α-C_β bond; (f) C1/H1-O1 distances; (g) C1/H1-O2 distances; indole-quinone angle *vs* H1-O2 distance.

3.7. Conclusions

Cross-correlation analysis revealed no regions of significant correlation around the active site, and suggests that the inherent flexibility of the linker region connecting the indole and quinone of the reacting tryptiminoquinone allows the donor C1/H1 methylene group to move independently of the rest of the tryptiminoquinone. The motions of C1/H1 are not anticorrelated with the motions of O2, whether initial structural alignment is carried out on the β subunit C_α atoms or the tryptiminoquinone and Asp128β heavy atoms, indicating that if there is a motion that modulates the donor-acceptor distance it is very small scale, and therefore very rapid, and not suited to diagnosis via long-timescale MD simulations. The motions of C1/H1 do, however, appear to assist proton transfer to O2 rather than O1, by rotating C1/H1 towards their position in the structure for the RTE (Masgrau et al. 2006).

This analysis cannot rule out motions that have effects other than pushing the donor and acceptor groups – for example electrostatic effects – but the fact that there are no regions of strong correlation within the active-site containing subunit indicates that correlated motions are not likely to play a significant role. Furthermore, cross-correlation analysis only applies to the *overall* motions of the atoms or residue centroids that are included, not specific vibrations within the overall motion (see Chapter 4).

The MD simulation of the β monomer suggests less motion within the tryptiminoquinone - the C1/H1-O2 distances and the indole-quinone fluctuations are less pronounced than they are in the $\alpha_2\beta_2$ heterotetramer. However, lower C1/H1-O1/O2 distances are achieved in the β monomer, which appears to be at variance with

the experimentally observed ~1000 fold reduction in proton transfer rate in the β

monomer relative to the heterotetramer.

4.   Short Timescale Molecular Dynamics Simulations and Frequency Calculations

4.1. Preface

It has been shown that achieving a tunneling configuration requires structural rearrangements of the reacting moieties, namely a rotation of the donor carbon (C1) and transferring proton (H1) and a reorientation of the acceptor oxygen (O2), to achieve a sufficiently short hydrogen-oxygen separation (Masgrau et al. 2006). To fully understand the mechanism of vibrationally assisted tunneling for this proton transfer, it is necessary to understand how these motions emerge, i.e. how they relate to the overall motions of C1, H1 and O2, and also to the motions of surrounding atoms. Long timescale MM MD simulations suggest that the motion of the C1/H1 methylene group is independent of surrounding atoms. To study this motion in detail, and how it relates to the motion of O2 and other atoms, short timescale MM MD simulations were run, so that sub-picosecond motions can be recorded. This allows the analysis of specific atomic vibrations, and how these can promote tunneling by pushing the system towards a tunneling configuration, in particular by reducing the H1-O2 distance.

4.2. Analysis of MM MD Simulations

To understand how enzyme motion might promote proton transfer it is first necessary to examine how the motion of the hydrogen and oxygen relate to the hydrogen-oxygen distance. To this end, a 400 ps MM MD simulation was run using a 1 fs timestep, which was started from a structure and corresponding velocities after 2 ns of long time-scale MD simulation (Section 3.5). Coordinates were sampled at 8 fs intervals. This time interval allows the study of very fast motions, such as the vibration of individual atoms, and 400 ps provides adequate sampling of sub-

picosecond motions. Atomic velocities were computed as the change in distance over each 8 fs interval; these are not instantaneous velocities, but for the purposes of this analysis this does not matter, since only very small-scale motions happen at that timescale. The discussions will focus on the A,H dimer, since the MD simulations for this dimer were found to be better than those for the B,D dimer (Section 3.5).

From these atomic velocities, it is then possible to compute spectral densities (Section 2.7.3), to determine the relative population of the various frequencies involved in a particular motion. Spectral density analysis has been used previously by Schwartz and co-workers to diagnose promoting vibrations in enzymes (Caratzoulas and Schwartz 2001; Caratzoulas et al. 2002). Using the frequencies identified from spectral densities, it is possible to visualise the corresponding motions using digital filtering by frequency deconvolution (Sessions et al. 1989).

4.2.1. Velocity Analysis

It is possible to get an indication of how much the motions of H1, O1 and O2 contribute to the H1-O1/O2 distances by simply comparing the magnitudes of the atomic velocities, i.e. the speeds, with the changes in distance. Therefore, as well as the atomic velocities, the changes in H1-O1/O2 distances were also measured at 8fs intervals. Comparing these to the velocities of H1, O1 and O2, suggests that the H1 velocity contributes most to the change in the distances: the average and spread of O1/O2 velocities are much lower than the H1 velocities or the changes in H1-O1/O2 distances (Table 4.1). The contribution of the motion of each atom to the H1-O1/O2 distances was further estimated by calculating the change in distance of one of the H1-O1/O2 pair to the average position of the other (Table 4.1). The average and standard deviations for the changes in H1-⟨O1/O2⟩ distances (angle brackets denote

(a)	$|\Delta[d(H1\text{-}O1)]|$	$|\Delta[d(H1\text{-}O2)]|$	$|v(H1)|$	$|v(O1)|$	$|v(O2)|$
μ (Å/fs)	0.0759	0.0783	0.1463	0.0495	0.0496
σ (Å/fs)	0.0590	0.0600	0.0713	0.0209	0.0209

(b)	$|\Delta[d(H1\text{-}\langle O1\rangle)]|$	$|\Delta[d(\langle H1\rangle\text{-}O1)]|$	$|\Delta[d(H1\text{-}\langle O2\rangle)]|$	$|\Delta[d(\langle H1\rangle\text{-}O2)]|$
μ (Å/fs)	0.0716	0.0252	0.0748	0.0252
σ (Å/fs)	0.0566	0.0190	0.0573	0.0190

Table 4.1. Analysis of H1 and O1/O2 velocities. Average, μ, and standard deviation, σ (in Å/fs) for (a) for the magnitude of the change in H1-O1/O2 distance ($|\Delta[d(H1\text{-}O1/O2)]|$) compared to the speed of H1, O1, O2 ($|v(H1/O1/O2)|$), and (b) the magnitude of the change in H1-⟨O1/O2⟩ and ⟨H1⟩-O1/O2 distances ($|\Delta[d(H1\text{-}\langle O1/O2\rangle)]|$ and $|\Delta[d(\langle H1\rangle\text{-}O1/O2)]|$), where the angle brackets denote an ensemble average.
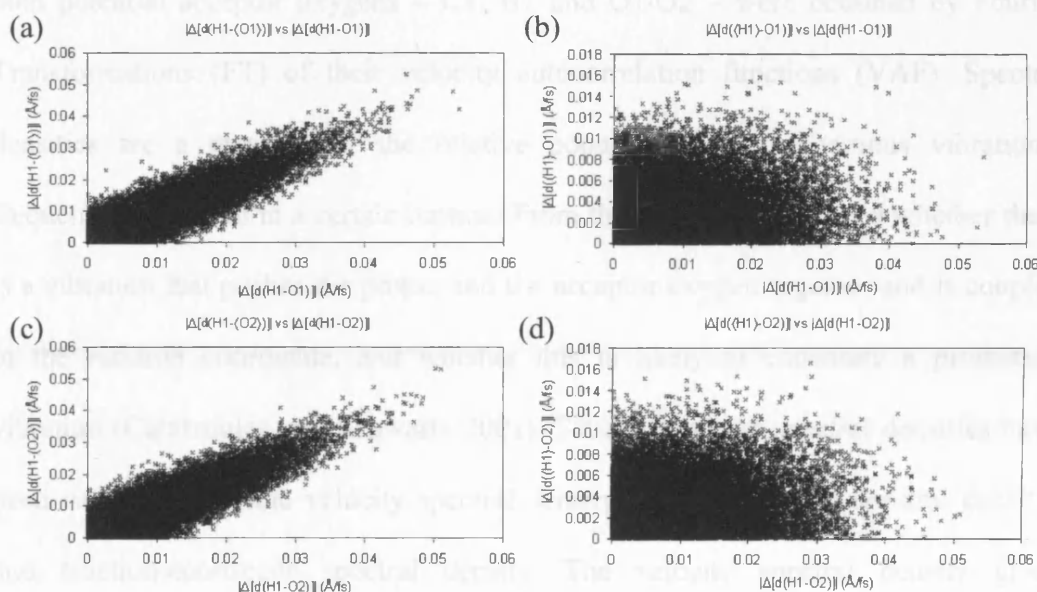
Figure 4.1. Contibution of H1, O1 and O2 motions to the H1-O1/O2 distances. The speed of change of distance between one atom and the average position of the other atom are plotted against the speed of change of distance between the two atoms.

an ensemble average) are very similar to the values for H1-O1/O2, while the values for ⟨H1⟩-O1/O2 are about one third of those for H1-O1/O2. Furthermore there is a good correlation between the changes in H1-⟨O1/O2⟩ distances and the change in H1-O1/O2 distance, while there is no correlation for ⟨H1⟩-O1/O2 (Figure 4.1). (Interestingly, there is no such good correlation between the speed of H1 and the change in H1-O1/O2 distance.) Therefore, although this is a fairly crude analysis, it does reveal that the motion of H1 is the most important factor for the H1-O1/O2

distances. This analysis does not, however, reveal if the motion of H1 favours one of the two oxygen atoms, and therefore whether proton transfer to either of the two potential acceptor atoms is favoured dynamically.

4.2.2. Spectral Density Analysis

The spectral densities of the motions of the atoms involved in the reaction, including both potential acceptor oxygens – C1, H1 and O1/O2 – were obtained by Fourier Transformations (FT) of their velocity autocorrelation functions (VAF). Spectral densities are a measure of the relative populations of the various vibrational frequencies involved in a certain motion. From these it can be deduced whether there is a vibration that pushes the proton and the acceptor oxygen together and is coupled to the reaction coordinate, and whether this is likely to constitute a promoting vibration (Caratzoulas and Schwartz 2001). Several types of spectral densities have been calculated: atomic velocity spectral density, relative-velocity spectral density, and reaction-coordinate spectral density. The velocity spectral density gives information on the relative populations of the frequencies involved in the 3-dimensional motion of an atom, and the VAF is obtained from the dot-products of the velocities at different time intervals. For the relative velocity spectral density for two atoms A and B, the relative velocity of the two atoms involved is calculated and projected onto their inter-atomic axis according to the equation:

$$r_{AB} = v_{AB} \cdot u_{AB} \qquad (4.1)$$

where v_{AB} is the relative velocity of atoms A and B, and u_{AB} is the unit vector along the A-B axis. Since r_{AB} is a scalar value, the VAF is obtained by scalar multiplication. The reaction coordinate spectral density uses a reaction coordinate s which is simply a linear combination of the coordinates of the donor atom, transferring proton and acceptor atom:

$$s = \left[r_H - \frac{(m_D r_D + m_A r_A)}{m_D + m_A} \right] \cdot u_{DA} \tag{4.2}$$

where $r_{H/D/A}$ is the coordinate vector for the proton/donor/acceptor, and $m_{D/A}$ is the mass of the donor/acceptor, so that s depends simply on the position of the proton relative to the donor and acceptor atoms. It is important to realise that this is much simpler than the true reaction coordinate; however, s will be a strong component of the true reaction coordinate. Before calculating the VAF, the change in s from one frame in the MD to the next is computed: just as velocity is a change in coordinate, so too is the change in reaction coordinate required. Note that s, just as r_{AB}, is a scalar value.

The calculations of spectral densities are explained in more detail in Section 2.7.3. The spectral densities are smoothed using the Savitzky-Golay algorithm, so while the resulting spectral densities show the relative population of the frequencies, they cannot distinguish between vibrations of very similar frequencies. This does not matter for the purposes of this analysis, since it only aims at identifying the most strongly populated frequencies: any system is likely to have vibrations that are coupled to some extent to the reaction coordinate, but the vibrational energy of the atoms involved is efficiently channelled into the vibration only if it is strongly

populated. However, it is important to realise that changes in the relative populations of vibrations of very similar frequency can affect the precise location of the top of the corresponding peak in the smoothed spectral density.

The spectral densities were calculated for the 400 ps molecular dynamics window mentioned previously. The spectral densities for the 3-dimensional motions of the reactive atoms (C1, H1, O1/O2) reveal that these motions can be broken down into a few major frequencies. The motions of interest here are those that can most significantly modulate the donor-acceptor and proton-acceptor distances, which are in the low-frequency region of the spectrum. Of primary interest, therefore, are the peaks below $ca.$ 500 cm^{-1}. One of the motions of particular interest, as identified from VTST/MT calculations (Masgrau et al. 2006), is a rotation of the donor methylene group, which would correspond to a peak that is common to both C1 and H1. C1 and H1 velocity spectral densities (Figure 4.2a,b) share the strongest low-frequency peak at about 165 cm^{-1}, which therefore corresponds to a vibration of the methylene group; although this peak is quite wide for H1, the highest point is at ~165 cm^{-1}. For O1 and O2 the strongest low-frequency peaks are at about 145 cm^{-1} and 120 cm^{-1} respectively (Figure 4.2c). C1 also has a strong peak at about 380 cm^{-1}, while H1 has a relatively small peak at the same frequency, and C1 and H1 have overlapping peaks at about 880 cm^{-1} and O2 has a weaker peak at about 270 cm^{-1}. The spectral densities for the C1-O2 and H1-O2 relative motions (Figure 4.2d,e) both have a prominent peak at about 100 cm^{-1}, making this frequency a potential candidate for a promoting vibration. The C1-O2 and H1-O2 spectral densities also have strong peaks at about 260 and 880 cm^{-1} respectively. The strongest low-frequency peak in the H1-O1 spectral density, at about 250 cm^{-1} does not correspond to the strongest peak in the C1-O1 spectral density, which lies at about 325 cm^{-1}, and these peaks are weaker than those

in the H1-O2 and C1-O2 spectral densities, indicating that the proton moves more effectively towards O2 than O1.

Comparing the O2 and C1/H1-O2 spectral densities suggests that the 100 cm^{-1} squeezing along the C1/H1-O2 axes corresponds to motion of O2, since, although the centre of the major peak in the O2 spectral density is at ~120cm^{-1}, this is quite a wide peak about 2.5 times higher than the H1-O2 peak, which can easily accommodate the
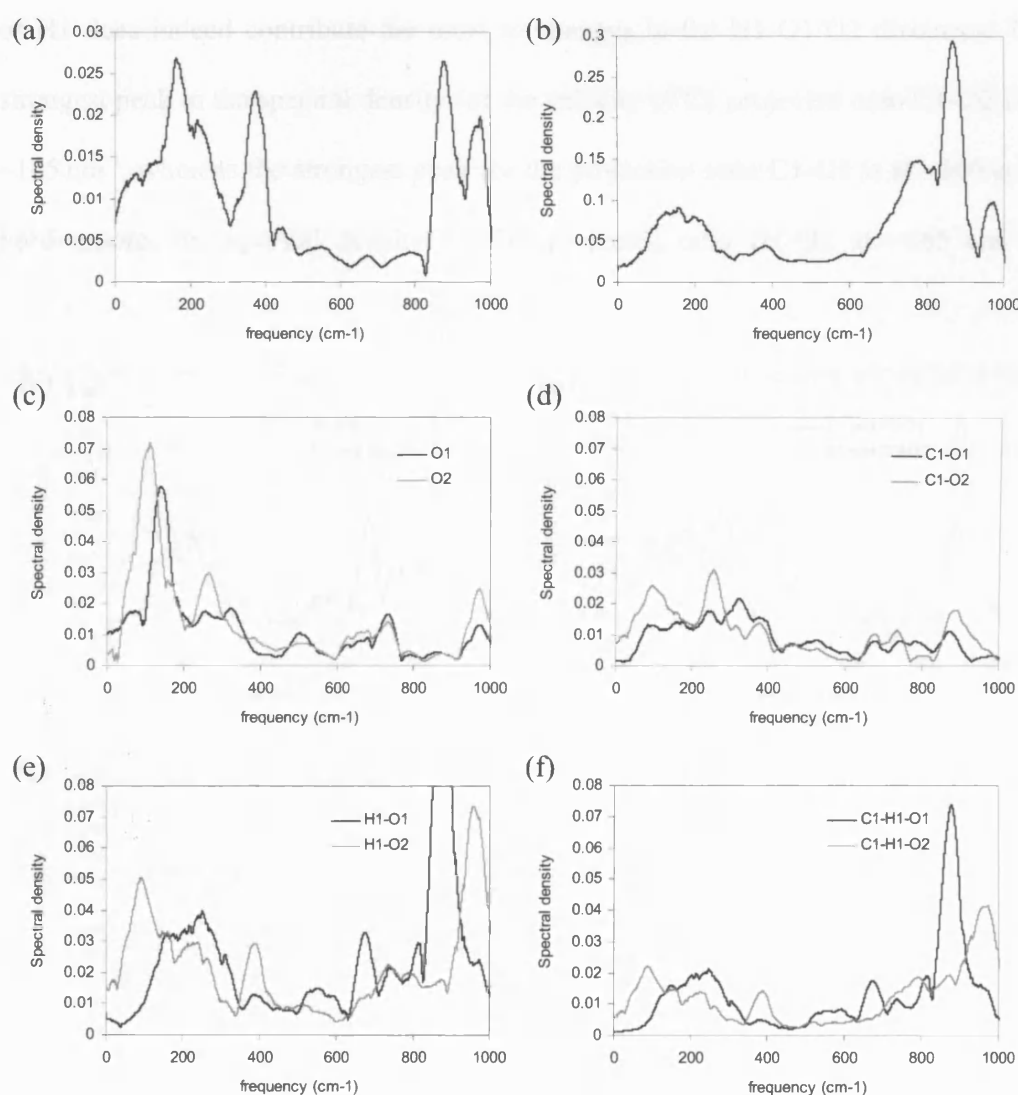
Figure 4.2. Spectral densities for C1, H1, O1 and O2: velocity spectral densities for (a) C1, (b) H1, (c) O1/O2, relative velocity spectral densities for (d) C1-O1/O2 and (e) H1-O1/O2, and (f) the C1-H1-O1/O2 reaction coordinate spectral densities.

100 cm^{-1} H1-O2 peak. However, the velocity comparison in Section 4.2.1 indicated that the motion of H1 contributes the most to the modulation of the H1-O1/O2 distance. Therefore, to determine precisely which atom contributes the most to the changes in the H1-O1/O2 distance, and also to further examine whether H1 moves more towards either O1 or O2, the spectral densities for the H1 and O1/O2 velocities projected onto the H1-O1/O2 axes were calculated (Figure 4.3). The spectral densities for H1 are stronger than those for O1 or O2 in both cases, indicating that the motion of H1 does indeed contribute the most to changes in the H1-O1/O2 distances. The strongest peak in the spectral density for the velocity of C1 projected onto C1-O2 is at ~165 cm^{-1}, whereas the strongest peak for the projection onto C1-O1 is at ~380 cm^{-1}. Furthermore, the spectral density for H1 projected onto H1-O2 at ~165 cm^{-1} is
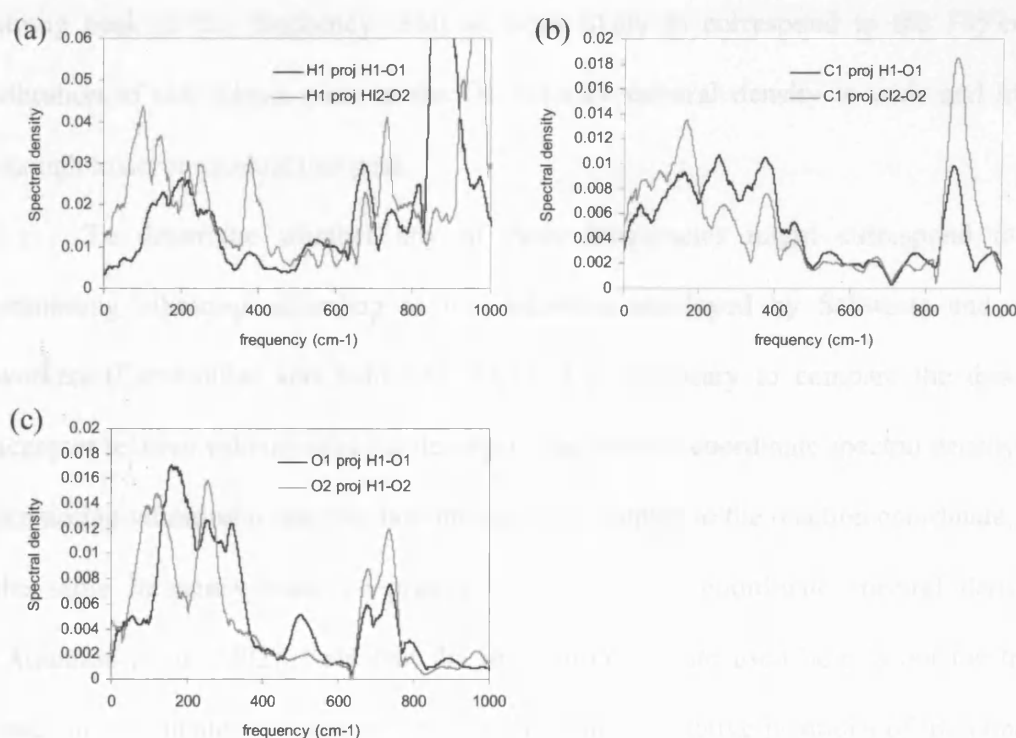
Figure 4.3. Spectral densities $J(\omega)$ for velocities projected onto the C1/H1-O1/O2 vectors: (a) H1, (b) C1 and (c) O1/O2.

stronger than that for the velocity projected onto H1-O1. Therefore, the 165 cm^{-1} vibration of the methylene group pushes C1 and H1 towards O2 more than O1.

The spectral density for H1 projected onto H1-O2 is stronger at both ~100 and ~250 cm^{-1} than for the projection onto H1-O1, even though modulation of the H1-O1 distance is stronger at ~250 cm^{-1}. This is because the ~250 cm^{-1} peak does not correspond to the highest peak in either the H1 or O1 projected velocity spectral densities (these are at ~210 and ~165 cm^{-1} respectively), since the relative velocity spectral density is equal to the sum of the projected velocity spectral densities for the two atoms in question, and it is this sum that is strongest at ~250 cm^{-1}. Note that although the spectral density for the projected velocity of O1 has a strong peak at ~165 cm^{-1}, this does not necessarily indicate that O1 is strongly coupled to the 165 cm^{-1} vibration of C1/H1, since the velocity spectral density of O1 does not show a strong peak at this frequency. This is more likely to correspond to the 145 cm^{-1} vibration of O1, whose peak in the O1 velocity spectral density is wide and high enough to accommodate this peak.

To determine whether any of these frequencies might correspond to a promoting vibration according to the definition employed by Schwartz and co-workers (Caratzoulas and Schwartz 2001), it is necessary to compare the donor-acceptor relative velocity spectral density to the reaction coordinate spectral density: a promoting vibration is one that is symmetrically coupled to the reaction coordinate, so the same frequency must be present in the reaction coordinate spectral density (Antoniou et al. 2002). Note that the reaction coordinate used here is not the true reaction coordinate, but one derived simply from the relative positions of the donor, acceptor and transferring proton projected onto the donor-acceptor axis. The 100 cm^{-1} vibration identified in the C1/H1-O2 spectral densities is present in the C1-H1-O2

reaction coordinate spectral density (Figure 4.2f), while the strongest low-frequency (i.e. below 500 cm^{-1}) peak in the C1-H1-O1 spectral density corresponds to the second-strongest 250 cm^{-1} peak in the C1/H1-O1 spectral densities. There is therefore a stronger correspondence between the relative velocity and reaction coordinate spectral densities for O2 than O1, indicating that a promoting vibration for proton transfer to O2 is more probable than one for transfer to O1.

Comparing the single-atom spectral densities with donor-acceptor and reaction coordinate spectral densities reveals that the 875 cm^{-1} vibration corresponds to C1/H1 motion, while the 960 cm^{-1} vibration corresponds to motion of O1. There is therefore a high frequency vibration, caused by C1/H1 motion that also contributes to a reduction of the C1-H1-O2 reaction coordinate, while an even higher frequency vibration, caused by O1 motion, contributes to a reduction of the C1-H1-O1 reaction coordinate. However, vibrations at such high frequencies correspond to motions of much smaller magnitude, which will not squeeze the reaction coordinate as much, and would therefore constitute a less effective promoting vibration. It has also been argued that vibrations of such high frequency are likely to promote the reaction less effectively because the timescale when the barrier remains low is too short (Antoniou *et al.* 2004).

The best candidate for a promoting vibration therefore appears to be the 100 cm^{-1} C1/H1 vibration, which pushes C1/H1 and O2 towards each other and squeezes the corresponding reaction coordinate. However, this vibration does not correspond to a major vibration of any of the three atoms involved – the 120 cm^{-1} peak from the O2 spectral density does overlap with this frequency, but the 100 cm^{-1} is much weaker, indicating that the O2 vibration at this frequency is only weakly coupled to the 100 cm^{-1} C1/H1-O2 vibration. The major vibration of the C1/H1

methylene group at ~165 cm^{-1} pushes both C1 and H1 towards O2 more than O1. The conclusions from this spectral density analysis are, therefore, that the dynamics of the system seem to prefer transfer to O2, in agreement with VTST/MT calculations (Masgrau et al. 2006), with a potential promoting vibration at 100 cm^{-1}, and that the 165 cm^{-1} vibration of the C1/H1 group pushes C1/H1 towards O2 more than O1.

4.2.3. Comparing Motions at Specific Frequencies to Motions Occurring During VTST/MT Calculations of the Proton Transfer

It has been shown that the overall motion of C1 and H1 correspond quite closely to the motions required to achieve tunneling (Section 3.5). On the other hand, the above spectral density analysis suggests that the major motions of C1/H1 – the 165 cm^{-1} vibration – are not the strongest contributors to the squeezing of the C1-H1-O2 reaction coordinate. To investigate this apparent discrepancy, the 3-dimensional motions of these atoms at specific frequencies were analysed using digital filtering by frequency deconvolution (Section 2.7.4) of the same 400 ps MD simulation used in the previous analyses. The new velocities that are obtained are applied to the first structure from the simulation. This is important, since it means that the new coordinates represent an oscillation about this first structure, not the average structure (which would be a more accurate representation), and any direct measurement of distance or reaction coordinate will not be directly comparable to the values from the MD simulation.

Comparing the 3-dimensional nature of a vibration with the motions required to achieve tunneling, as determined from the VTST/MT calculation (Masgrau et al. 2006), gives an indication of how well this vibration will promote tunneling by pushing the system towards a tunneling configuration. A good measure for the

similarity between the required motions and a particular vibration is to measure the vector overlap (normalised cosine) between the vector for each atom describing the vibration and the vectors linking the atoms in the reactant (R) and the structure corresponding to the representative tunneling energy (RTE, the energy where the most tunneling occurs) – the R-to-RTE vectors. To this end, principal components analysis (PCA) was applied to the coordinates obtained from the digital filtering, and the eigenvector for the first principal component (PC1) is taken as the vector for the vibration. The R structure from the VTST/MT calculations was then aligned to the first structure of the MD simulation, and the same transformation matrix was applied to the RTE structure as the R structure. The R-to-RTE vectors can then be compared directly to the PC1 eigenvector for the vibration. However, it is important to realise that, since motions from PM3 calculations are being compared to motions from MM simulations, the results are more qualitative than quantitative.

The frequencies that are common to C1 and H1 are of particular interest, since these correspond to a vibration of the methylene group, which the VTST/MT calculations suggest is the main motion required to achieve a tunneling configuration. A window size of 60 cm^{-1} (i.e. ±30 cm^{-1}) was chosen, so to analyse the 165 cm^{-1} and 875 cm^{-1} vibrations (the two major peaks in the C1/H1 spectral densities), new sets of velocities were created for the 135-195 cm^{-1} and 845-905 cm^{-1} ranges, which were then applied to the first structure from the 400 ps MD window to create a new set of coordinates. The new coordinates for H1 for the 165 cm^{-1} and 875 cm^{-1} vibrations are shown in Figure 4.4. As expected, the 875 cm^{-1} vibration is far weaker
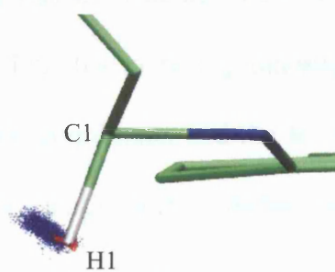
Figure 4.4. Coordinates from digital filtering of H1 motion: the 165 cm^{-1} (blue) and 875 cm^{-1} (red) vibrations of H1.

than the 165 cm^{-1} vibration, and will therefore squeeze the barrier far less efficiently.

When determining the vector overlaps, it is necessary to take into account the differences between the MM and PM3 structures; for example, the position of Asp128β in the starting structure for the 400ps MD simulation (which is not and energy minimised structure) differs significantly from its equilibrium position, and therefore a direct comparision with the R and RTE structures is not be the best approach. Therefore, the vector overlaps were calculated after aligning the Asp128β heavy atoms and the quinone and linker region from the PM3 structures separately onto the MM structure, so that the O1/O2 motions physically overlap the PM3 Asp128β oxygens as closely as possible.

To illustrate the vibrations, "cages" were created to represent the eigenvectors (the direction) and eigenvalues (the relative magnitudes), which were then superimposed onto the R and RTE structures. The 165 cm^{-1} vibrations for C1, H1, O1 and O2 are thus illustrated in Figure 4.5a, and the vector overlaps are listed in Table 4.2., along with the vector overlaps for the overall motion from the 4 ns MD simulation (Chapter 3). The C1, H1 and O2 motions are all very similar to the R-to-RTE vectors, therefore corresponding to the motions required to go from the R to the RTE configuration and thus achieve tunneling. Of course, the vector overlaps do not show whether this vibration actually pushes H1 towards O2, i.e. whether these two atoms push towards the RTE in phase or out of phase. For this to be a promoting vibration, it must be symmetrically coupled to the reaction coordinate, and the R-to-RTE vectors, which represent the motions along the free energy profile, define the reaction coordinate for this reaction. Therefore, to determine whether H1 and O2 move synchronously towards the tunneling configuration, PC1 for these atoms were plotted against each other, and the resulting correlation was compared with the

eigenvectors for PC1 of each atom (Figure 4.6): the eigenvectors for H1 and O2 are both positive and negative in the same direction relative to the R-to-RTE vectors, and are strongly correlated with a high R^2 value (0.87). H1 and O2 therefore move towards and away from the RTE in phase, which means that the vibration is in fact coupled to the reaction coordinate. This vibration does therefore correspond to a promoting vibration.

The overall motions of C1/H1 were previously found to be similar to the motions required for proton transfer to O2 (Table 4.2 and Figure 3.15), and the 165 cm^{-1} C1/H1 vibration is even more so, in agreement with the spectral densities
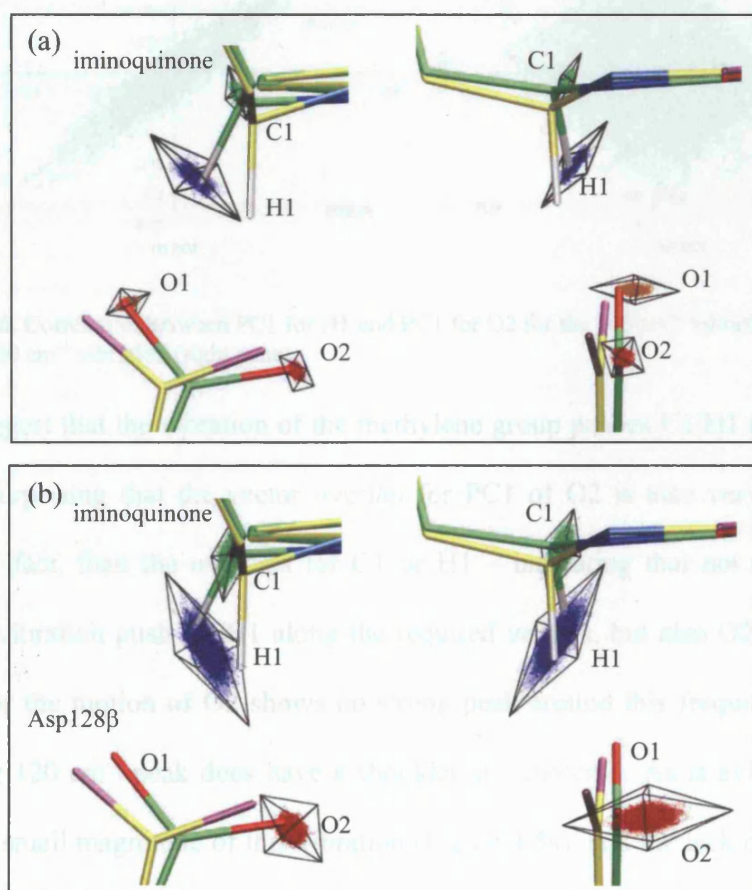
Figure 4.5. Orthogonal views for (a) the 165 cm^{-1} and (b) the 100 cm^{-1} vibrations for C1 (green dots), H1 (blue dots), O1 (orange dots, 170cm^{-1} only) and O2 (red dots) superimposed on the R (green carbon atoms) and RTE (yellow carbon atoms) structures from VTST/MT calculations. The cages represent the principal components for each atom, and are scaled according to the relative eigenvalues.

	PC1 of overall vibration (4ns)		PC1 of 165cm^{-1} vibration (400ps)		PC1 of 100cm^{-1} vibration (400ps)	
	R-to-RTE overlap	Percent of motion	R-to-RTE overlap	Percent of motion	R-to-RTE overlap	Percent of motion
C1	0.81	48	0.916	59	0.731	53
H1	0.91	54	0.936	62	0.799	59
O1	0.70	40	0.235	53	-	-
O2	0.63	50	0.996	47	0.689	51

Table 4.2. Overlaps with R-to-RTE vectors and percent of motion for PC1 of overall motion and motion at specific frequencies for C1, H1, O1 (except 100 cm^{-1}) and O2.
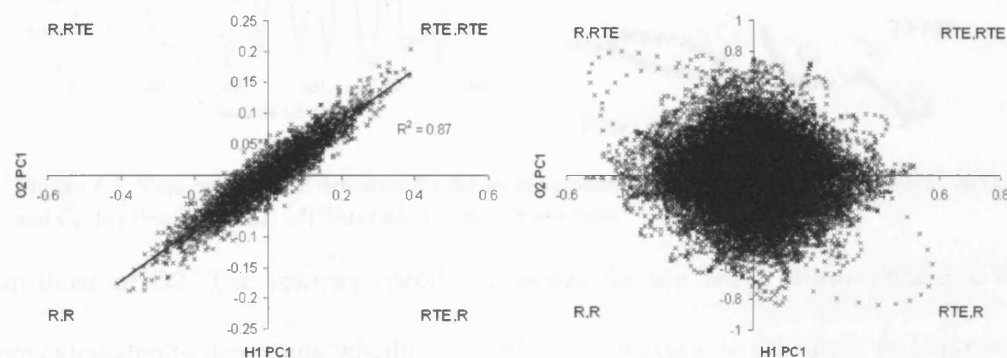
Figure 4.6. Correlation between PC1 for H1 and PC1 for O2 for the 165 cm^{-1} vibration (left pane) and the 100 cm^{-1} vibration (right pane).

which suggest that the vibration of the methylene group pushes C1/H1 towards O2. It is more surprising that the vector overlap for PC1 of O2 is also very high – even higher, in fact, than the overlaps for C1 or H1 – indicating that not only does the 165 cm^{-1} vibration push C1/H1 along the required vectors, but also O2. The spectral density for the motion of O2 shows no strong peak around this frequency, although the strong 120 cm^{-1} peak does have a shoulder at ~165 cm^{-1}. As is evident from the relatively small magnitude of this vibration (Figure 4.5a), and the lack of a prominent peak in the O2 spectral density, this motion is not significant to the overall motion of O2. This is further supported by the percentage of motion represented by PC1 for each atom, which indicate that the C1 and H1 vibrations are more strongly focused
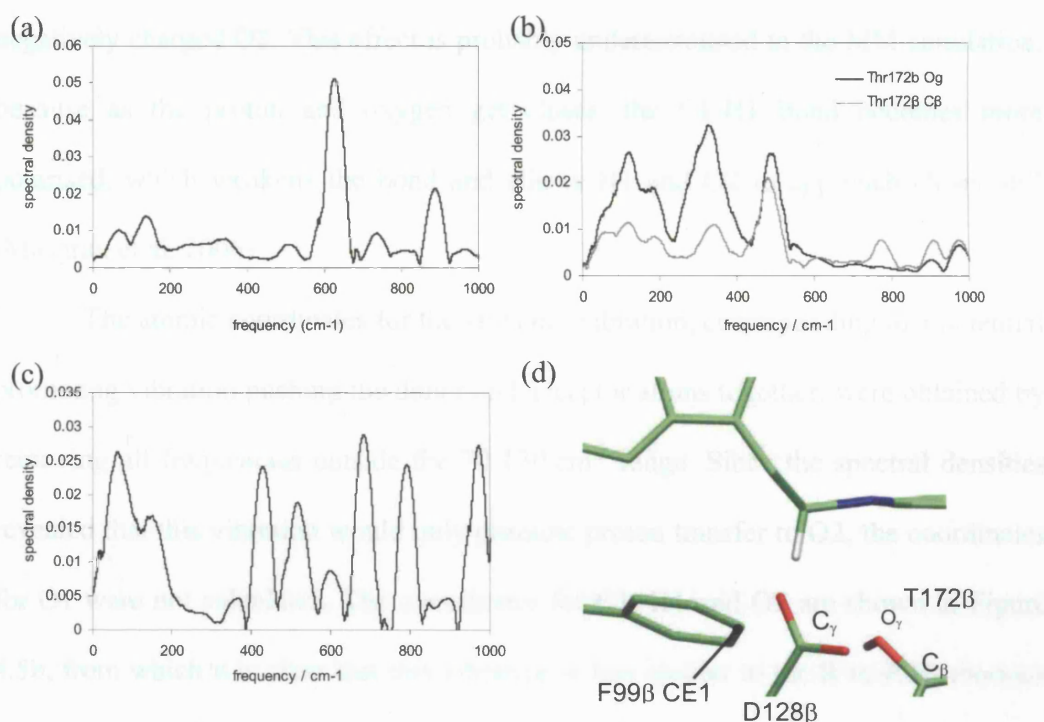
Figure 4.7. Velocity spectral densities for the atoms nearest O2: (a) Asp128β C_γ, (b) Thr172β O_γ and C_β, (c) Phe169β CE1; (d) illustration of the atoms used

than those of O2. The velocity spectral densities for the heavy atoms closest to O2 were calculated to determine whether the 165 cm⁻¹ vibration in O2 might be caused by a larger network of vibrations (Figure 4.7). The strongest low-frequency peak for Asp128β C_γ is at ~145cm⁻¹, corresponding to the ~145cm⁻¹ peak for O1, and the strongest peak in the spectral density for Thr172β O_γ - the hydrogen-bonding partner of O2 – in the region of 165 cm⁻¹ is at ~125cm⁻¹, corresponding the ~120cm⁻¹ peak for O2. There is a fairly strong shoulder at ~165 cm⁻¹, but the velocity spectral density for the adjacent atom, Thr172β C_β is much weaker and does not have a peak at ~165 cm⁻¹. Therefore, these atoms appear to be responsible for the major vibrations of O1 and O2, but not the 165 cm⁻¹ vibration of O2. The strongest low-frequency peak for the nearest Phe169β heavy atom is at ~70 cm⁻¹, with a smaller peak at ~150 cm⁻¹ of about half the strength of the O2 spectral density at ~165 cm⁻¹. Thus Phe169β does not either give rise to the 165 cm⁻¹ vibration in O2. This vibration is therefore most likely caused by electrostatic attraction between the positively charged H1 and the

negatively charged O2. This effect is probably underestimated in the MM simulation, because as the proton and oxygen get closer, the C1-H1 bond becomes more polarised, which weakens the bond and allows H1 and O2 to approach closer still (Masgrau et al. 2006).

The atomic coordinates for the 100 cm^{-1} vibration, corresponding to a potential promoting vibration pushing the donor and acceptor atoms together, were obtained by removing all frequencies outside the 70-130 cm^{-1} range. Since the spectral densities revealed that this vibration would only promote proton transfer to O2, the coordinates for O1 were not calculated. The coordinates for C1, H1 and O2 are shown in Figure 4.5b, from which it is clear that this vibration is less similar to the R-to-RTE motions than the 165 cm^{-1} vibration; the vector overlaps for these motions are lower than those for the 165 cm^{-1} motions, the values for C1 and H1 being lower than for the overall motion (Table 4.2). The 100 cm^{-1} motions of O2 do not sample coordinates as close to the RTE structure as the 165 cm^{-1} motions. Furthermore, the 100 cm^{-1} motions of H1 and O2 are not coupled (Figure 4.6b), which means that while this vibration does modulate the C1/H1-O2 distances, it is not symmetrically coupled to the reaction coordinate.

Comparing the motions of the 100 cm^{-1} and the 165 cm^{-1} motions (Figure 4.5) offers an insight into the nature of the motions required for tunneling. The 100 cm^{-1} coordinates for O2 lie further from the RTE structure than the 165 cm^{-1} coordinates. Note that the 70-130 cm^{-1} range used for to obtain these motions covers the main vibration of O2 at 120 cm^{-1}. This suggests that the major vibration of O2 serves as an initial preorganisation, which is required to achieve a certain minimum H1-O2 distance. Once O2 is close enough to H1, the 165 cm^{-1} vibration pushes C1, H1 and O2 towards the point of tunneling. Thus, while the 165 cm^{-1} vibration occurs

constantly in C1/H1, it only occurs in O2 once it has been positioned sufficiently close to interact with C1/H1. This explains why the peak at 165 cm^{-1} is only a relatively weak shoulder in the O2 spectral density.

From these results it is apparent that vibrations that most strongly push the donor and acceptor atoms along the axis between them do not necessarily correspond to the vibrations that most efficiently push the donor, proton and acceptor towards their reactive positions, in this case the positions required for tunneling. This is because the most effective promoting vibration is one which pushes the reactant and product wells together, which means pushing the positions of the hydrogen wavefunctions in the reactant and product states together, i.e. pushing together the donor and acceptor orbitals. If the donor, proton and acceptor atoms are not aligned, this is not the same as pushing these atoms along the donor-acceptor axis. In Figure 4.5, it is easy to see that the proton in the RTE configuration is nearer the lone pair orbital of O2 than the proton in the R configuration. It is therefore necessary to expand on the diagnosis for a promoting vibration developed by Schwartz and co-workers (Caratzoulas and Schwartz 2001), to take into account the 3-dimensional requirements of a promoting vibration.

4.3. Determining if other atoms/residues are involved in the promoting vibration

Cross-correlation analysis revealed that the motions of C1/H1 are not coupled to the overall motions of surrounding atoms or residues (Chapter 3). However, this does not rule out the possibility of a network of vibrations at 165 cm^{-1} which is coupled to the promoting vibration. Therefore, to determine whether the 165 cm^{-1} promoting vibration is caused by large-scale protein motion or just by the vibration of the

iminoquinone methylene C1, spectral density analysis was carried out to diagnose whether heavy atoms surrounding the C1 are coupled to the motion of C1 at this frequency. Mincer and Schwartz used the criterion that if an atom (or, in their case, residue centre of mass) participates in the promoting vibration then there must be a vibration at the same frequency which has a strong component along the vector connecting the atom and the donor or acceptor atom *and* along the donor-acceptor axis (Mincer and Schwartz 2003). The reason is that, in their analysis, the atom in question was required to push the donor or acceptor atom along the donor-acceptor axis. However, this is based on the assumption that the promoting vibration is the one that most effectively reduces the donor-acceptor axis, and therefore the donor-acceptor relative velocity spectral density was used as the reference. In this case, the promoting vibration comes from the vibration of the donor carbon, C1, so the velocity spectral density for C1 is used as the reference. Furthermore, an atom that participates in the promoting vibration might not necessarily push towards C1, since the motion of two atoms can also be coupled through non-covalent interaction such as van der Waals or electrostatic interactions, or through covalent bonding. Therefore, the criterion for an atom being coupled to the motion of C1 is that it has a vibration at about $165 \, cm^{-1}$ which is strongly correlated with the $165 \, cm^{-1}$ vibration of C1. The reason that the velocity spectral density for H1 was not used for this analysis, even though H1 is also involved in the promoting vibration, is that the magnitude of the H1 velocity spectral density is much greater than that of heavy atoms (Figures. 4.2 & 4.7), and therefore if the vibration is part of a larger network of coupled vibrations (which will mainly involve heavy atom motion), it will be coupled via C1.

Therefore, to determine whether a specific atom A is involved in the promoting vibration, the spectral density for the time-correlation function (McQuarrie

2000) for the velocities of C1 and the atom A was used. The time-correlation function

for A and C1 is defined as:

$$C_{A,C1}(i) = \left\langle v_A(t+i).v_{C1}(t) \right\rangle \qquad (4.1)$$

Both $C_{A,C1}(i)$ and $C_{C1,A}(i)$ were calculated and averaged to give $C(i)$, whose

autocorrelation function was then Fourier transformed to give the spectral density.

The strength of this spectral density at around 165 cm^{-1} was assumed to be a good

measure for the strength of coupling between A and C1 at that frequency. However,

as shall be explained, this is not necessarily the case.

Both the velocity and time-correlation spectral densities for all atoms that

never move further than 12Å from C1 were calculated, and the values $V(f_1-f_2)$ and

$C_T(f_1-f_2)$ were defined as the areas under the velocity and time-correlation spectral

densities in the frequency range defined by f_1 and f_2, divided by the area in the same

frequency range for the C1 spectral density (for which the time-correlation spectral

density is identical to the velocity spectral density). $C_T(135-195)$, was used as an

initial measure for the correlation with the C1 vibration at 165 cm^{-1}. Note that, since

the VAF for calculating $C_T(f_1-f_2)$ for atom A comes from $\langle v_{C1}.v_A \rangle$, it is possible to have

a $C_T(135-195)$ value greater than 1 if the velocity spectral density for atom A in the

135-195 cm^{-1} range is stronger than that of C1 in the same range. Figure 4.8 plots

$C_T(135-195)$ and $V(135-195)$ versus distance from C1, as well as $C_T(135-195)$ versus

$V(135-195)$.

It quickly became apparent that $C_T(f_1-f_2)$ is not an accurate measurement of the

correlation, due to the fact that it takes into account both the magnitude and

directionality of both atoms. This means that for any given threshold, $C_T(135-195)$ can

lie above the threshold with a relatively weak vibration if the direction of the vibration is close to that of the C1 vibration, or with a strong vibration in a different direction to the C1 vibration. For example, Asp128β O1 has a $C_T(135-195)$ value of 0.60, even though its motion in the 135-195 cm^{-1} range was previously shown to lie predominantly in a very different direction to that of C1 (Figure 4.5a), because its
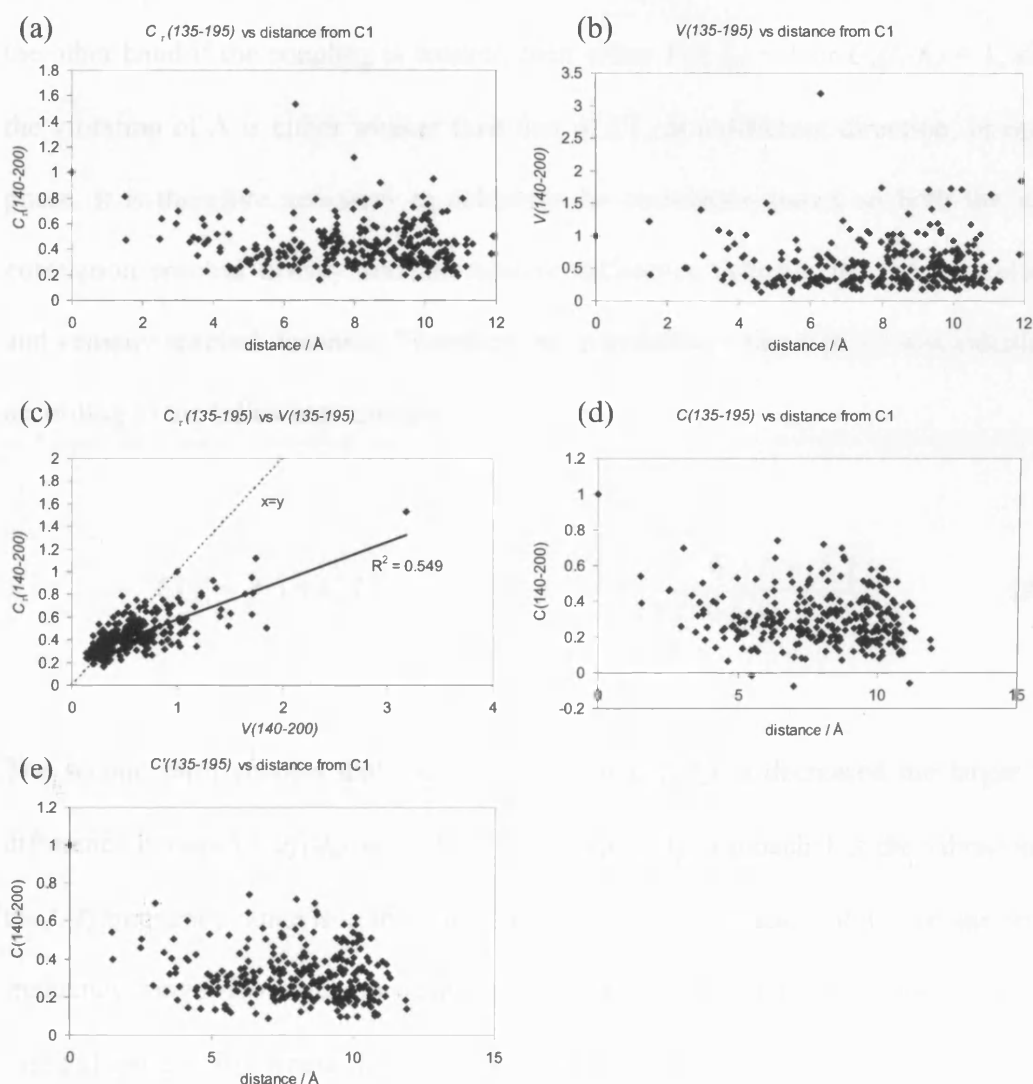
Figure 4.8. Vibrational strengths and couplings from spectral density calculations for atoms that never move beyond 12 Å from C1: areas under the 135-195cm^{-1} range relative to the area under the C1 velocity spectral density for the same range for (a) time-correlation [$C_T(135-195)$] and (b) velocity [$V(135-195)$] spectral densities *versus* distance from C1 ; (c) plot of $C_T(135-195)$ vs $V(135-195)$; (d) correlation values $C(135-195)$, according to equation (4.2) and (e) $C'(135-195)$, according to equation (4.3).

V(135-195) value is 1.4 times that of C1. Asn122C$_\beta$, on the other hand has a *C$_\tau$(135-195)* value of 0.63 even though its *V(135-195)* value is only 0.45.

To further understand how *V(f$_1$-f$_2$)* and *C$_\tau$(f$_1$-f$_2$)* relate to the coupling between vibrations in the *f$_1$-f$_2$* range, consider *V(f$_1$-f$_2$)* and *C$_\tau$(f$_1$-f$_2$)* for an atom A. In the perfectly coupled case, *V(f$_1$-f$_2$)* ≥ *C$_\tau$(f$_1$-f$_2$)* ≥ 1, since this means the vibration of atom A is at least as strong as the vibration of C1, in the same direction and in phase. On the other hand if the coupling is weaker, then either *V(f$_1$-f$_2$)* < 1 or *C$_\tau$(f$_1$-f$_2$)* < 1, since the vibration of A is either weaker than that of C1, in a different direction, or out of phase. It is therefore necessary to calculate the correlation based on both the time-correlation spectral density and the relative difference between the time-correlation and velocity spectral densities. Therefore, the correlation value *C(f$_1$-f$_2$)* was calculated according to the following equation:

$$C(f_1 - f_2) = C_\tau(f_1 - f_2) \times \left[1 - \frac{|V(f_1 - f_2) - C_\tau(f_1 - f_2)|}{V(f_1 - f_2)} \right] \qquad (4.2)$$

The second term ensures that the magnitude of *C(f$_1$-f$_2$)* is decreased the larger the difference between *C$_\tau$(f$_1$-f$_2$)* and *V(f$_1$-f$_2$)*, and will only approach 1 if the vibration in the *f$_1$-f$_2$* frequency range is in the same direction as the vibration of C1 in the same frequency range. However, this equation results in a negative *C(135-195)* in a few cases (Figure 4.8d) where *V(135-195)* is more than twice as low as *C$_\tau$(135-195)*. Equation 4.2 was therefore adapted to:

$$C'(f_1 - f_2) = C_\tau(f_1 - f_2) \times \left[1 - \frac{|V(f_1 - f_2) - C_\tau(f_1 - f_2)|}{\max[V(f_1 - f_2), C_\tau(f_1 - f_2)]} \right] \qquad (4.3)$$
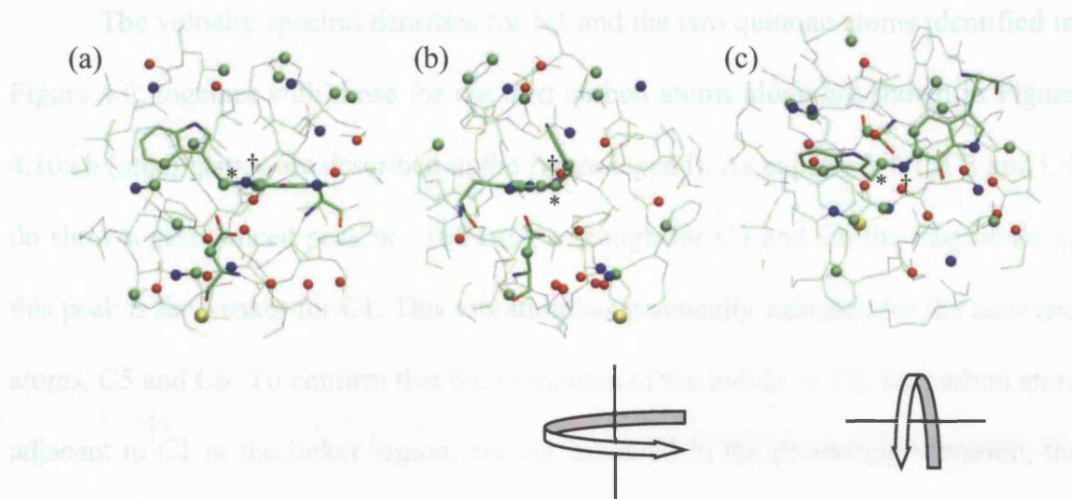
Figure 4.9. Orthogonal views of atoms surrounding C1 with *C'(140-200)* > 0.5. All the atoms used in the analysis are shown as lines, the iminoquinone and Asp128β as thicker lines, and the atoms with *C'(140-200)* > 0.5 as spheres. The diagram below views (b) and (c) illustrate how each is obtained from rotation of (a). * designates C1 and † designates N1. N1 is immediately behind C1 in panel (b).

This alteration only makes a difference to those atoms with a low *V(135-195)* and $C_T(135-195)$ values, since only these atoms can have *V(135-195)* values twice as low as their $C_T(135-195)$ values (Figure 4.8d).

The values for *C'(135-195)* are plotted versus the distance from C1 in Figure 4.8d). Using this measure, very few atoms are strongly correlated with C1, with none having *C'(135-195)* values above 0.8. 13% of the atoms (36 out of a total of 285) have values above 0.5. (Using Equation 2.2, 34 atoms have values above 0.5). These atoms appear randomly scattered around C1 (Figure 4.9), N1 being the only atom capable of transferring its vibrational energy directly to C1, and within the selection N1 is only adjacent to two atoms in the quinone. Therefore, even using a low cutoff value of 0.5, there is no indication of a network of atoms that might give rise to the 165 cm^{-1} vibration of C1, indicating that the 165 cm^{-1} vibration is inherent in the iminoquinone.

The velocity spectral densities for N1 and the two quinone atoms identified in Figure 4.9, together with those for the next carbon atoms along are shown in Figure 4.10a,b (atom names are described in the figure legend). As expected, N1, C3 and C4 do show a pronounced peak at ~165 cm^{-1}, although for C3 and C4 the magnitude of this peak is far weaker for C1. This vibration has practically vanished for the next two atoms, C5 and C6. To confirm that the vibrations of the indole or C2, the carbon atom adjacent to C1 in the linker region, are not involved in the promoting vibration, the velocity spectral densities for C2, the indole heavy atom centroid and selected indole atoms are shown in Figure 4.10c,d. C2 shows a peak at ~165 cm^{-1}, although it is
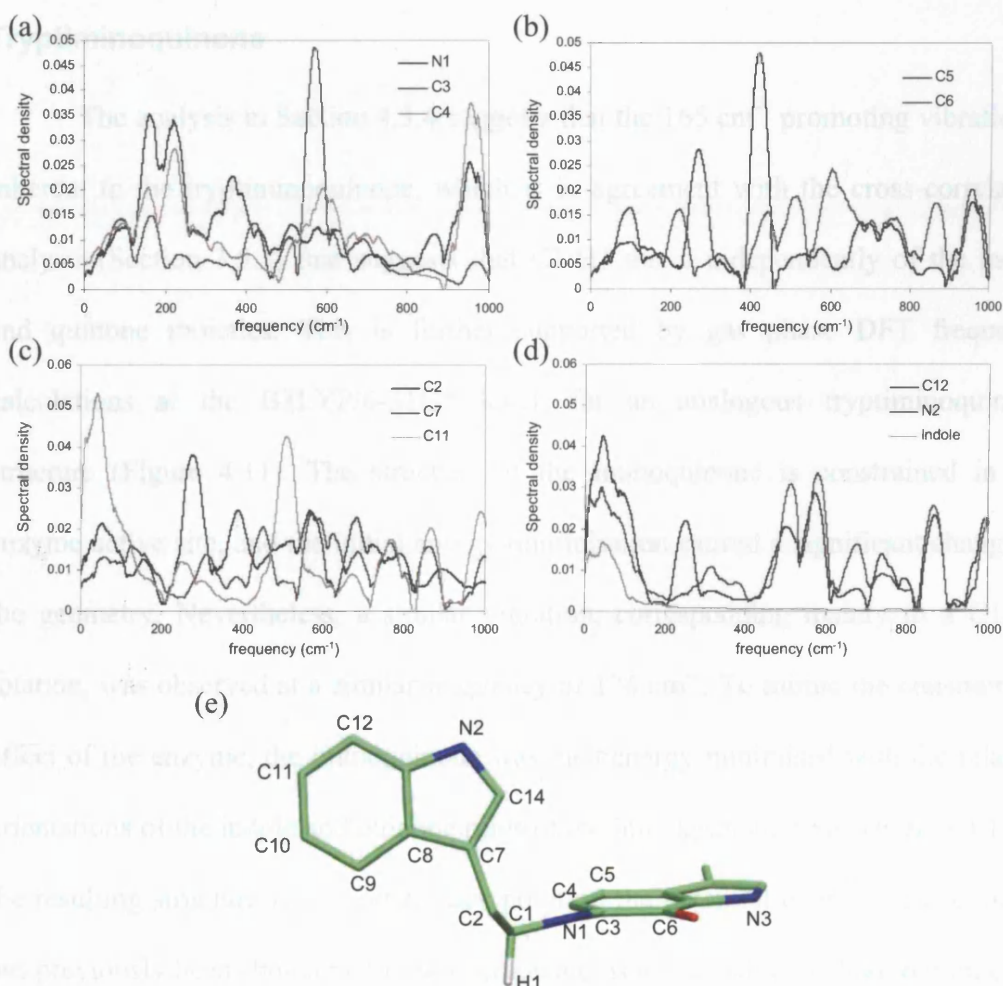
Figure 4.10. Velocity spectral densities for selected tryptiminoquinone atoms: (a) N1, C3, C4; (b) C5, C6; (c) C2, C7, C11; (d) C12, N2, indole heavy atom centroid; (e) atom numbering.

significantly weaker than the C1 peak, and the indole centroid shows only one strong peak at ~50 cm^{-1}. That the indole centroid does not show any high-frequency peaks is because vibrations that are specific to individual atoms become averaged out when calculating the spectral density for a multiple-atom selection. This confirms that the 165 cm^{-1} promoting vibration is small-scale local vibration, and that the only atoms which can contribute significantly to the vibration of C1 within the tryptiminoquinone are the same atoms that were diagnosed earlier.

4.4. Quantum Mechanical Frequency Calculations of the Tryptiminoquinone

The analysis in Section 4.3.4 suggests that the 165 cm^{-1} promoting vibration is inherent to the tryptiminoquinone, which is in agreement with the cross-correlation analysis (Section 3.5.1) that suggests that C1/H1 move independently of the indole and quinone moieties. This is further supported by gas phase DFT frequency calculations at the B3LYP/6-31G* level, for an analogous tryptiminoquinone structure (Figure 4.11). The structure of the iminoquinone is constrained in the enzyme active site, and the initial energy minimisation caused a significant change in the geometry. Nevertheless, a similar vibration, corresponding mainly to a C1/H1 rotation, was observed at a similar frequency of 174 cm^{-1}. To mimic the constraining effect of the enzyme, the iminoquinone was then energy minimised with the relative orientations of the indole and quinone rings of the iminoquinone fixed (Figure 4.11b); the resulting structure is a nonstationary point on the potential energy surface, but it has previously been shown that fixing certain atoms is a suitable method to mimic the strain of the enzyme (Siegbahn 2003). This gave a frequency of 164 cm^{-1} for the C1/H1 rotation. These calculations confirm that the promoting vibration is inherent to

the tryptiminoquinone, especially in the conformation adopted in the protein environment.
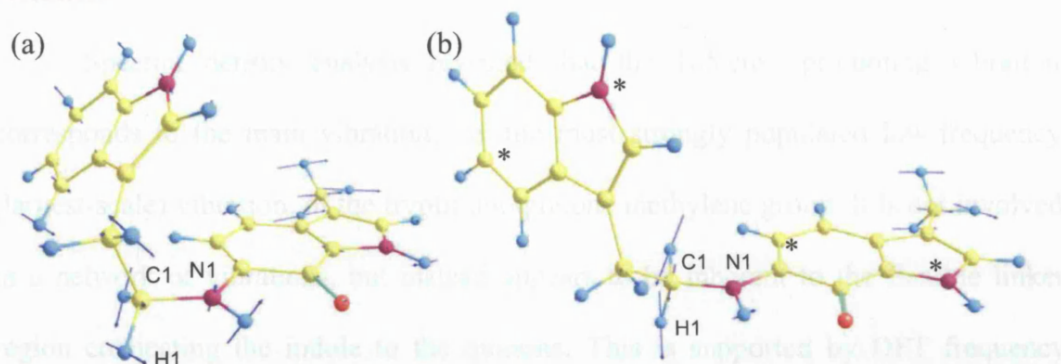
Figure 4.11. B3LYP/6-31G* energy minimised iminoquinone structure, with scaled arrows representing the vibration for the C1/H1 rotation: (a) without any constraints (174 cm^{-1}), (b) with indole/quinone orientations fixed by fixing the relative positions of the marked atoms (164 cm^{-1}).

4.5. Conclusions

A vibration has been identified that promotes tunneling by pushing the reacting atoms – C1, H1 and O2 – towards the tunneling configuration. This 165 cm^{-1} vibration minimises the C1/H1-O2 distances and the reaction coordinate, although it does not correspond the vibration that most effectively modulates these distances. It is, however, symmetrically coupled to the reaction coordinate, and will therefore act as a promoting vibration. In this case the criteria used by Schwartz and co-workers to identify a promoting vibration (Caratzoulas and Schwartz 2001) is not applicable, since it assumes that the vibration that pushes the donor and acceptor atoms most strongly along the donor-acceptor axis (and therefore the vibration with the strongest donor-acceptor distance modulation) will most effectively promote the reaction. The difference between such a vibration and the promoting vibration observed here is illustrated in Figure 4.12: in Panel A, achieving a tunneling configuration does not require a promoting vibration that pushes the donor, proton and acceptor along the

donor-acceptor axis; in Panel B, on the other hand, when the donor, transferring proton and acceptor are aligned, such a vibration will be the most effective promoting vibration.

Spectral density analysis revealed that the 165 cm^{-1} promoting vibration corresponds to the main vibration, i.e. the most strongly populated low-frequency (largest-scale) vibration, of the tryptiminoquinone methylene group. It is not involved in a network of vibrations, but instead appears to be inherent to the flexible linker region connecting the indole to the quinone. This is supported by DFT frequency calculations on the tryptiminoquinone structure, which revealed that such a vibration is in fact inherent to the tryptiminoquinone. Therefore, in terms of promoting the proton transfer, the role of the enzyme in this case appears to be that of a scaffold that holds the donor and acceptor groups such that the vibrations inherent in the donor group promote the reaction.
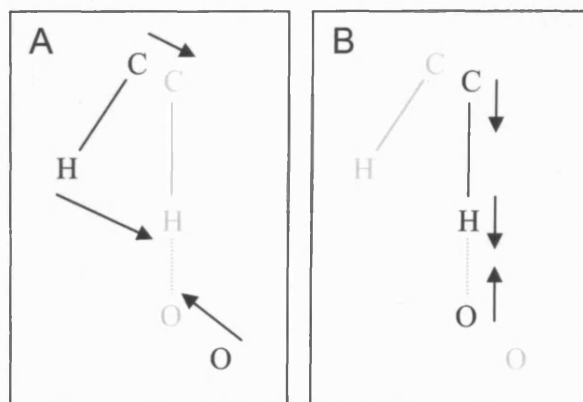
Figure 4.12. Schematic illustration of two potential promoting vibrations: (A) the promoting vibration observed in AADH:tryptiminoquinone; (B) a promoting vibration when the donor, transferring proton and acceptor atoms are aligned.

5. Hybrid Quantum Mechanical / Molecular Mechanical Simulations of the Proton Transfer Step

5.1. Preface

Hybrid QM/MM simulations were carried out for two purposes: to analyse the energetics of proton transfer, and to study the motions required to bring the system to a tunneling configuration. Since MM does not allow the breaking and making of bonds, insight into how the structure of the enzyme and iminoquinone affect the energetics of proton transfer requires QM treatment of the reacting moieties. Furthermore, while important insight into motions, both global (Chapter 3) and local (Chapter 4), was obtained from MM MD simulations, a more precise analysis of the motions that occur as the enzyme moves towards the tunneling configuration requires QM treatment, since tunneling requires C1 and O2 to approach nearer than the sum of their van der Waals radii (Masgrau et al. 2006). However, the tunneling configuration is statistically too unlikely to occur during standard MD simulations, since reaction rates are typically on the millisecond timescale ($3500\,s^{-1}$ in this case) while MD simulations are limited to the nanosecond timescale, both because of the computational time required and because the nature of the simulations is such that numerical errors are introduced from rounding and truncation in the integration algorithm which prevent the unlimited extension of the simulation (Antoniou et al. 2004). Instead, the motions that occur during the reactive event can be observed by first forcing the system to a putative transition state and then allowing it to relax by unrestrained MD simulations: the motions that move the system away from the transition state to the reactant are the opposite of those required to bring the system to the transition state from the reactant. Assuming that the classical pathway and the tunneling pathway do not differ significantly in the motions of the heavy atoms (i.e. that the main difference is in the nature of the proton transfer event), then the tunneling configuration is expected to lie close to the transition state, and therefore the

motions required to bring the system towards a tunneling configuration can be observed.

5.2. QM/MM MD simulations of the AADH:tryptiminoquinone $\alpha_2\beta_2$ heterotetramer

To obtain starting structures (and velocities) for the calculations outlined above, two unrestrained 200 ps simulations were run, each with the QM region as illustrated in Figure 5.1 applied to one of the two dimers ($A,H/B,D$), starting from a structure after 2 ns of MM MD simulation, so that the enzyme structure has been equilibrated. The simulations were run using the same method as the MM simulations, i.e. constant temperature and pressure (CPT) at 300 K using CHARMM, version 27 with the CHARMM22 force field for the MM region. The QM region was treated using the Austin model 1 (AM1) semi-empirical method (Dewar et al. 1985). In this case, SHAKE was not employed, so a 1 fs timestep was used. The protocol used was as follows: (1)
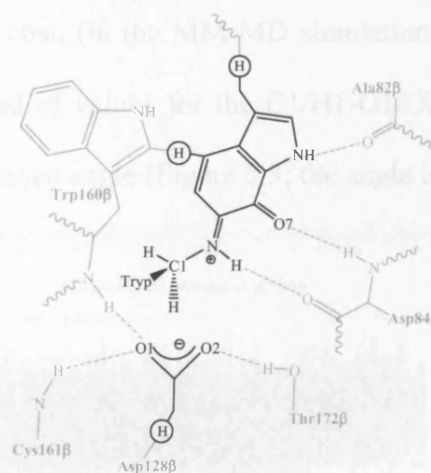
Figure 5.1. Schematic of the QM/MM partition used for the AM1/MM simulations for AADH:tryptiminoquinone. The QM region is shown in black and part of the surrounding QM/MM region in grey with link atoms are circled. Hydrogen bonds between the QM region and MM residues are depicted by dotted lines.

the QM region was defined; (2) the MM region was fixed and the QM region energy minimised by adopted-basis Newton Raphson minimisation (ABNR) until a gradient of 0.1 kcal/mol/Å was achieved (3) the entire structure was minimised first using Steepest Descent (SD) until a gradient of 0.5 kcal/mol/Å was achieved, then by ABNR until a gradient of 0.1 kcal/mol/Å was achieved; (4) the system was thermalised over 12 ps, with a 5 K increase in temperature every 200 integration

steps; (5) 30 ps of simulation were run at constant temperature for equilibration; (6) 200 ps of simulation were run for analysis.

The C1/H1-O1/O2 distances for the 200 ps analysis run are shown in Figure 5.2. These distances are shorter than those from the MM MD simulations (Chapter 3). As with those simulations, O2 is, on average, further from C1/H1 than O1. This is consistent with the VTST/MT calculations (Masgrau et al. 2006), where, although O2 is further away, it is the preferred proton acceptor both kinetically and thermodynamically. Critically, these simulations agree well with the VTST/MT calculations where the H1-O2 distance achieves a distance of ~2Å, from the minimum energy configuration at a relatively low energetic cost, (in the MM MD simulations the H1-O2 distance never reaches 2Å). The spread of values for the C1/H1-O1/O2 distances for both subunits, and also the indole-quinone angle (Figure 5.3; the angle is
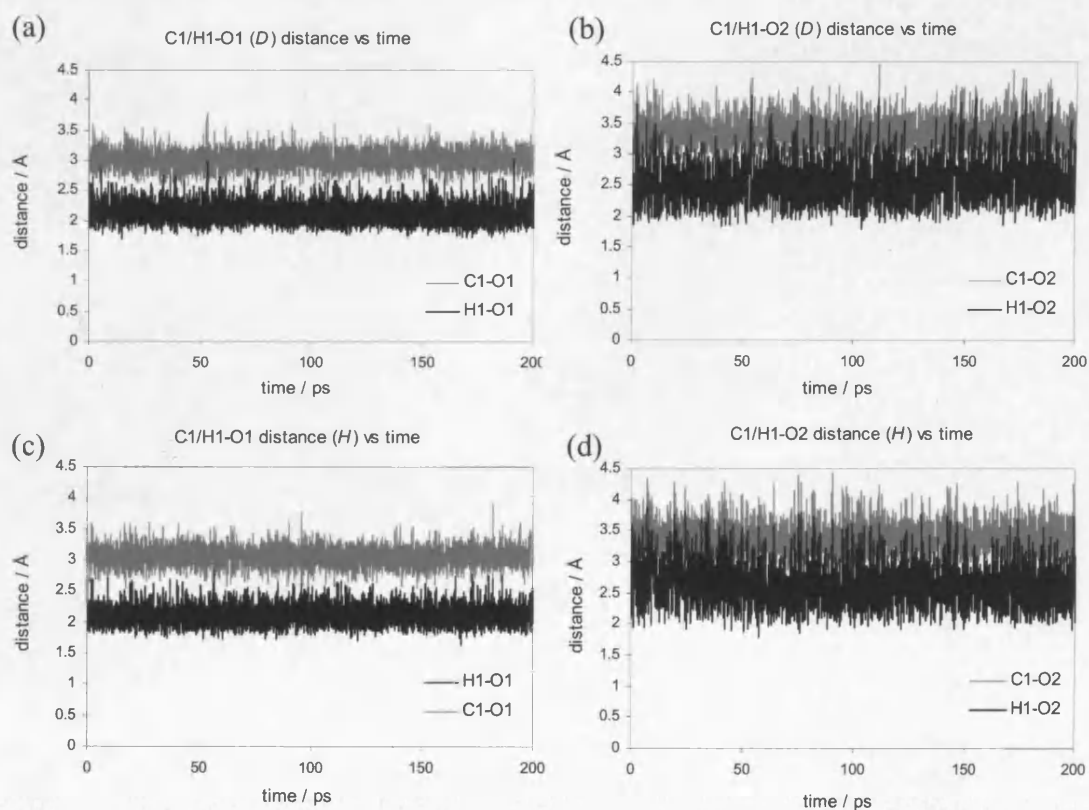
Figure 5.2. C1/H1-O1/2 distances for the *H* (a,b) and *D* (c,d) subunits *versus* time.

defined in Figure 3.6), are similar to those for the MM MD simulations for the *H*-subunit.

Since the VTST/MT results (Masgrau et al. 2006) support the mechanistic requirement that proton transfer occurs to O2 (Chapter 2), the following discussions will focus on proton transfer to O2. Also, since the active sites from both dimers seem to behave similarly, and the *A,H* dimer was the most reliable from the MM simulations, further calculations stem from the AM1/MM simulation where the *A,H* reacting moieties are treated quantum mechanically.
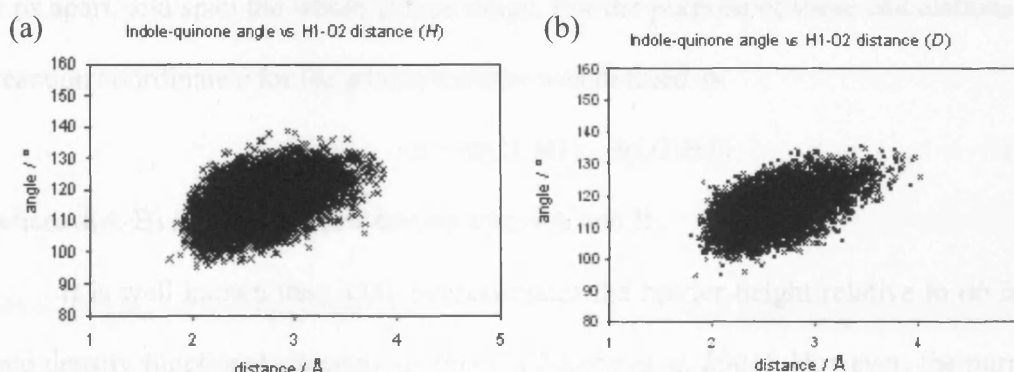
Figure 5.3. Indole-quinone angle *versus* H1-O2 distance for the (a) *H* and (b) *D* subunits.

5.3. Potential Energy Surfaces for AADH:tryptimiminoquinone

As discussed above, VTST/MT calculations have been carried out previously to determine precisely the contribution of tunneling: proton transfer occurs in excess of 99.9% by tunneling. Prior to this, the H1-O2 distance is reduced by classical activation to ~1.64 Å (Masgrau et al. 2006). Since the rate for this proton transfer step is reported as ~3500 s^{-1} (Masgrau et al. 2006), it is not surprising that such a short distance was not observed in the 200 ps AM1/MM simulations. However, important insight into how the dynamics of the system might affect the proton transfer reaction can still be obtained from these simulations, in particular concerning the effect of

dynamics on the proton transfer step and whether factors other than the O2-H1 distance determine the likelihood of the proton transfer.

The effect of protein and iminoquinone configuration on the potential energy barrier was studied by calculating the one-dimensional potential energy surface (PES), using AM1/MM, for snapshots taken from this MD simulation. 200 Snapshots were taken at 1 ps intervals, and a further 11 structures with the shortest H1-O2 distances were also selected, since the shortest distances are statistically too infrequent to be selected by sampling every ps. These 11 structures were all at least 5 ps apart, and span the whole 200 ps range. For the purpose of these calculations, the reaction coordinate z for the proton transfer was defined as

$$z = d(C1\text{-}H1) - d(O2\text{-}H1) \tag{5.1}$$

where d(A-B) is the distance between atoms A and B.

It is well known that AM1 overestimates the barrier height relative to *ab initio* and density functional calculations (Garcia-Viloca *et al.* 2001). However, the purpose of this study is not to reproduce experimental results or to produce a quantitative description of the potential energy surfaces: the goal is to analyse *trends* in the potential energy surfaces based on the configuration of the reactant (i.e. the MD snapshot).

Initially, the PESs were calculated without any constraints on the MM region, so that the MM atoms could move in response to the changes in the QM region as the proton was transferred. However, this typically results in the system jumping from one PES to another (Figure 5.4) as this
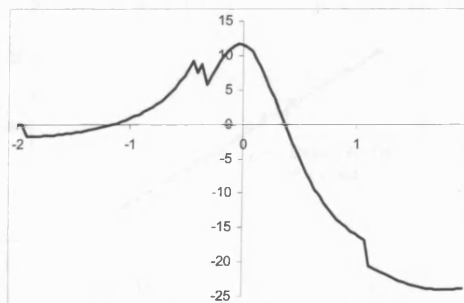
Figure 5.4. Example of a potential energy surface calculated with the MM region unrestrained.

allows it to find lower energy configurations. It is important not to restrict the MM region completely, since some structural rearrangement is probably required for the proton transfer to take place. A harmonic constraint of 10 kcal/Å^2/mol was selected, as this represents a good compromise between preventing jumps to "lower" energy surfaces and allowing the MM region to move, and a similar constraint has previously been used in the calculation of potential energy surfaces for MD snapshots (Nunez *et al.* 2004). The PESs calculated using this constraint are not completely smooth (e.g. Figure 5.5), i.e. there is some shifting between potential energy surfaces. However, initial PES calculations for 15 structures revealed no difference when a harmonic constraint of 15 kcal/Å^2/mol was used instead (Figure 5.6). It is important to keep in mind that constraining the MM region will cause the PES to be overestimated, since it means more energy is required for any necessary structural rearrangements to take place, but, as mentioned above, this is a qualitative study, and any difference in activation energy or barrier height/width reflects the difference in energy required for the proton transfer to take place.

Each PES was calculated from $z = -2$ to $z = 2$ according to the following protocol: (1) minimise the QM region with all the MM atoms fixed and z restrained at
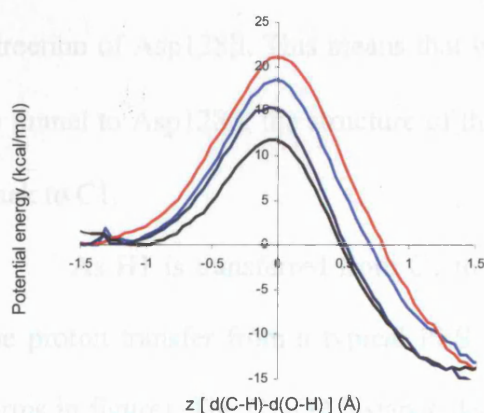
Figure 5.5. Four example potential energy surfaces, representing the lowest/narrowest (black) to the tallest/widest (red).
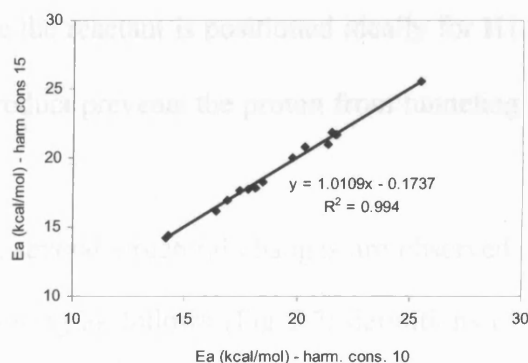
Figure 5.6. Comparing activation energies calculated using a harmonic constraint of 15 and 10 kcal/mol/Å^2 (labeled harm. cons. 10 and 15).

$$y = 1.0109x - 0.1737$$
$$R^2 = 0.994$$

the value in the MD snapshot using a harmonic restraint of 5000 kcal/Å^2/mol; (2) apply a harmonic constraint of 10kcal/Å^2/mol to all MM atoms to ensure that the system remains on one PES; (3) incrementally increase/decrease z by 0.05Å using a harmonic restraint of 5000 kcal/Å^2/mol and energy minimize to obtain the potential energy at each point.

The PES fluctuates significantly during the MD simulation (Figure 5.5), both in terms of height and width. Note that although the PESs were not calculated until the minimum on the product side was reached, it is clear that the PESs are highly exothermic, the lowest ones by more than 15 kcal/mol, and that the enzyme structure is therefore able to accommodate the increasing H1-O2 distance. This is an important result, since exothermicity lowers the activation energy and prevents the back-reaction, and it has been suggested that exothermicity facilitates tunneling in the analogous enzyme MADH (Nunez *et al.* 2006). Initially this exothermicity might seem surprising, since a hydrogen-oxygen bond is typically easier to break than a carbon-hydrogen bond, so that the back-reaction should require less energy than the forward reaction. However, C1 becomes sp^2 hybridised as it loses H1 and the electronic reorganisation of the quinone leads to a C1-N1 double bond, and the sp^2 orbitals lie along the plane of the C1-N1 double bond, nearly perpendicular to the direction of Asp128β. This means that while the reactant is positioned ideally for H1 to tunnel to Asp128β, the structure of the product prevents the proton from tunneling back to C1.

As H1 is transferred from C1 to O2, several structural changes are observed, the proton transfer from a typical PES occurring as follows (Fig 5.7; definitions of terms in figure). The C1-O2 distance decreases to about 2.7Å and the indole-quinone
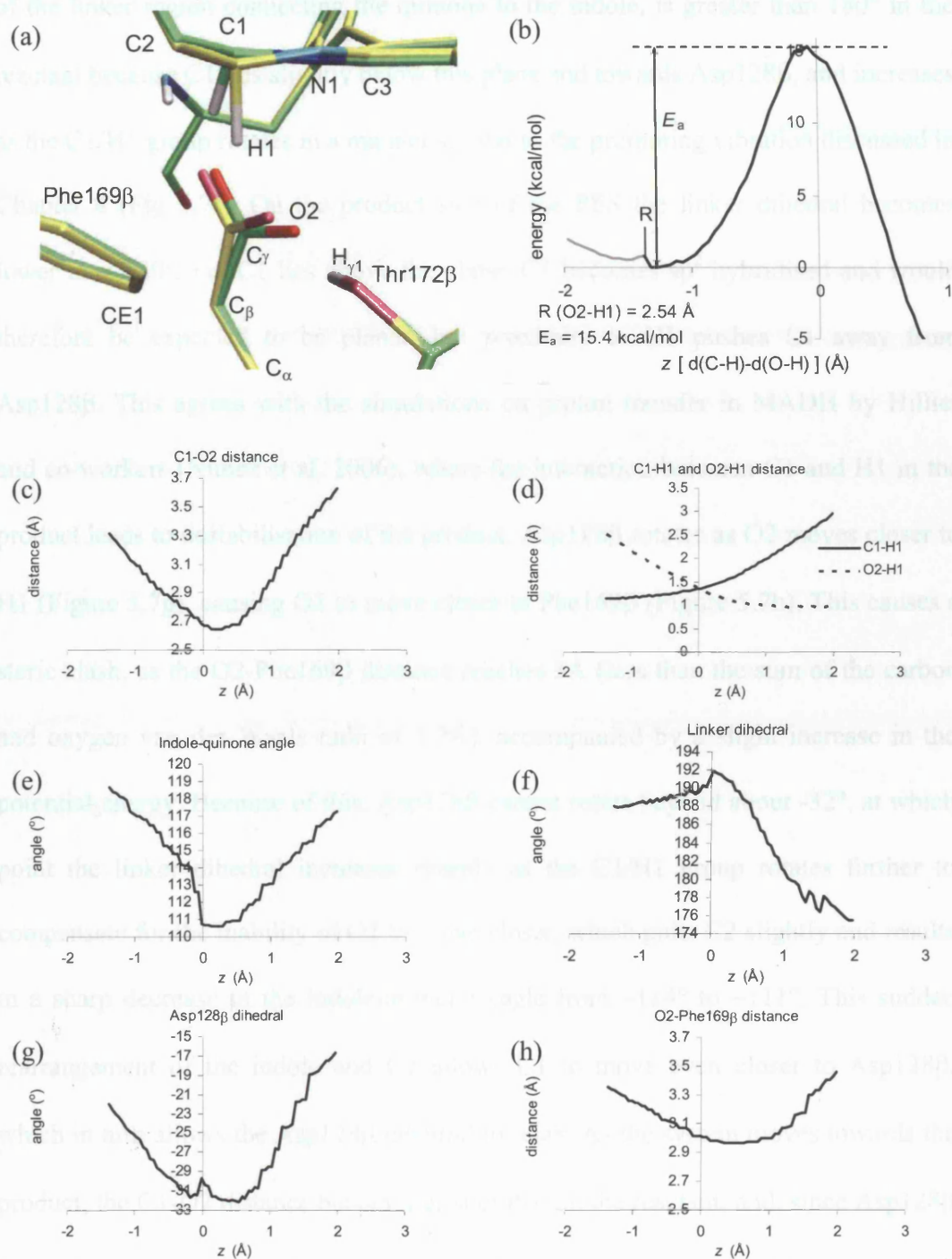
Figure 5.7. Structural changes during proton transfer: (a) reactant (green carbon atoms) structure with maximum potential energy (yellow carbon atoms) (b) potential energy surface and structural changes during proton transfer: (c) C1-O2 distance, (d) C1-H1 / O2-H1 distance, (e) indole-quinone angle, (f) linker dihedral, C3-N1-C1-C2, (g) Asp128β dihedral, O2-Cγ-Cβ-Cα,, (h) O2-Phe169β CE1 distance.

angle decreases by about 8°. The linker dihedral, which is a measure of the planarity of the linker region connecting the quinone to the indole, is greater than 180° in the reactant because C1 lies slightly below this plane and towards Asp128β, and increases as the C1/H1 group rotates in a manner similar to the promoting vibration discussed in Chapter 4 (Fig 5.7f). On the product side of the PES the linker dihedral becomes lower than 180°, i.e. C1 lies above the plane. C1 becomes sp^2 hybridised and would therefore be expected to be planar, but proximity to H1 pushes C1 away from Asp128β. This agrees with the simulations on proton transfer in MADH by Hillier and co-workers (Nunez et al. 2006), where the interaction between C1 and H1 in the product leads to destabilisation of the product. Asp128β rotates as O2 moves closer to H1 (Figure 5.7g), causing O2 to move closer to Phe169β (Figure 5.7h). This causes a steric clash, as the O2-Phe169β distance reaches 3Å (less than the sum of the carbon and oxygen van der Waals radii of 3.2Å), accompanied by a slight increase in the potential energy. Because of this, Asp128β cannot rotate beyond about -32°, at which point the linker dihedral increases sharply as the C1/H1 group rotates further to compensate for the inability of O2 to move closer, which pulls C2 slightly and results in a sharp decrease in the indole-quinone angle from ~114° to ~111°. This sudden rearrangement of the indole and C2 allows C1 to move even closer to Asp128β, which in turn allows the Asp128β dihedral to relax. As the system moves towards the product, the C1-O2 distance becomes greater than in the reactant, and, since Asp128β loses its negative charge as it forms a bond with H1, the O2-Thr172β hydrogen bond is weakened, and the distance between O2 and Thr172β $H_{\gamma 1}$ increases (Figure 5.8).

In the above example, the presence of Phe169β is unfavourable to the proton transfer: a steric clash between Phe169β and O2 causes a sudden increase in the PES. Clearly, it would be beneficial for the reaction if Phe169β could move away from Asp128β during the reaction (the MM region is restrained during these calculations). However, any structural rearrangement required for the proton transfer to occur will increase the potential energy barrier, so Phe169β would in any case reduce the probability of Asp128β achieving its optimal reacting configuration. This raises the question as to the role of Phe169β, the most likely being that it pushes Asp128β so that the C1-O2 distance in the product is greater than in the reactant to prevent the back-reaction. The role of Phe169β will be discussed further in the Section 5.6.
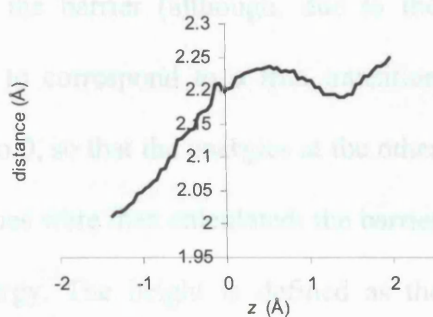
Figure 5.8. O2-Thr172β Hγ$_1$ distance during proton transfer.

To analyse the fluctuations of the PES in more detail, three points were defined (Figure 5.9): the reactant (R) is the MD snapshot with the QM region with the z-value fixed; the reactant minimum (R$_{min}$) is the minimum in the reactant well; the
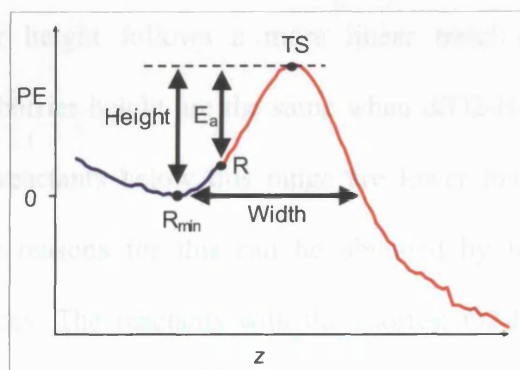
Figure 5.9. Definition of reactant (R), reactant minimum (R$_{min}$), transition state (TS), barrier height and width and activation energy (E$_a$). The red portion of the potential energy surface goes from R towards the product, and the blue portion goes from R to R$_{min}$. The axes are: x, z = d(C-H)-d(O-H) (Å); y, potential energy, PE (kcal/mol)

transition state (TS) is the point at the top of the barrier (although, due to the simplicity of these calculations, this is unlikely to correspond to a true transition state). The energy at the reactant minimum is set to 0, so that the energies at the other points are relative to this. For each PES, three values were then calculated: the barrier height, the barrier width and the activation energy. The height is defined as the potential energy difference between the reactant minimum and the transition state; the width is the difference in z value from the reactant minimum and the point with 0 energy on the product side of the barrier; the activation energy is defined, as the energy difference between the reactant (i.e. the MD snapshot) and the transition state (note that this is an idiosyncratic definition, not that used in the Arrhenius expression).

There is an obvious correlation between the activation energy and the O2-H1 distance (Figure 5.10a): the lowest activation energies are only achieved when H1 is closest to O2, and the activation energies are the highest when H1 and O2 are further apart. However, this is not a linear trend, and the absolute highest activation energies do not correspond to the longest H1-O2 distances. Instead, the plot fits much better to a quadratic curve, since the activation energies for the longest O2-H1 distances are lower than would be expected from a linear trend, as are those for the shortest O2-H1 distances. The barrier height follows a more linear trend (Figure 5.10b). The activation energy and barrier height are the same when d(O2-H1) > ~2.2 Å, and the activation energy for reactants below this range are lower than the barrier height. Some insight into the reasons for this can be obtained by looking at individual potential energy surfaces. The reactants with the shortest O2-H1 distances (Figure 5.11a,b,c) lie part-way up the potential energy barrier, with a z value closer to 0 than the reactant minimum, which results in a further reduction in activation energy
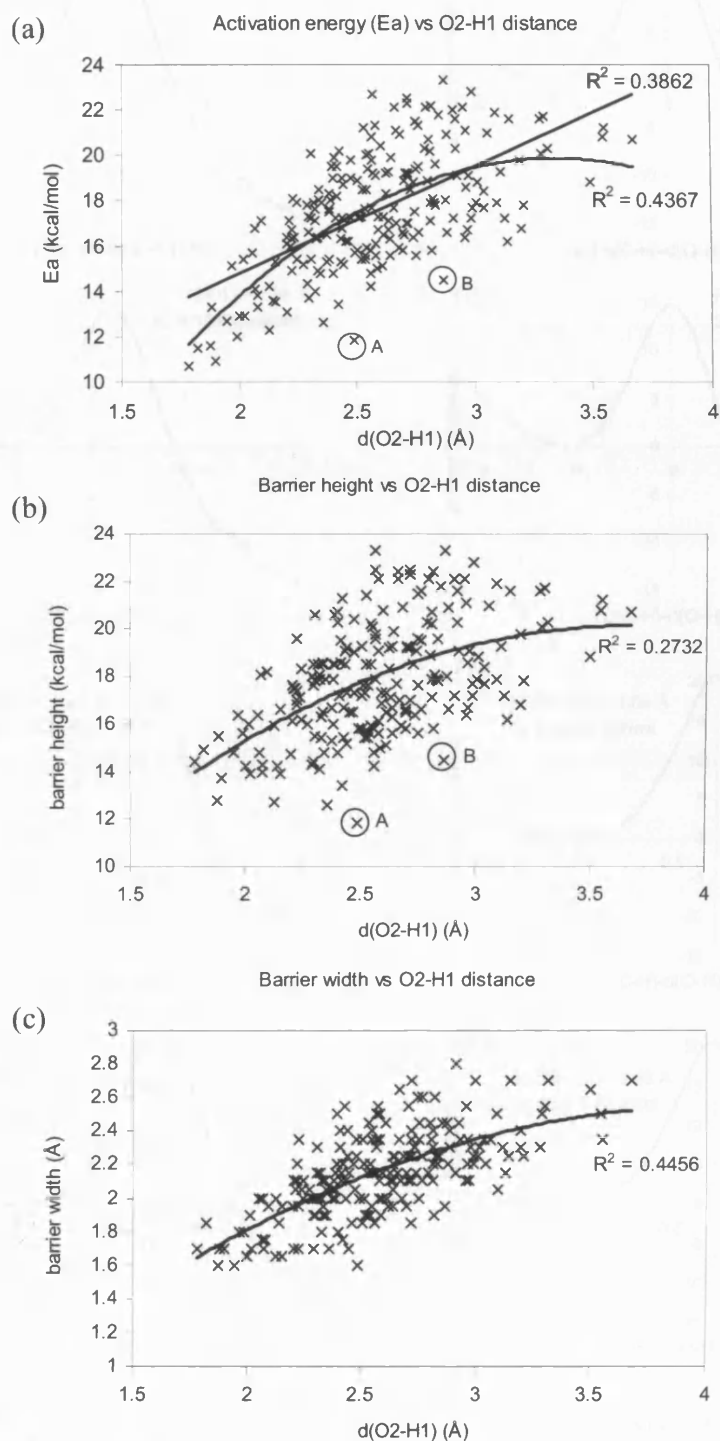
Figure 5.10. Activation energy (a), barrier height (b) and barrier width (c) against O2-H1 distance.
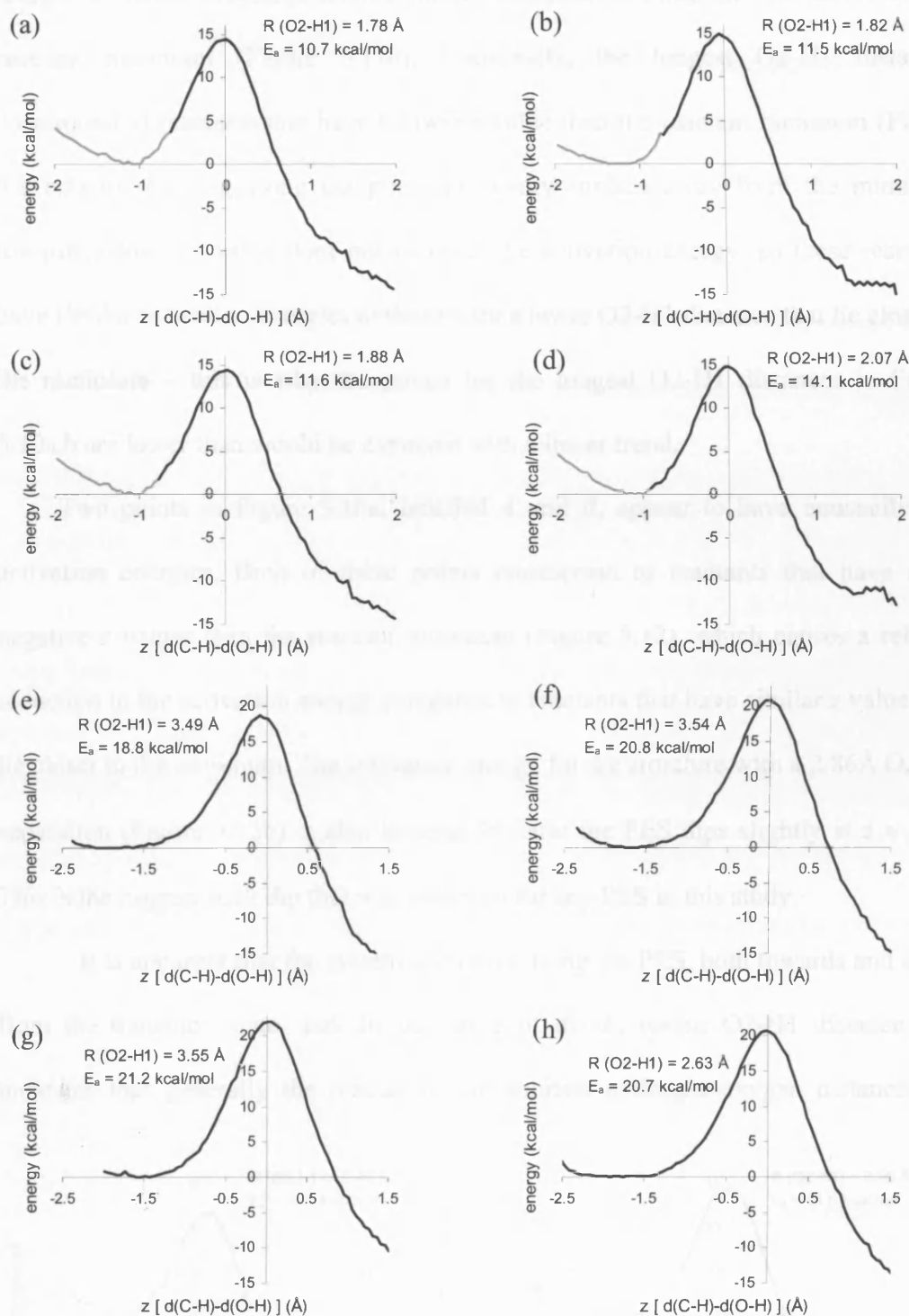
Figure 5.11. Selected potential energy surfaces. The reactant is the point where the black and grey lines meet, the black line representing the system moving towards the transition state, the grey line away from the transition state. O2-H1 distance and activation energies (E_a) are given in Å and kcal/mol. (a,b,c) have the shortest O2-H1 distances, while (e,f,g,h) have the longest. (d) is shown for comparative purposes: even though (d) has a similar minimum z and barrier height to (a,b,c) it has a higher activation energy E_a.

relative to those structures with a similar minimum z value that lie closer to the reactant minimum (Figure 5.11d). Conversely, the longest O2-H1 distances correspond to reactants that have a lower z value than the reactant minimum (Figure 5.11e,f,g,h). Moving along the potential energy surface away from the minimum towards a lower z value does not increase the activation energy, so these reactants have similar activation energies to those with a lower O2-H1 distance that lie closer to the minimum – this is why the points for the longest O2-H1 distances in Figure 5.10a,b are lower than would be expected with a linear trend.

Two points in Figure 5.10a, labelled A and B, appear to have unusually low activation energies. Both of these points correspond to reactants that have more negative z values than the reactant minimum (Figure 5.12), which causes a relative reduction in the activation energy compared to reactants that have similar z values but lie closer to the minimum. The activation energy for the structure with a 2.86Å O2-H1 separation (Figure 5.12b) is also lowered because the PES dips slightly at $z \approx$ -0.2. This is the biggest such dip that was observed for any PES in this study.

It is apparent that the system can move along the PES, both towards and away from the transition state, and the curvature of the E_a versus O2-H1 distance plot indicates that generally the reactants with shortest hydrogen-oxygen distances lie
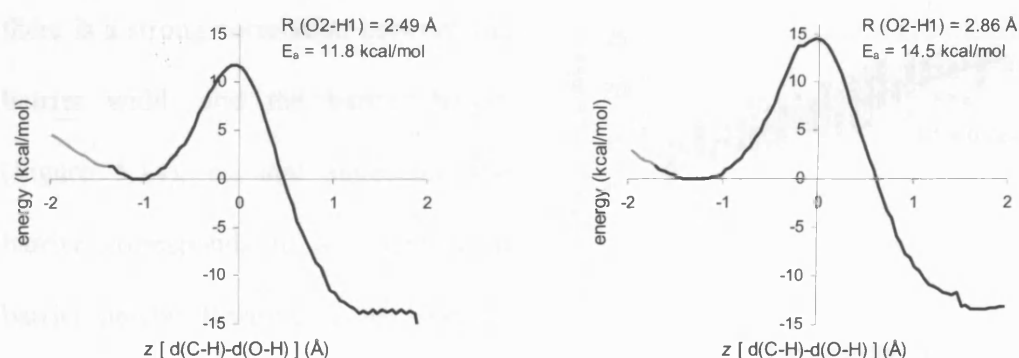
Figure 5.12. Potential energy surfaces with unusually low activation energy for the reactant O2-H1 distance. The reactant is the point where the solid and dotted lines meet, the solid line representing the system moving towards the transition state, the dotted line away from the transition state.
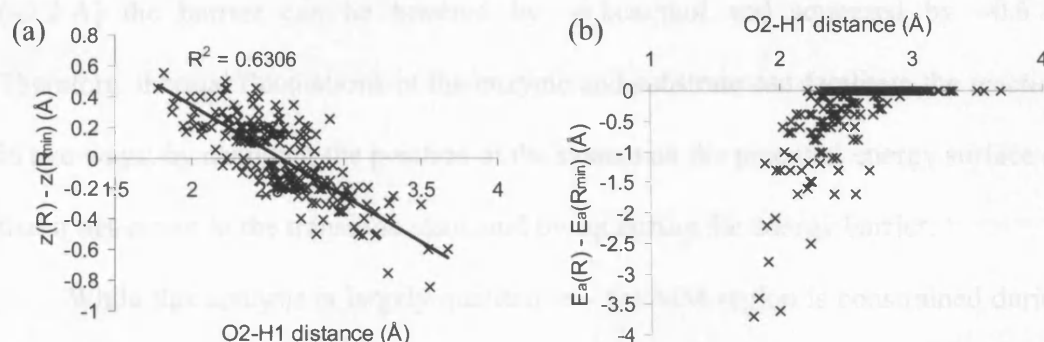
Figure 5.13. The difference in (a) z values and (b) activation energies between the reactant (R) and reactant minimum (R_{min}) *versus* the O2-H1 distance of the reactant.

closer to the transition state, while those with the longest hydrogen-oxygen distances lie further from it. This trend is obvious from the plot of the difference in z values between the reactant and reactant minimum *versus* reactant O2-H1 distance (Figure 5.13a). Very few reactants actually correspond to the reactant minimum, with most lying further than the minimum from the transition state. The activation energy can be reduced by ~ 3-4 kcal/mol by this thermal fluctuation along the PES (Figure 5.13b).

Thermal fluctuations can therefore reduce the activation energy, and also the distance the proton needs to tunnel through the barrier, by moving the system along the potential energy surface. The activation energy and tunneling distance can also be reduced by squeezing the barrier: there is a correlation between the O2-H1 distance and the barrier width (Figure 5.10c): reactants with the shortest O2-H1 distances tend to have narrower barriers. Furthermore, there is a strong correlation between the barrier width and the barrier height (Figure 5.14), so that squeezing the barrier corresponds to a reduction in barrier height. Relative to the average barrier height (~18 kcal/mol) and width
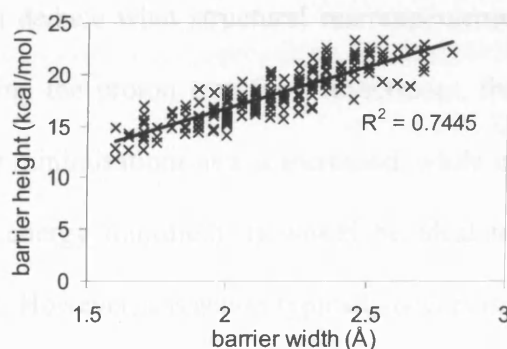
Figure 5.14. Barrier height *versus* barrier width.

(~2.2 Å) the barrier can be lowered by ~6 kcal/mol and squeezed by ~0.6 Å. Therefore, thermal fluctuations of the enzyme and substrate can facilitate the reaction in two ways: by changing the position of the system on the potential energy surface so that it lies closer to the transition state, and by squeezing the energy barrier.

While this analysis is largely qualitative – the MM region is constrained during the calculation of the PES, which causes the height of the potential energy surface to be overestimated – it does show that reducing the hydrogen-acceptor distance is sufficient to effectively reduce the activation energy and the barrier width, and therefore promote both proton transfer by a classical over-the-barrier route and by tunneling. The C1/H1 rotation and repositioning of O2 that occur as the system is pushed along the PES (Figure 5.7) corresponds to the promoting vibration identified in Chapter 4. Thus, the mechanism by which this vibration promotes proton transfer has been identified

5.4. MD simulations initiated at the transition state

The PES calculated in Section 5.2 give important insight into how the structure of the enzyme and substrate affect the proton transfer reaction; in particular they revealed that reducing the H1-O2 distance is key to reducing the activation energy. However, from these calculations it is not possible to deduce what structural rearrangements, beyond those in the QM region, occur during the proton transfer. Furthermore, the PESs are calculated from consecutive energy minimisations as z is increased, while in reality a reaction does not occur from an energy minimum. It would be ideal to observe a reaction during the MD simulation. However, a reaction typically occurs on the millisecond timescale – in this case just below the millisecond timescale as the rate is ~3500 s^{-1} (Masgrau et al. 2006)– and is therefore too rare an event to be

observed from standard MD simulations. Therefore, MD simulations were initiated at a putative transition state and propagated backwards and forwards in time: combining the two trajectories gives one trajectory which passes through this putative transition state. This method has previously proved useful for identifying promoting motions in dihydrofolate reductase (Agarwal *et al.* 2002b).

To initiate these simulations, QM/MM MD simulations of the transition state were first produced: every 20 ps, a "spin-off" trajectory was run from the 200 ps QM/MM MD simulation described in Section 5.2, where the system was dragged towards a putative transition state, defined as z = -0.05 Å (the top of the PES lies, on average at about z = -0.05), by decreasing z by 0.05 Å every 1 ps using a harmonic restraint of 1000 kcal/mol/Å^2. Once z = -0.05 Å was reached, a 20 ps trajectory was created where z was restrained at -0.05 Å using a force constant of 750 kcal/mol/Å^2. The reason for a force constant one order of magnitude lower than the 5000 kcal/mol/Å^2 used for the PES calculations is that as the system moves through the transition state the proton needs some velocity along the C1-H1 and O2-H1 vectors, and C1 and O2 need velocity along their interatomic axis; a high force constant does not allow this.

The reason for producing separate 20 ps transition state MD simulations rather than just one is that the transition state is, by definition, strained and statistically unlikely: running the simulation with an enforced transition state allows the system to adapt to it and alleviate some of this strain, which can alter the structure of the transition state. Furthermore, as is be discussed in Section 5.6, the conformation of Phe169β was found to alter significantly during the transition state simulations, so it was restrained using a weak harmonic constraint of 1 kcal/mol/degree^2 on the C-C$_\alpha$-C$_\beta$-C$_\gamma$ dihedral, which measures the side chain orientation relative to the backbone,

and a restraint of 3 kcal/mol/Å^2 on the distance between O2 and the nearest Phe169β atom.

Unrestrained MD simulations (i.e. without any restraints on z) were initiated every 1 ps from the transition state simulations, and run for 1 ps both forwards and backwards in time. The latter was achieved by reversing the velocities of all the atoms – for time reversible deterministic dynamics, integrating forward in time with inverted velocities is equivalent to running the simulation backward in time (Basner and Schwartz 2005). By merging the two trajectories, a single trajectory that passes through the putative transition state is obtained. About half of the resulting trajectories started and finished in the same well, but 50 so-called reactive trajectories, which start at the reactant and finish at the product, were obtained. Structural rearrangements during these trajectories were measured and averaged, and their respective standard deviations were calculated; the standard deviations can be used to determine the statistical significance of the observed structural changes.

The picture that emerges from these simulations is this (Figure 5.15): heavy atom motion dominates until the donor C1 and acceptor O2 have approached to a distance of about 2.7 Å, which agrees with the distance at which tunneling is maximised in the VTST/MT calculations (Masgrau et al. 2006), at which point proton motion dominates (Figure 5.15a,d and Figure 5.16). Once the proton has transferred to O2 the system relaxes as C1 and O2 move apart. The point at which the C1-O2 distance reaches its minimum coincides with the point when C1-H1 begins stretching (Figure 5.15d and 5.16), and the C1-O2 distance begins increasing again once the O2-H1 bond is formed. The proton transfer event itself occurs from $z \approx -0.32$ to $z \approx 0.65$, during which time the proton moves ~0.49 Å, which is slightly lower than the TST/MT result where the proton tunnels ~0.59 Å to O2 (Masgrau et al. 2006).
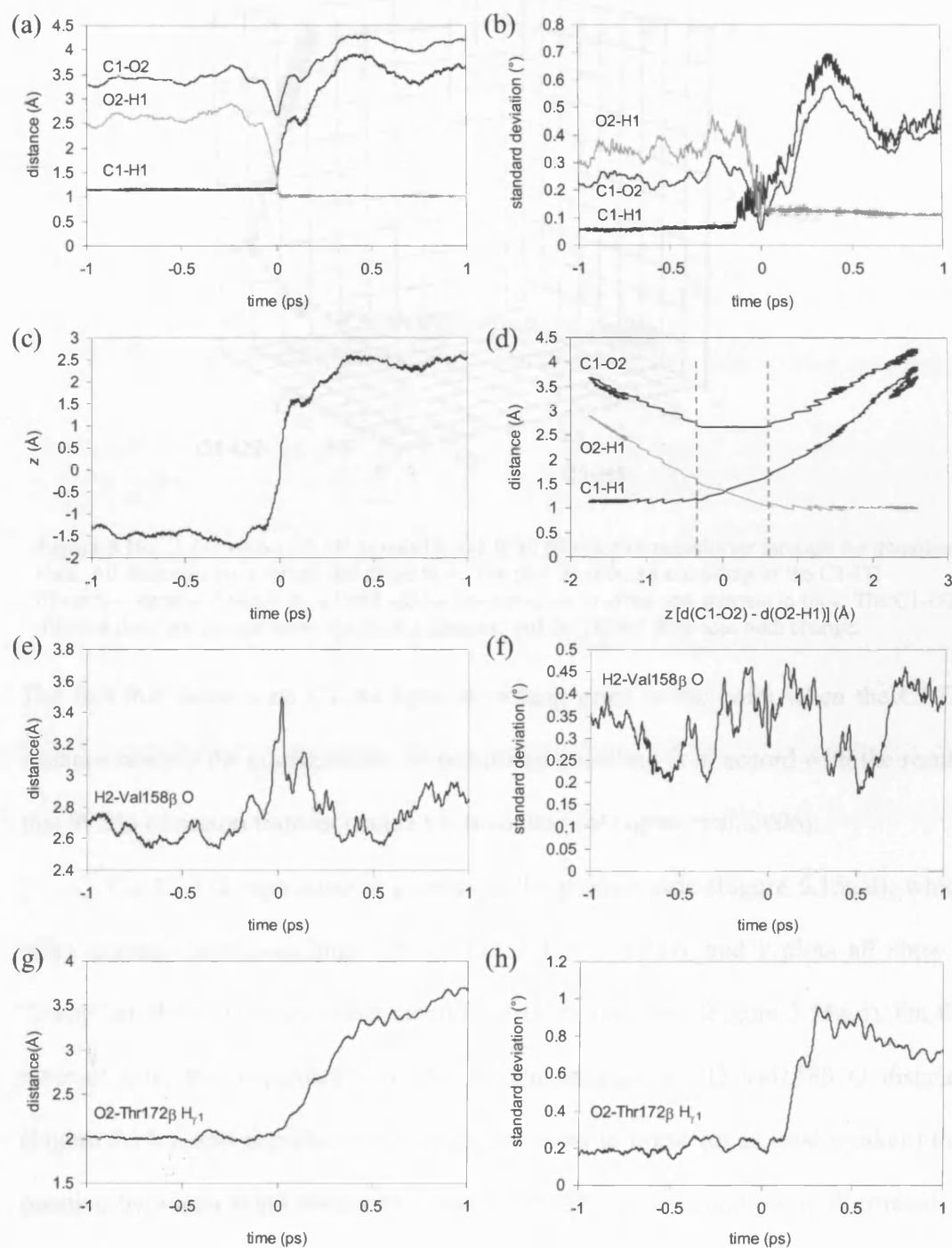
Figure 5.15. Average structural changes and standard deviations from 50 2ps AM1/MD simulations through the transition state.
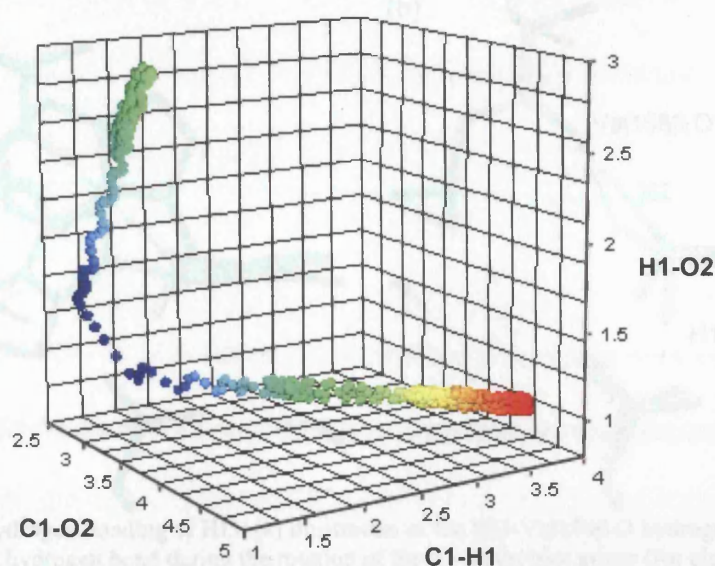
Figure 5.16. C1-O2 *versus* C1-H1 *versus* H1-O2 from 50 reactive trajectories through the transition state. All distances are average and given in Å. The plot is coloured according to the C1-O2 distance – longest distance in red and yellow, intermediate in green and shortest in blue. The C1-O2 distance does not change when the C1-H1 distance and the O2-H1 distances both change.

The fact that there is no C1-H1 bond stretching prior to the point when the C1-O2 distance reaches the configuration of maximum tunneling is in accord with the results that 99.9% of proton transfer occurs via tunneling (Masgrau et al. 2006).

The C1-O2 separation is greater on the product side (Figure 5.15a,d), which helps prevent back-tunneling. The C1-O2, C1-H1, O2-H1 and z plots all show a "hump" at about 0.1ps on either side of the transition state (Figure 5.15a,d). On the reactant side, this coincides with the sudden increase in H2-Val158β O distance (Figure 5.15e), and is probably caused by the need to break (or at least weaken) this putative hydrogen bond during the rotation of the C1/H1 group, as is illustrated in Figure 5.17. On the product side the "hump" is accompanied by the breaking of the hydrogen bond between O2 and the Thr172β hydroxyl proton, $H_{\gamma 1}$ – there is a sudden increase in both the distance and standard deviation for the O2-Thr172β $H_{\gamma 1}$ distance at ~0.1ps (Figure 5.15g,h).

(a)   (b)

Val158β O

H2

H1
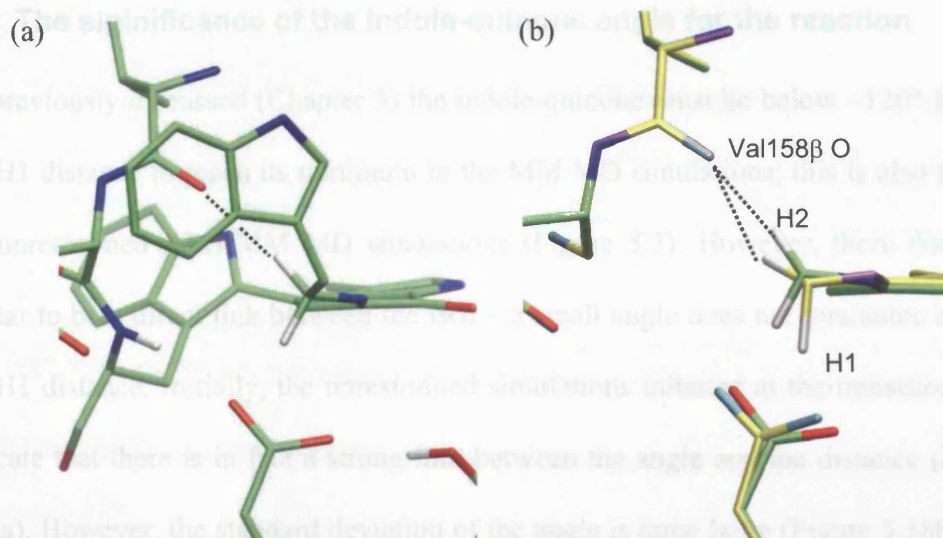
Figure 5.17. Hydrogen bonding of HI3: (a) illustration of the HI3-Val158β O hydrogen bond; (b) breaking of this hydrogen bond during the rotation of the C1 methylene group (for clarity, the indole is not shown). The values for the H-bond distance and the C1-H1-O angle are 2.5 Å and 172° for the minimum energy structure (green carbon atoms) and 2.8 Å and 154° for the structure after rotation of the C1 methylene group (yellow carbon atoms).

As for the proton transfer discussed in Section 5.3, the linker dihedral (the dihedral angle which describes the planarity of the region linking the quinone and the indole – see Figure 5.7) is greater than 180° in the reactant, increases as the system moves to the transition state, then decreases when the product is formed (Figure 5.18). Initially, the dihedral decreases to about 175°, which is about the same as the minimum value at $z = 2$ in the proton transfer discussed in Section 5.3. Here, however, the linker dihedral then settles at about 180°, as the C1-O2 distance increases above the maximum of ~3.6 Å in the previously discussed proton transfer, and the increased distance between C1 and H1 now allows C1 to move in-plane with the quinone. Therefore, as the O2-Thr172β $H_{\gamma 1}$ hydrogen bond breaks, O2 can move away from C1, which allows the linker region to become more planar. Again, this agrees with the results of Hillier and co-workers which suggests that product stabilisation in MADH requires that Asp128β moves away from C1 (Nunez et al. 2006).

149

5.5. The siginificance of the indole-quinone angle for the reaction

As previously discussed (Chapter 3) the indole-quinone must be below ~120° for the O2-H1 distance to reach its minimum in the MM MD simulations; this is also true in the unrestrained AM1/MM MD simulations (Figure 5.3). However, there does not appear to be a direct link between the two – a small angle does not guarantee a short O2-H1 distance. Initially, the unrestrained simulations initiated at the transition state indicate that there is in fact a strong link between the angle and the distance (Figure 5.18a). However, the standard deviation of the angle is quite large (Figure 5.18b), and not much lower than the ~10° decrease in the angle from the reactant to transition state, and many of the reactive trajectories do not show a strong decrease in the indole-quinone angle (e.g. Figure 5.18c,d). Furthermore, the average indole-quinone angle at the transition state is ~106°, which is visited frequently during the unrestrained AM1/MM simulations of the reactant (Figure 5.3), while the C1/H1-O2 distances in those simulations never get close to the transition state values. Therefore, while achieving a low O2-H1 distance does require the indole-quinone angle to lie below ~120° (Figure 5.3. and 5.18a,b), the angle does not appear to be coupled to the reaction. Furthermore, the correlation between the activation energy and the indole-quinone angle (Figure 5.19) is far weaker than that between the activation energy and the O2-H1 distance (Figure 5.10a). Using multiple linear regression for activation energy *versus* both O2-H1 distance and indole-quinone angle gives an R^2 value identical to 4 significant figures to the linear regression for activation energy *versus* O2-H1 distance (0.38615 and 0.38623 respectively) which means that the indole-quinone angle does not directly affect the activation energy.
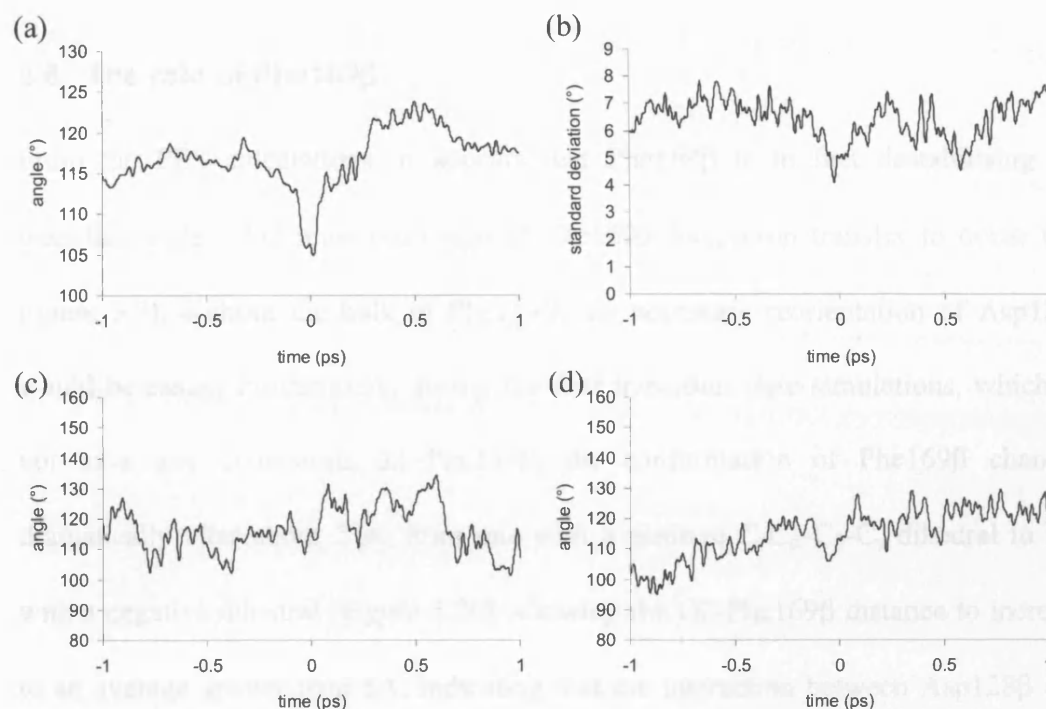
Figure 5.18. Indole-quinone angle from unrestrained MD simulations initiated at the transition state: (a) average indole-quinone angle and (b) its standard deviation from 50 2ps AM1/MD simulations through the transition state; (c,) indole-quinone angle for two individual trajectories.
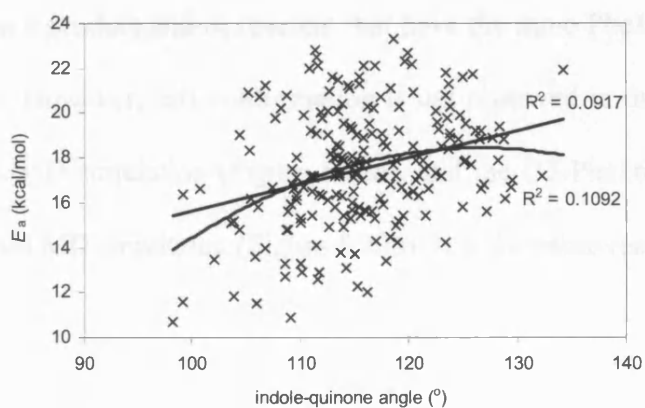
Figure 5.19. Activation energy *versus* indole-quinone angle.

5.6. The role of Phe169β

From the PES calculations, it appears that Phe169β is in fact destabilising the transition state – O2 must push against Phe169β for proton transfer to occur (see Figure 5.7); without the bulk of Phe169β, the necessary reorientation of Asp128β would be easier. Furthermore, during the first transition state simulations, which do not have any constraints on Phe169β, the conformation of Phe169β changed dramatically after about 2 ps, from one with a positive $C-C_\alpha-C_\beta-C_\gamma$ dihedral to one with a negative dihedral (Figure 5.20), allowing the O2-Phe169β distance to increase to an average greater than 5Å, indicating that the interaction between Asp128β and Phe169β is unfavourable in the transition state. Running the dynamics forwards and backwards in time from a transition state with this alternate Phe169β conformation usually results in a product and/or reactant that have the same Phe169β conformation (Figure 5.21a,c). However, this conformation is not observed in the crystal structure or in the 200 ps MD simulation (Figure 5.22a), and the O2-Phe169β distance never reaches 5Å in said MD simulation (Figure 5.22b). It is therefore reasonable to assume
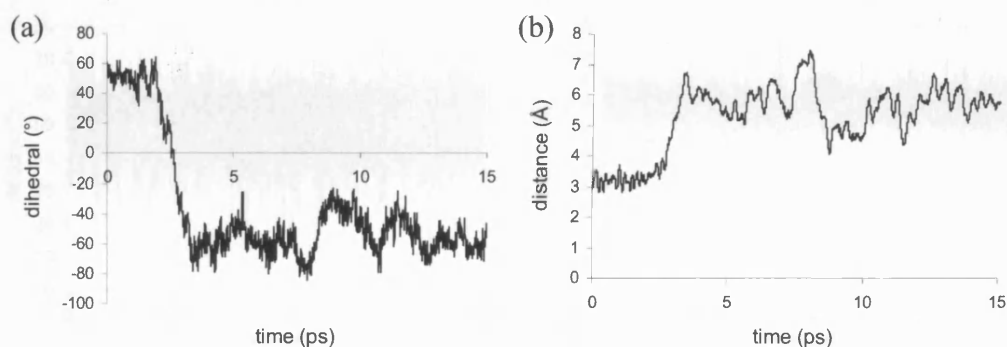
Figure 5.20. Change in Phe169β conformation during a 15 ps MD simulation of the transition state: (a) the $C-C_\alpha-C_\beta-C_\gamma$ dihedral angle which represents the sidechain orientation relative to the backbone and (b) the O2-Phe169β CE1 (see Figure 5.7 for atom label) distance.

that this conformation does not occur naturally but is instead an artefact of the simulation. Therefore, subsequent simulations of the transition state were run with the previously mentioned restraints applied to Phe169β (Section 5.4).

In the trajectories where Phe169β adopts the alternate conformation (with a negative $C-C_\alpha-C_\beta-C_\gamma$ dihedral), the hydrogen bond between O2 and Thr172β is not
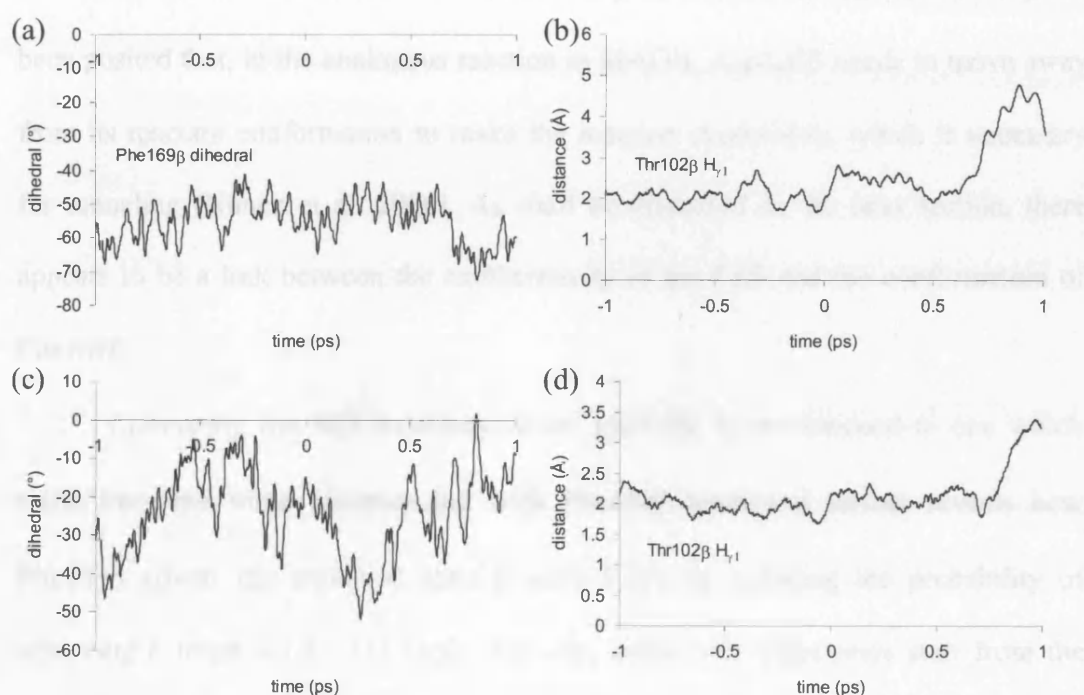
Figure 5.21. (a,c) Phe169β $C-C_\alpha-C_\beta-C_\gamma$ dihedral angles for two 2 ps AM1/MM MD simulations through the transition state, and (b,d) the corresponding O2-Thr172H$_{\gamma1}$ distances.
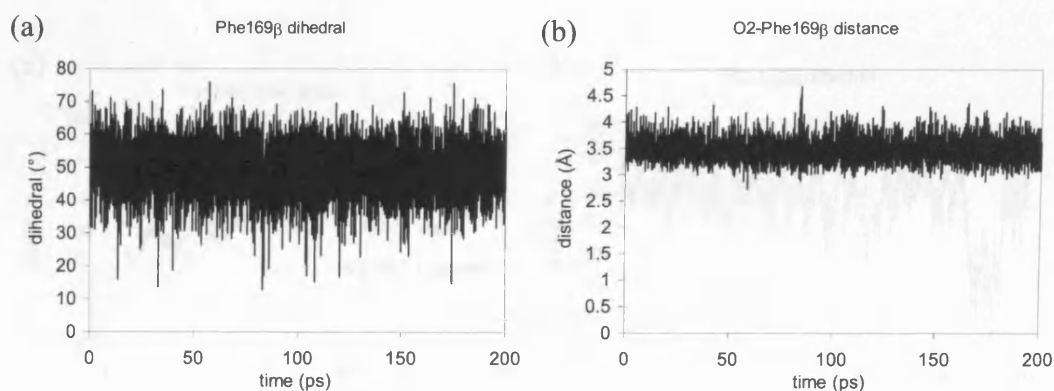
Figure 5.22. O2-Phe169β CE1 distance (see Figure 5.7 for atom label) and Phe169β $C-C_\alpha-C_\beta-C_\gamma$ dihedral during the 200 ps AM1/M MD simulation of the tryptiminoquinone.

broken as quickly in the product as it is in the other trajectories (Figure 5.21b,d), although it is eventually broken, which is facilitated by the formation of the O2-H1 bond which renders O2 less negative. It therefore appears that the force of Phe169β pushing against O2 is required to ensure that the hydrogen bond is broken quickly. Breaking this hydrogen bond will further strengthen the O2-H1 bond and allow O2 to move further from C1, and therefore reduce the probability of the back-reaction. It has been posited that, in the analogous reaction in MADH, Asp128β needs to move away from its reactant conformation to make the reaction exothermic, which is necessary for tunneling (Nunez et al. 2006). As shall be discussed in the next section, there appears to be a link between the exothermicity of the PES and the conformation of Phe169β.

Comparing the MD trajectory where Phe169β is unrestrained to one which starts from the same structure but with Phe169β restrained further reveals how Phe169β affects the transition state (Figure 5.23), by reducing the probability of achieving a linear C1-H1-O2 angle. Initially, since both trajectories start from the same structure and the same velocities, the C1-H1-O2 angles are very similar, but start to diverge after about 2 ps (Figure 5.23a), when the unrestrained Phe169β

(a)

C1-H1-O2 angle

(b)
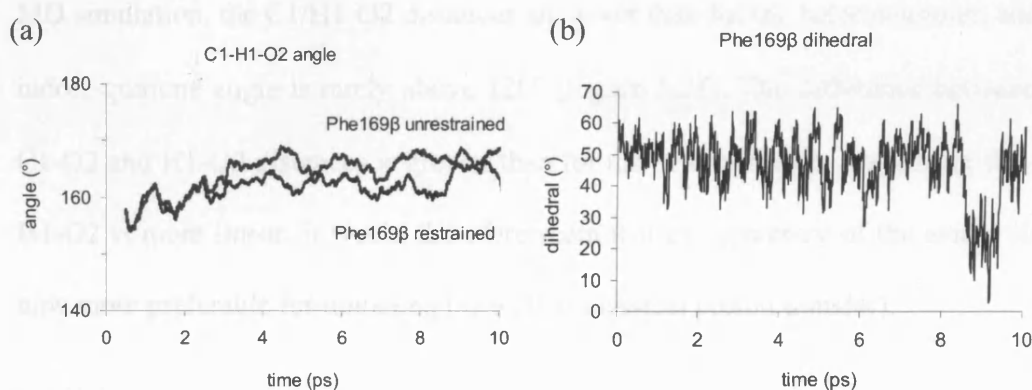
Phe169β dihedral

Figure 5.23. Effect of Phe169β conformation on C1-H1-O2 angle: (a) C1-H1-O2 angle (running average over consecutive 0.5ps windows), (b) Phe169β $C-C_\alpha-C_\beta-C_\gamma$ dihedral during AM1/MM MD simulation of the transition state ($z \approx -0.05$).

changes conformation (Figure 5.20a). The unrestrained Phe169β then allows a C1-H1-O2 angle closer to 180° to be achieved, which facilitates proton transfer. At about 9 ps the average angle for the restrained Phe169β temporarily increases, which coincides with a drop in the Phe169β dihedral: as Phe169β pushes less against Asp128β, a higher C1-H1-O2 angle can be achieved.

5.7. QM/MM MD simulations and PES calculations of the AADH β monomer

As mentioned in Section 3.6, the isolated β monomer in solution is catalytically active, but three orders of magnitude slower than the $\alpha_2\beta_2$ heterotetramer, with a much reduced degree of tunneling[1]. The most intuitive explanation would be that, with a solvent exposed active site, H1 and O2 are not held close enough for effective proton transfer to take place. However, MM MD simulations suggested that quite the opposite was true: the H1-O2 distances are slightly shorter than in the heterotetramer (see Chapter 3). To try to reconcile this observation with the kinetic data, a 200 ps AM1/MM MD simulation was run, started after 5 ns of MM MD simulations (see Section 3.6), using the same protocol as for the $\alpha_2\beta_2$ heterotetramer. As for the MM MD simulation, the C1/H1-O2 distances are lower than for the heterotetramer, and the indole-quinone angle is rarely above 120° (Figure 5.24). The difference between the C1-O2 and H1-O2 distances is greater than for the heterotetramer, indicating that C1-H1-O2 is more linear. It would therefore seem that the geometry of the active site is now more preferable for tunneling (as well as classical proton transfer).

---

[1] Personal communication with Nigel S. Scrutton and Parvinder Hothi; work in progress.
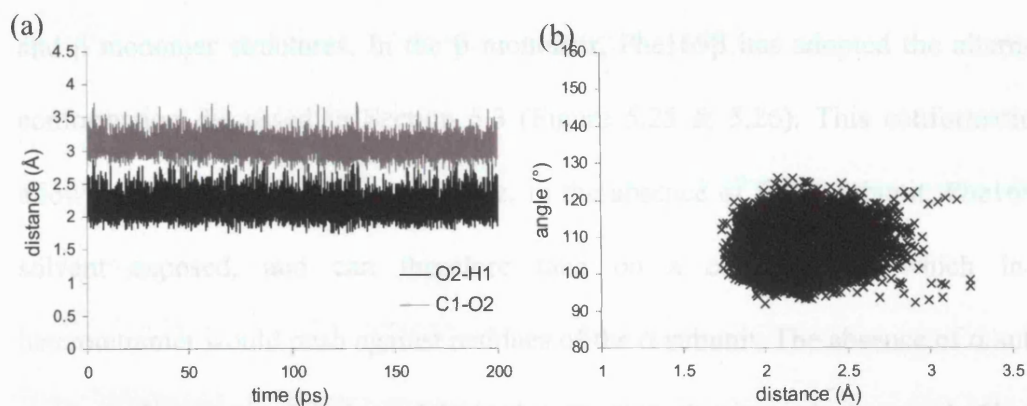
Figure 5.24. (a) C1/H1-O2 distance *versus* time and (b) indole-quinone angle *versus* O2-H1 distance during a 200ps AM1/MM MD simulation of the β monomer.
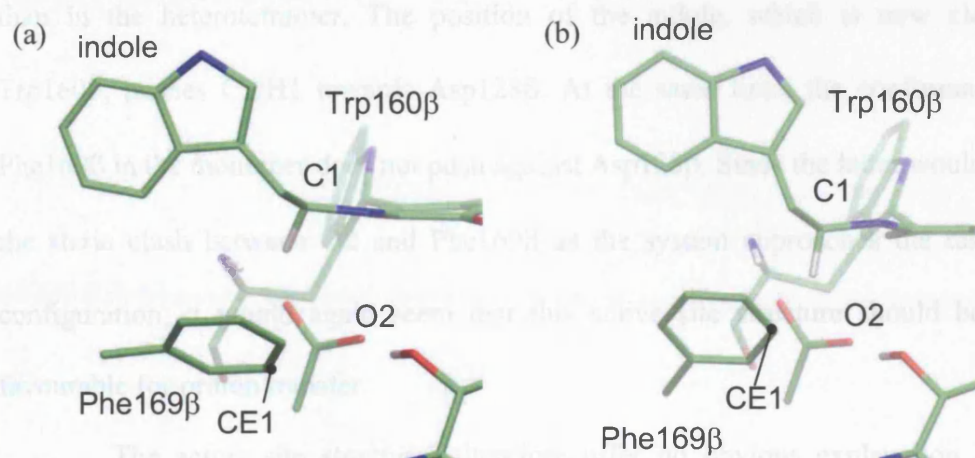
Figure 5.25. Active site of AM1/MM minimised AADH and iminoquinone: (a) *A,H* active site from the $\alpha_2\beta_2$ heterotetramer; (b) isolated β monomer active site.
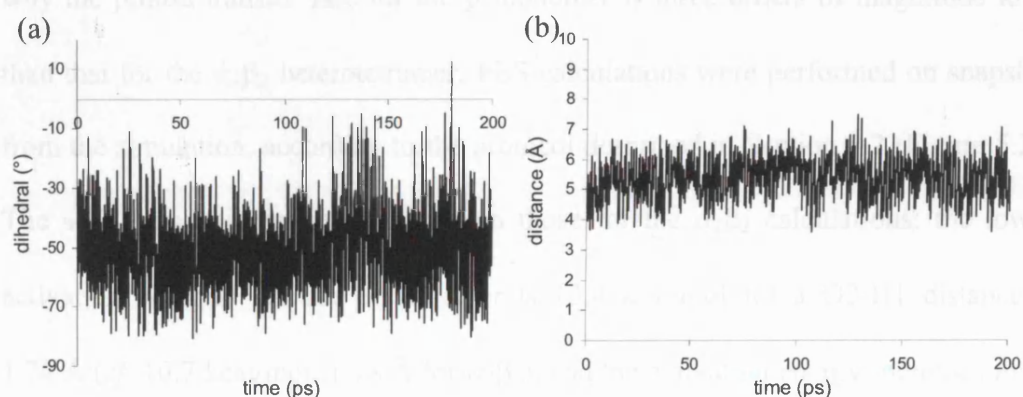
Figure 5.26. (a) Phe169β dihedral and (b) O2-Phe169β CE1 distance during the 200ps AM1/MM MD simulation of the β monomer.

Figure 5.25 compares the active sites in the energy minimised heterotetramer and β monomer structures. In the β monomer, Phe169β has adopted the alternative conformation discussed in Section 5.3 (Figure 5.25 & 5.26). This conformation is allowed during this simulation because, in the absence of the α subunit, Phe169β is solvent exposed, and can therefore take on a conformation which in the heterotetramer would push against residues of the α subunit. The absence of α subunit residues also means that the indole in the monomer is not pushed towards Phe169β and away from Trp160β, so that the indole-quinone angle can achieve lower values than in the heterotetramer. The position of the indole, which is now closer to Trp160β, pushes C1/H1 towards Asp128β. At the same time, the conformation of Phe169β in the monomer does not push against Asp128β. Since the latter would avoid the steric clash between O2 and Phe169β as the system approaches the tunneling configuration, it would again seem that this active site structure should be more favourable for proton transfer.

The active site structures therefore offer no obvious explanation for the considerable reduction in proton transfer rate in the β monomer. To gain insight into why the proton transfer rate for the β monomer is three orders of magnitude lower than that for the $\alpha_2\beta_2$ heterotetramer, PES calculations were performed on snapshots from the simulation, according to the protocol described in Section 5.2 (Figure 5.27). The activation energies are higher than those for the $\alpha_2\beta_2$ calculations: the lowest activation energies for the β monomer is 13.4 kcal/mol for a O2-H1 distance of 1.74 Å (*cf.* 10.7 kcal/mol, 1.78 Å for $\alpha_2\beta_2$), and the activation energy increases much faster with the O2-H1 distance. Furthermore, the correlation between the activation energy and O2-H1 distance is linear, suggesting that there is less motion along the

PES than in the heterotetramer where the activation energies follow a curved trend. And indeed, the differences between the z values and activation energies for the reactant and reactant minimum (Figure 5.27b,c) are far less pronounced than for the heterotetramer (Figure 5.13): the z value is never more than 0.25/0.2 Å closer to/further from the transition state than the reactant minimum, and the activation energy can be reduced by less than 2 kcal/mol. This indicates that the reactant well is very narrow, i.e. that more energy is required to move away from the minimum, which agrees with the smaller spread of C1/H1-O2 distances observed in the MD simulation of the reactant.
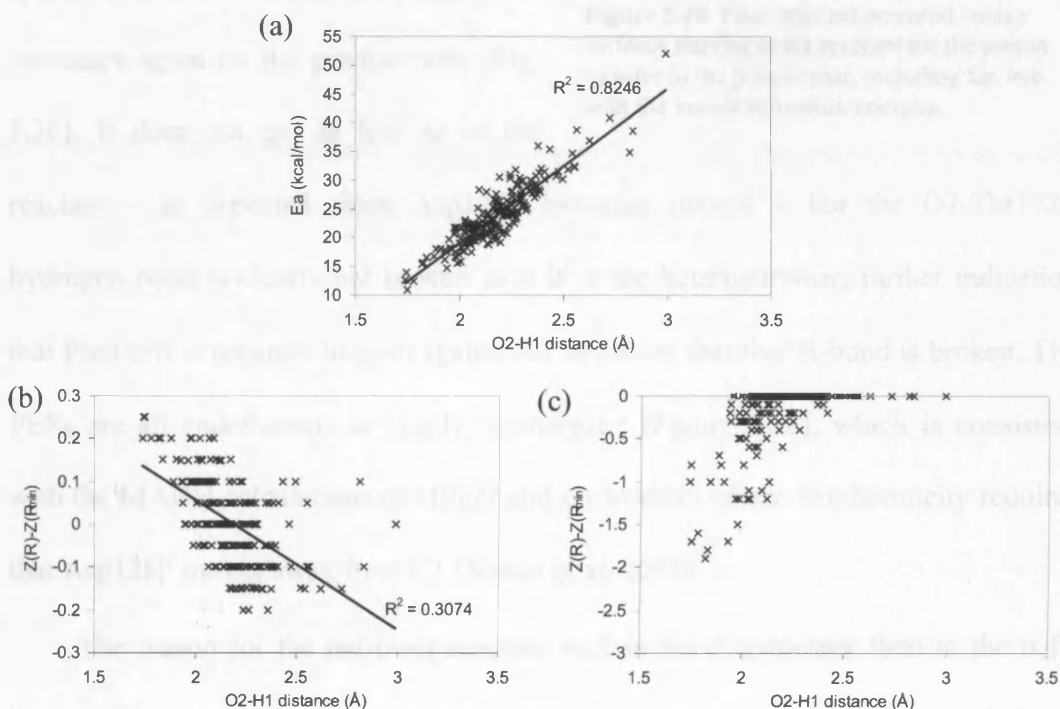
Figure 5.27. (a) Activation energy *versus* O2-H1 distance and the difference in (b) z values and (c) activation energies between the reactant (R) and reactant minimum (R_{min}) *versus* the O2-H1 distance.

Looking at individual PESs confirms that the reactant well is narrower than was observed for the heterotetramer (Figure 5.28 *cf* Figure 5.6), so that it is more difficult for the system to move along the PES. As the system moves along the PES towards the transition state the C1-O2 distance decrease to about 2.7Å (Figure 5.29), but this is accompanied by less structural rearrangement of the iminoquinone than in the heterotetramer, the indole-quinone angle and the linker dihedral both changing by less than 1°. The O2-Thr172β distance increases as the system approaches the transition state, but then decreases again on the product side (Fig. 5.30). It does not get as low as in the

Figure 5.28. Four selected potential energy surfaces starting at the reactant for the proton transfer in the β monomer, including the two with the lowest activation energies.

reactant – as expected since Asp128β becomes neutral – but the O2-Thr172β hydrogen bond is clearly not broken as it is in the heterotetramer, further indicating that Phe169β is required to push against O2 to ensure that this H-bond is broken. The PESs are all endothermic or nearly isoenergetic (Figure 5.28), which is consistent with the MADH calculations of Hillier and co-workers where exothermicity requires that Asp128β moves away from C1 (Nunez et al. 2006).

The reason for the narrower reactant well in the β monomer than in the $\alpha_2\beta_2$ hetererotetramer can be seen by comparing the reactant for the PES discussed above to the reactant for the PES discussed in Section 5.3 (Figure 5.31). In the heterotetramer structure the C1/H1 group can rotate towards O2, so that C1-H1-O2 becomes more linear. This corresponds to the main vibration of the C1/H1 group,

Figure 5.29. Structural changes during proton transfer in the β monomer: (a) Reactant, green carbon atoms, and transition state, yellow carbon atoms, (b) potential energy surface and structural changes during proton transfer: (c) C1-O2 distance, (d) C1-H1 / O2-H1 distance, (e) indole-quinone angle, (f) linker dihedral, C3-N1-C1-C2, (g) Asp128β dihedral, O2-Cγ-Cβ-Cα,, (h) O2-Phe169β CE1distance.

which is also coupled to the motion of O2 required to achieve tunneling (Chapter 4). Thus, the promoting vibration pushes the system towards the transition state along the PES. In the β monomer, however, the position of the indole forces C1 towards Asp128β
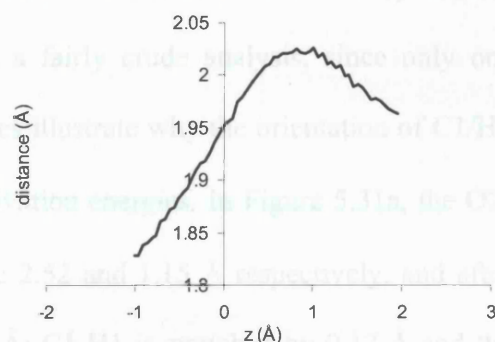
Figure 5.30. O2-Thr172b Hg1 distance during proton transfer in the β monomer

(Figure 5.25b). The result is that the C1/H1 orientation in the reactant is similar to that

after rotation of the C1/H1 group in the heterotetramer, and further rotation of C1/H1

becomes more difficult and would not bring C1/H1 closer to O2. Furthermore, the

motion of O2 in the promoting vibration is coupled to the motion of H1 (Chapter 4),

so, while the required repositioning of O2 is still possible, it will be less likely to be

coupled to the reaction coordinate.

Comparing this β monomer reactant to the heterotetramer reactant before and
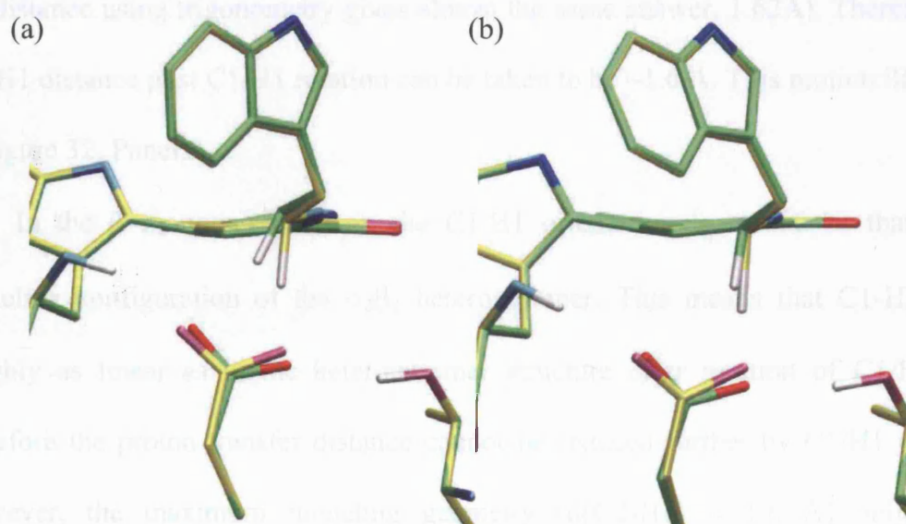
Figure 5.31. Reducing the H1-O2 distance in the $\alpha_2\beta_2$ heterotetramer and the β monomer: (a) reactant (green carbon atoms) and structure after rotation of C1/H1 (yellow carbon atoms) from the $\alpha_2\beta_2$ heterotetramer; (b) reactant (green carbon atoms) and structure with similar O2-H1 distance to the heterotetramer structure after C1/H1 rotation. The difference in O2-H1 distance in each case is 1.1Å, corresponding to a C1-H1 bond stretching of (a) 0.17Å in and (b) 0.42Å.

after C1/H1 rotation further reveals the importance of C1/H1 rotation as a dynamical, rather than an equilibrium, effect. This is a fairly crude analysis, since only one reactant from each system is used, but it does illustrate why the orientation of C1/H1 in the β monomer leads to much larger activation energies. In Figure 5.31a, the O2-H1 and C1-H1 distances in the reactant are 2.52 and 1.15 Å respectively, and after rotation of the C1/H1 group 1.44 and 1.32 Å: C1-H1 is stretched by 0.17 Å and the O2-H1 distance reduced by 1.1 Å. The C1/H1 rotation is in this case accompanied by C1-H1 bond stretching, which, as discussed in Section 5.4, is not expected to begin until the C1-O2 distance is minimised. Here, the C1-H1 stretching is probably due to the manner in which the proton transfer is simulated by forcibly reducing z at each step of the reaction. It is interesting to note, however, that if this C1-H1 stretching is cancelled out, i.e. the C1-H1 bond is shortened by the stretching distance and the O2-H1 distance is increased by the same amount, the resulting O2-H1 distance is 1.61 Å, which is very close to 1.64Å distance for maximum tunneling in the VTST/MT calculations (C1-H1-O2 is not completely linear, but calculating a more accurate O2-H1 distance using trigonometry gives almost the same answer, 1.62Å). Therefore, the O2-H1 distance post C1/H1 rotation can be taken to be ~1.6 Å. This motion illustrated in Figure 32, Panel A.

In the β monomer reactant, the C1/H1 orientation is similar to that in the tunneling configuration of the $\alpha_2\beta_2$ heterotetramer. This means that C1-H1-O2 is roughly as linear as in the heterotetramer structure *after* rotation of C1/H1, and therefore the proton transfer distance cannot be reduced further by C1/H1 rotation. However, the maximum tunneling geometry [d(O2-H1) $\approx$ 1.6 Å] only exists momentarily, as it is a strained structure: the potential energy of this tunneling configuration is ~9 kcal/mol in the heterotetramer (Masgrau et al. 2006). In the $\alpha_2\beta_2$

heterotetramer, this strain is relieved by

C1/H1 rotating back to its equilibrium

position, away from O2, but in the β

monomer this cannot occur. Instead, the

strain is relieved by Asp128β moving

slightly away from the iminoquinone:

there is a noticeable difference in Figure

5.31 between the positions of Asp128β

in the $\alpha_2\beta_2$ heterotetramer and the β

monomer. This effect is illustrated in
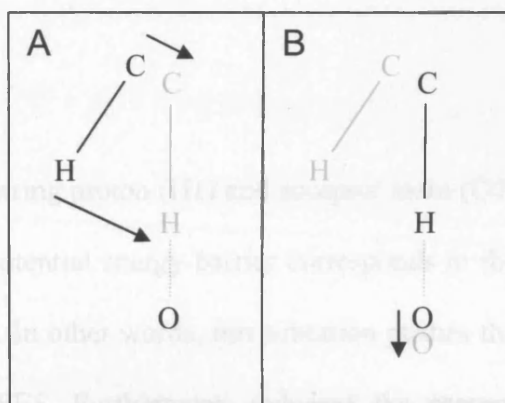
Fig 5.32. Effect of preventing the C1/H1 rotation (for simplicity, motion of O is ignored). **A.** The rotation pushes H so that it lies momentarily very close to O, thus facilitating proton transfer. **B.** C/H lie are in their "tunneling-ready configuration" but the O-H proximity pushes O away from H – tunneling will now require initial C-H bond stretching.

Figure 5.32, Panel B. This means that the C1/H1 rotation can only effectively reduce the proton transfer distance as a dynamical event. In other words the reactant structure and geometry is such that the reaction utilizes the softer bending mode associated with the C1/H1 rotation, rather than the stiffer C1-H1 stretching mode, to bring H1 closer to O2.

This analysis is a poignant illustration of the importance of dynamics for motion along the PES and for tunneling. In the $\alpha_2\beta_2$ heterotetramer, vibration of C1 (which is coupled to a vibration of O2 – see Chapter 4) pushes the system to the point of tunneling, but in the β monomer heavy atom motion cannot reduce the O2-H1 distance sufficiently. For tunneling to occur, initial C1-H1 bond stretching will therefore be required (Figure 5.31b), so this will not correspond to "extreme tunneling". This is consistent with the lower degree of tunneling in the β monomer than in the $\alpha_2\beta_2$ heterotetramer deduced from the kinetic data discussed in Section 3.6.

5.8. Conclusions

The motions of the donor atom (C1), transferring proton (H1) and acceptor atom (O2) that occur as the system moves along the potential energy barrier corresponds to the promoting vibration identified in Chapter 4. In other words, this vibration pushes the system along, instead of squeezing, the PES. Furthermore, reducing the proton-acceptor distance was shown to be sufficient to effectively reduce the barrier height, and therefore increase the probability of tunneling (as well as the chances of over-the-barrier transfer).

The role of Phe169β was elucidated by a combination of QM/MM simulations. This residue is important for product stabilization, which helps prevent back-reaction. However, it also seems to have the surprising effect of destabilising the transition state, and making it more difficult to achieve a tunneling configuration, by pushing against the acceptor atom. Therefore, evolution appears to have compromised between these two effects. Such a compromise might be more common for tunneling reactions than classical reactions, since tunneling itself is an instantaneous time-reversible process and therefore very rapid product stabilization is required.

The importance of the rotation of C1/H1 as a dynamical event was illustrated by comparing the PES and the corresponding atomic motions for proton transfer in the heterotatramer and in the β monomer. In the heterotetramer, this motion brings the proton-acceptor distance to ~1.6 Å, similar to the point of maximum tunneling in the VTST/MT calculations. In the monomer, this rotation is prevented, so that the lowest proton-acceptor distance cannot be sufficiently decreased by heavy atom motion. This means that greater C1-H1 bond stretching will be required to reach either a tunneling configuration or the transition state, and therefore the potential energy surfaces are

steeper and the activation energy is greater. These conclusions are consistent with

experimental data for the β monomer.

6. Numerical Modelling

6.1. Preface

Within the environmentally coupled hydrogen tunneling framework of Kuznetsov and Ulstrup (Kuznetsov and Ulstrup 1999), a promoting vibration or gating mode is taken to give rise to a temperature dependent KIE (Knapp and Klinman 2002). The KIEs observed in AADH (with multiple substrates) are, within the experimentally accessible temperature range and within experimental error, temperature independent (Basran et al. 2001; Masgrau et al. 2006), suggesting that tunneling in AADH is regulated by thermally equilibrated environmental reorganisation – passive dynamics in the environmentally coupled tunneling framework. While this appears at variance with the diagnosis of a $165 \, cm^{-1}$ promoting vibration (Chapter 4), modelling by Schwartz and co-workers suggests the possibility that a gating mode strongly coupled to the reaction coordinate can lead to a temperature independent KIE (Mincer and Schwartz 2004). Numerical modelling was carried out in collaboration with Dr Sam Hay to determine how the kinetic data for AADH with tryptamine relates to the framework of the Kuznetsov and Ulstrup model (Kuznetsov and Ulstrup 1999), and whether this is consistent with the results from the simulations.

6.2. AADH Within the Formalism of The Kuznetsov and Ulstrup Framework

The environmentally coupled tunneling model was implemented in a similar manner to that of Knapp and Klinman (Knapp et al. 2002). This model assumes that tunneling may occur either through a static barrier, with the tunneling configuration achieved via a passive reorganisation term – the Franck-Condon term – or a fluctuating barrier, where the Franck-Condon term is modified by a gating term (see Section 1.4.2). A

pre-requisite for this model is that the system involves extreme (or "deep") tunneling,

i.e. that the reaction proceeds entirely via tunneling. AADH therefore seems an ideal

candidate for this model, with 99.9% of proton transfers occurring by tunneling, ~43.5

kJ mol⁻¹ below the top of the barrier (Masgrau et al. 2006).

In the Kuznetsov and Ulstrup model, the rate of a tunneling reaction is given

by:

$$k_{tunnel} = (const.) \times \left[\exp\left\{ \frac{-(\Delta G^0 + \lambda)^2}{4\lambda RT} \right\} \right] \times (F.C.\ Term)$$

(6.1)

F.C. Term is the Frank-Condon nuclear overlap, which is different for a static barrier

and one modulated by gating; *const.* is an isotope-independent term; ΔG^0 is the free

energy driving force of the reaction (the difference in the Gibbs free energies of the

reactant and product); λ is the reorganisation energy; R is the universal gas constant

and T the temperature. The term in the square brackets is the Marcus term. The KIE

can be obtained from just the *F.C. Term*, since this is the only isotope dependent term,

and is strongly dependent on the tunneling distance. The ΔG^0 value has been obtained

from the VTST/MT calculations (Masgrau et al. 2006), and the reorganisation energy

can be obtained by fitting the above equation to the experimental rates – λ directly

impacts upon the temperature-dependence of the rates, i.e. $\Delta H^{\ddagger}$, the activation

enthanlpy. This means that any $\Delta H^{\ddagger}$ value can be accommodated by the model, and by

varying the const. term any magnitude of k_{tunnel} can be obtained. However, the key

question to be investigated with this numerical model is whether the experimental

KIE (55 ± 6) can be replicated with a tunneling distance that is consistent with that

from the VTST/MT calculations (Masgrau et al. 2006), using a static barrier and/or

gating, and whether the temperature-dependence of the KIEs ($\Delta\Delta H^{\ddagger} = \Delta H^{\ddagger D} - \Delta H^{\ddagger H}$)

obtained using a gating frequency of 165 cm^{-1} lies within the experimental error

($\Delta\Delta H^{\ddagger} \approx 0 \pm 5$ kJ/mol).

6.3. Modelling the Data With a Static Barrier

If there is no gating – i.e. tunneling occurs in a passive dynamics regime as suggested

by the seemingly temperature-independent KIEs – then the only isotope-dependent

term is the F.C. Term and the KIE can be calculated by:

$$KIE = k_H / k_D = F.C._H / F.C._D \tag{6.2}$$

$$F.C._{i} = \exp\left(- \mu_i \omega_i \Delta r^2 / 2\hbar\right) \tag{6.3}$$

where μ_i is the reduced mass, ω_i the angular frequency of the transferred isotope, and

Δr is the tunneling distance, i.e. the distance between the reactant and product wells at

the nuclear configuration compatible with tunneling. The *F.C. Term* assumes that the

proton is transferred from the vibrational ground state of the C1-H1 bond; this

assumption is not necessarily valid and is be addressed below. To simplify the

calculations, μ_i was calculated as the average C/O-H/D reduced mass

($\mu_H = 0.94$ g mol^{-1}, $\mu_D = 1.75$ g mol^{-1}), and ω_i as the average angular frequency ($\omega_H =$

5.65×10^{14} s^{-1}, $\omega_D = 4.14 \times 10^{14}$ s^{-1}) calculated from the stretching frequencies $f_H =$

3000 cm^{-1}; $f_D = 2200$ cm^{-1}. The KIE increases with Δr (Figure 6.1, Table 6.1) and a

KIE of 55 occurs when $\Delta r = 0.51$ Å. This value is significantly shorter than the

tunneling distance of 0.59 Å obtained from the VTST/MT calculations (Masgrau et al.

2006). The KIE is very sensitive to the tunneling distance, so even allowing for a KIE
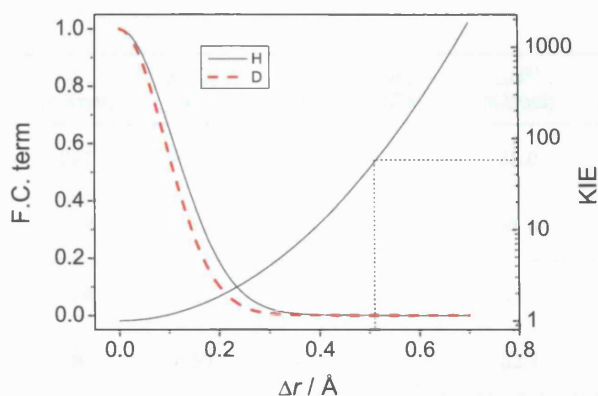
Figure 6.1. The Δr-dependence of the Franck-Condon terms for a static barrier (Equation 6.3) for hydrogen and deuterium, and the resulting KIE (Equation 6.2). The KIE is shown on a logarithmic scale; the Δr value corresponding to a KIE of 55 is represented by the dotted line.

of 60 the Δr value only increases to 0.52 Å. Therefore, while this model allows a good fit to the experimental data, it requires a tunneling distance that is significantly shorter than the computationally derived value. Since in this scenario there is no temperature-dependence on the KIE, if follows from the Arrhenius equation (Section 1.1.1) that the ratio of Arrhenius prefactors is $A_H/A_D = $ KIE $= 55$. The rates were calculated by:

$$k_{tunnel} = \left[\frac{1}{2\pi} |V_{el}|^2 \sqrt{4\pi^3 / \lambda RT\hbar^2} \right] \exp\left\{ \frac{-(\Delta G^0 + \lambda)^2}{4\lambda RT} \right\} \times (\text{F.C. Term}) \qquad (6.4)$$

The term in the square brackets is the complete form of the *const.* term in Equation 6.1; V_{el} is the isotope-independent electronic coupling constant, and was optimised to give the best fit to the experimental rates. The reorganisation energy, λ, was also estimated by fitting the data to the rate equation (Table 6.1, Figure 6.2) – altering λ directly affects the $\Delta H^{\ddagger}$ value.

	$-\Delta G^0$ (kJ/mol)	λ (kJ/mol)	$\Delta r / r_0$ $(\text{Å})^3$	ω_x (cm^{-1})	m_x (Da)	$\Delta H^{\ddagger H}$ (kJ/mol)	$\Delta H^{\ddagger D}$ (kJ/mol)	KIE (25 °C)
Static barrier[1]	32.6	297	0.51	-	-	55.0	55.0	55
	32.6	297	0.52	-	-	55.0	55.0	60
Static barrier[2]	32.6	288	0.52	-	-	53.1	54.2	55
	32.6	288	0.53	-	-	53.1	54.2	60
Gating	32.6	252	0.64	165	100	51.2	54.9	55
	32.6	252	0.65	165	100	51.2	55.0	60

Table 6.1. Parameters for modelling the experimental rates in AADH with tryptamine using the Kuznetsov and Ulstrup Environmentally Coupled Hydrogen Tunneling framework. The experimentally derived parameters are $\Delta H^{\ddagger H}$ = 57. 3 ± 3.4 kJ/mol, $\Delta H^{\ddagger D}$ = 53.5 ± 1.2 kJ/mol, KIE = 55 ± 6 and the computationally derived values are $-\Delta G^0$ = 32.6 kJ/mol and Δr = 0.59 Å (Masgrau et al. 2006).

[1] No contribution from excited states (Equation 6.3, 6.4).

[2] Contribution from the first reactant and product excited states.

[3] Δr values are given for the static barrier models, and r_0 for the gating model.
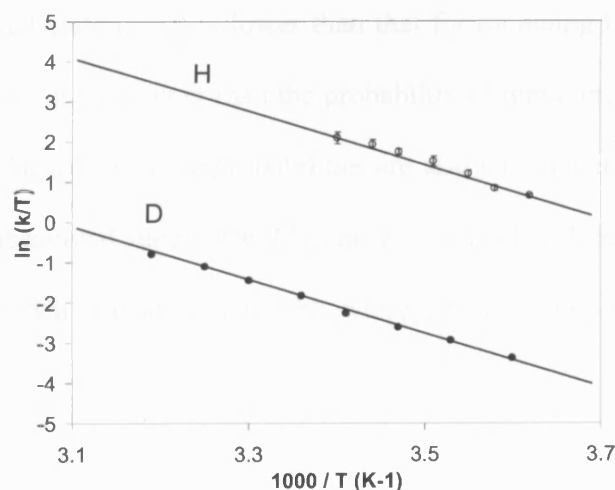
Figure 6.2. Modelling the experimental rates using a static barrier without contribution from excited states: Eyring plots for the model fitted to the experimental values for H and D.

To account for the possibility of tunneling from and/or to a vibrationally excited state (i.e. from the C1-H1 excited state and/or to a O2-H1 excited state), expressions for vibrational state specific Franck-Condon overlaps (Knapp et al. 2002) were employed. In each case, tunneling is assumed to occur between oscillators of equal frequencies.

$$F.C._{0,0} = \exp\left(-\mu\omega\Delta r^2 / 2\hbar\right) \tag{6.5}$$

$$F.C._{0,1} = \left(\mu\omega\Delta r^2 / 2\hbar\right) \times \exp\left(-\mu\omega\Delta r^2 / 2\hbar\right) \tag{6.6}$$

$$F.C._{1,0} = \left(\mu\omega\Delta r^2 / 2\hbar\right) \times \exp\left(-\mu\omega\Delta r^2 / 2\hbar\right) \tag{6.7}$$

$$F.C._{1,1} = \left(1 - \mu\omega\Delta r^2 / 2\hbar\right)^2 \times \exp\left(-\mu\omega\Delta r^2 / 2\hbar\right) \tag{6.8}$$

$F.C._{i,j}$ is the *F.C. Term* for tunneling from vibrational state i to vibrational state j. Note that only the first vibrationally excited states are included (the Boltzmann populations of the higher excited states are negligible). The probability of tunneling from a lower to a higher vibrational state ($i < j$) is lower than that for tunneling between the same states ($i = j$), which is in turn lower than the probability of tunneling from a higher to a lower state ($j > i$). However, these probabilities are also modulated by the likelihood of achieving each vibrational state i. The Marcus term must therefore be included, and the *F.C. Term* for each transition must be weighted according to its Boltzmann population (P_i):

$$KIE = \frac{k_H}{k_D} = \sum_i P_i \sum_j \frac{F.C._H}{F.C._D} \times \left[\exp\left\{\frac{-\left(\Delta G^0 + E_{vib} + \lambda\right)^2}{4\lambda RT}\right\}\right] \tag{6.8}$$

where E_{vib} is the difference in vibrational energy between the reactants and products: 0 when $i = j$, ±36.0 kJ/mol and ±26.3 kJ/mol for H and D, respectively, when $i \neq j$. E_{vib} reduces the probability of tunneling when $i < j$ and increases the probability when $i > j$. Again, the experimental data can be accommodated by this model (Table 6.1. and Figure 6.3), but the Δr value is at variance with the computationally derived value. In this case, the complete rate equation is (Knapp et al. 2002):

$$k_{tunnel} = \sum_i P_i \sum_i \frac{1}{2\pi} |V_{el}|^2 \sqrt{4\pi^3 / \lambda R T \hbar^2} \exp\left\{ \frac{-(\Delta G^0 + \lambda)^2}{4\lambda RT} \right\} \times (\text{F.C. Term}) \quad (6.9)$$

Because of the increased temperature-dependence ($\Delta\Delta H^{\ddagger} = \Delta H^{\ddagger D} - \Delta H^{\ddagger H} = 1.1$ kJ/mol) the A_H/A_D value in this case is decreased from 55 to 39.
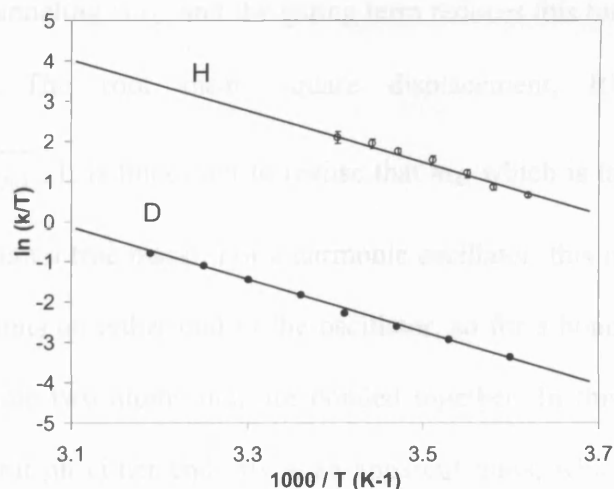
Figure 6.3. Modelling the experimental rates using a static barrier and contribution from excited states: Eyring plots for the modeled data fitted to the experimental values for H and D.

6.4. Modelling the Data With Gating

To incorporate gating, the F.C. term in Equation 6.4 is modified to:

$$F.C._{-i} = \int_0^{r_0} \exp\left(-\mu_i \omega_i \Delta r^2 / 2\hbar\right) \exp\left(-E_X / k_B T\right) \, dX \qquad (6.10)$$

$$E_X = \tfrac{1}{2}\hbar\omega_X X^2 \qquad (6.11)$$

The gating mode is treated as an isotope-independent harmonic oscillator with energy E_X. The frequency term ω_X is now the angular frequency of the gating motion along the reduced gating coordinate $X = r_X\sqrt{m_X\omega_X / \hbar}$. The gating "unit" has a mass, m_X, and a force constant, $k_{HO} = m_X\omega_X^2$. The tunneling distance at a nuclear configuration compatible with tunneling is r_0, and the gating term reduces this tunneling distance by r_X: $\Delta r = r_0 - r_X$. The root mean square displacement, RMSD, of r_X is:

$RMSD = \sqrt{k_B T / k_{HO}}$. It is important to realise that m_X, which is taken from Hooke's law of springs, is not a true mass. For a harmonic oscillator, this mass is the reduced mass of the two units on either end of the oscillator, so for a bond vibration it is the reduced mass of the two atoms that are bonded together. In this case, there is no "spring" with a unit on either end. m_X is an apparent mass, which relates the force constant of the oscillator to the observed frequency. In other words, the mass represents the amount of energy required for the oscillation to occur.

The solution for this model where KIE = 55 and ω_X = 165 cm^{-1} at a temperature of 298 K, with m_X = 100 Da is shown in Figure 6.4. This corresponds to a $\Delta\Delta H^{\ddagger}$ value of 3.7 kJ mol^{-1}, which lies within the experimental error ($\Delta\Delta H^{\ddagger} \approx 0 \pm 5$

kJ mol^{-1}), and an r_0 value of 0.64 Å. It should be noted that although this r_0 value is significantly shorter than the equilibrium well separation [d(O2-H1) = 2.67 Å (Masgrau et al. 2006)], this is reasonable since r_0 is not the equilibrium well separation but the separation at a nuclear configuration compatible with tunneling. Thermally equilibrated motions (e.g. the 100 cm^{-1} reorganisation discussed in Chapter 4), which are independent of the isotope, are required to bring the system to this configuration, where O2 is sufficiently close to H1 for electrostatic interactions to take effect – r_0 is the well separation at the point when the gating vibration becomes effective. Using the rate expression in Equation 6.3, a good fit to the experimental data was obtained using the *F.C. Term* for gating in Equation 6.10 (Figure 6.5).

For simplicity, the rate for the gating model does not include contributions from the excited state transitions, which have the effect of slightly increasing $\Delta\Delta H^{\ddagger}$. The contribution to $\Delta\Delta H^{\ddagger}$ from excited states is strongly dependent on Δr (Figure 6.6), and in the gating model $\Delta r \leq r_0$ so that the $\Delta\Delta H^{\ddagger}$ values from gating and excited states are not strictly additive. Nevertheless, the 'extreme' scenario would involve an additional ~1.5 kJ/mol contribution to $\Delta\Delta H^{\ddagger}$, i.e. $\Delta H^{\ddagger H}$ would be reduced by ~1.5 kJ/mol relative to $\Delta H^{\ddagger D}$ (Figure 6.7). Even with this contribution to $\Delta\Delta H^{\ddagger}$ the model can accommodate the experimental rates: this has a negligible effect on the slope of the Eyring plot (Figure 6.7). Note that this will have a small effect on the KIE, so r_0 will have to be readjusted slightly (the KIE is very strongly dependent on r_0, so the change in r_0 will be very small).
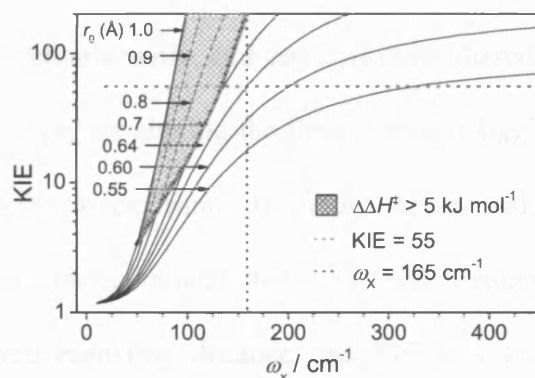
Figure 6.4. The effect of the gating frequency on the KIE at 298 K for a range of r_0 values, with m_X = 100 Da
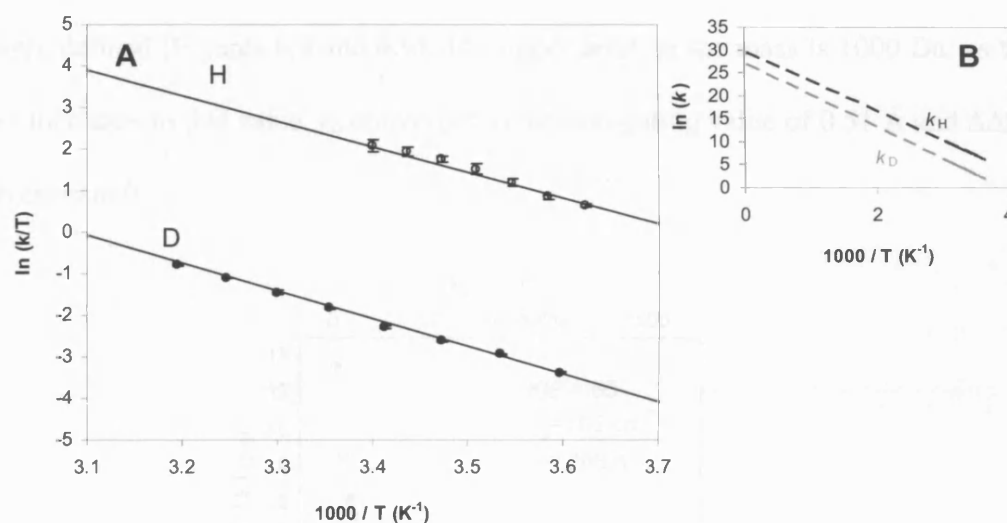
Figure 6.5. Modelling the experimental rates using a gating mode with ω_X = 165 cm^{-1} and m_X = 100 Da. **A.** Eyring plot for the model fitted to the experimental values for H (open circles) and D (closed circles). **B.** Arrhenius plots extrapolated to show the natural logarithms of the Arrhenius prefactors at the y-intercepts.
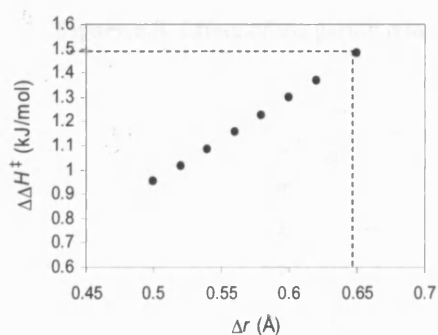
Figure 6.6. Effect of Δr on $\Delta\Delta H^{\ddagger}$ for tunneling through a static barrier with contributions from excited states.
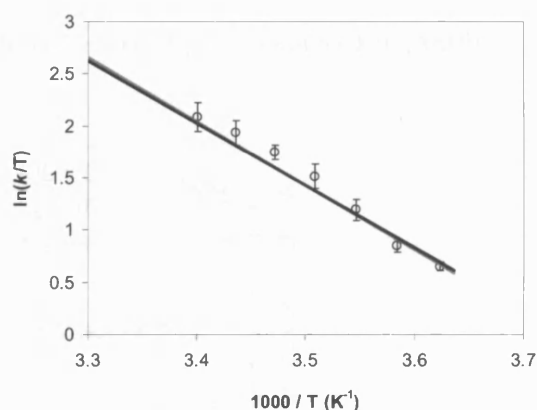
Figure 6.7. The effect of an increase of 1.5 kJ/mol to $\Delta\Delta H^{\ddagger}$ on the modeled k_H: the grey line shows k_H originally obtained from the model, and the black line k_H with a decrease of 1.5 kJ/mol in $\Delta H^{\ddagger}$; the experimental rates are also shown.

The mass m_X was selected arbitrarily, and can always be altered to accommodate any given frequency ω_X, simply by altering the force constant k_{HO}; however, this affects $\Delta\Delta H^{\ddagger}$ and r_0. Therefore, to determine the range of m_X values that fit with the experimental data and the computationally derived frequency as well as the computationally derived tunneling distance, the KIE was fixed at 55 and ω_X at 165 cm^{-1}, and k_{HO} was systematically altered (note: the temperature is fixed at 298 K). From these calculations, a lower limit of 70 Da for m_X and an upper limit of 0.7 Å for r_0 were defined (Figures 6.8 and 6.9). The upper limit on the mass is 1000 Da: as the mass increases to this value, r_0 converges to the non-gating value of 0.51 Å and $\Delta\Delta H^{\ddagger}$ converges to 0.
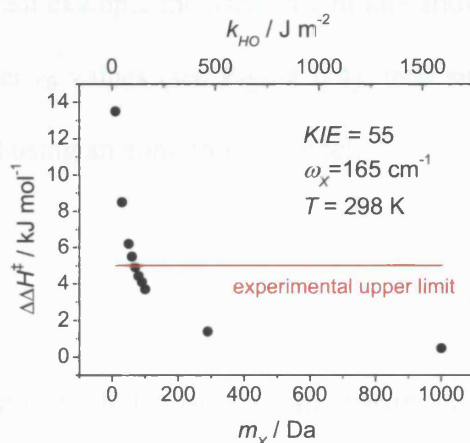
Figure 6.8. Effect of the gating mass on the temperature dependence of the KIE ($\Delta\Delta H^{\ddagger}$).
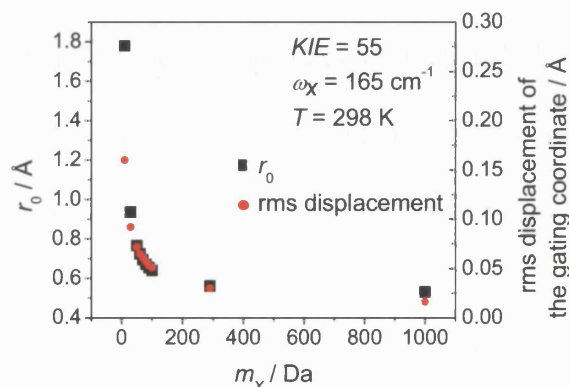
Figure 6.9. Effect of the gating mass on r_0 and the RMS displacement.

Gating reduces the tunneling distance by r_X. Therefore, taking $r_X \approx RMSD$ a m_X value of 100 Da gives r_0 and $RMSD$ values of 0.64 Å and 0.05 Å, respectively, which give a Δr value of 0.59 Å, consistent with the computationally derived tunneling distance (Masgrau et al. 2006). This mass is similar to that of 110 Da used by Klinman and co-workers, representing the average mass of an amino acid residue (Knapp et al. 2002; Meyer and Klinman 2005). The ratio of Arrhenius prefactors obtained is $A_H/A_D = 11.8$.

In a recent application of the Kuznetsov and Ulstrup model, the harmonic oscillator was replaced by a more accurate Morse potential, which had the effect, for a given KIE and $\Delta\Delta H^{\ddagger}$, of decreasing ω_X and increase r_0 (Meyer and Klinman 2005). However, in the current example the harmonic model allows both significantly higher frequencies and lower r_0 values (see Figure 6.4), thus similar ω_X and r_0 values can probably be obtained using an anharmonic model.

6.5. Conclusions

Modelling the experimental KIEs using a static barrier gives a value for Δr (0.51 Å), the tunneling distance when no gating is included, which is not compatible with the computationally derived tunneling distance (0.59 Å) (Masgrau et al. 2006). When tunneling from excited C-H vibrational states are included, the Δr value is increased slightly (0.52 Å), but because of the strong dependence of the KIEs on Δr, a reasonable value for Δr could not be obtained even when significantly increasing the KIEs. On the other hand a more realistic value for r_0 was obtained when a gating vibration of 165 cm^{-1} was incorporated. Therefore, within the Kuznetsov and Ulstrup framework, the gating frequency derived from the spectral density analysis and digital

filtering (Chapter 4) is compatible with both the computationally derived tunneling distance and the experimentally observed kinetics. From this numerical model, it transpires that gating can lead to very similar reaction kinetics to tunneling through a static barrier. For example, the ratio of Arrhenius prefactors is not necessarily a good indicator of the tunneling regime, since A_H/A_D is greater than 10 in each case. The large reorganisation energies, λ, obtained for each of the calculations, is in good agreement with a previously published value of 285 ± 4 kJ/mol for an enzymic hydride transfer (Brinkley and Roth 2005).

The experimental data for AADH with tryptamine – highly elevated, seemingly temperature-independent KIEs – is suggestive of tunneling in a passive dynamics regime. However, this is apparently inconsistent with the 165 cm^{-1} promoting vibration identified in Chapter 4, and numerical modelling suggests that the experimental data are in fact consistent with an active dynamics regime. Tunneling from an excited state is likely to contribute to the rate, although this will not strongly affect the temperature-dependence of the KIEs. Taken together, the experimental and computational data along with the numerical modelling are suggestive of tunneling promoted by active dynamics – gating – with the possibility of contributions from an excited C–H vibrational state.

7. Discussion

7.1. General Discussion

A short-range, sub-picosecond promoting vibration has been diagnosed at 165 cm^{-1}

for the proton tunneling step in the oxidative deamination of tryptamine by AADH,

which is similar to the substrate oscillations ($\leq$ 220 cm^{-1}) suggested by Schwartz and

co-workers almost a decade ago (Antoniou and Schwartz 1997), and the gating

frequencies of 150-200 cm^{-1} predicted by Kuznetsov and Ulstrup for ADH.

(Kuznetsov and Ulstrup 1999). It is also very similar to the 150 cm^{-1} promoting

vibration identified by Schwartz and co-workers in HLADH (Caratzoulas, Mincer et

al. 2002) This promoting vibration synchronously pushes the donor C1, transferring

proton H1 and acceptor O2 towards the point of tunneling, and is therefore

symmetrically coupled to the reaction coordinate as defined by the vectors connecting

the reactant to the representative tunneling structure (the RTE structure). This

vibration is the major vibration for C1/H1 (strongest low-frequency peak in the

velocity spectral densities), but not for O2 as this vibration arises in O2 only when O2

is sufficiently close for an electrostatic interaction between itself and H1 to take

effect. In other words, O2 will only participate in the promoting vibration vibration

once it is sufficiently close to H1. Another vibration at about 100 cm^{-1} has been

identified, which plays a significant role in reducing the donor-acceptor and proton-

acceptor distances, and hence the tunneling distance, and brings O2 to the point at

which it can participate in the promoting vibration. This vibration is not

symmetrically coupled to the reaction coordinate, and is therefore not a promoting

vibration in the sense of enhancing tunneling. Instead, this vibration corresponds to a

preorganisation of the active site which brings the system to a configuration from

which the promoting vibration can take effect. In this sense, the 165 cm^{-1} promoting

vibration corresponds to active, non-equilibrium dynamics, while the $100 \, cm^{-1}$ vibration is an example of passive, equilibrium dynamics.

A reduction in the tunneling distance has a greater effect on the tunneling probability of the deuteron than the proton, and therefore both vibrations might be expected to lead to temperature-dependent KIEs. However, the $100 \, cm^{-1}$ vibration can be thought of as a "switch" which activates the more rapid $165 \, cm^{-1}$ promoting vibration: if the population of the $100 \, cm^{-1}$ vibration were selectively increased, then this would increase the occurrence of a configuration from which the $165 \, cm^{-1}$ promoting vibration can take effect (r_0 in the Kuznetsov and Ulstrup model; see Chapter 6). This will increase the rate of the reaction, but not the KIE.

Both of these vibrations lead to a reduction in the transfer distance, and therefore the simple view that passive dynamics are involved in bringing the system to a degenerate state compatible with tunneling while a promoting vibration, or gating, then reduces the tunneling distance is not applicable here. In this case, the promoting vibration also has a significant effect on the reactant energy, pushing the imine nitrogen away from planarity while rotating C1/H1 towards O2, which corresponds to the system moving up the potential energy barrier (see Chapter 5). This also has the effect of bringing the secondary hydrogen on C1 more in-plane with the linker region, thus aiding the transition of C1 from the reactant (sp^3) to the product (sp^2). This further explains the preference for proton tunneling to O2: tunneling to O1 does not involve such a C1/H1 rotation, which means that the secondary hydrogen is significantly above the plane of the linker region during the proton transfer event.

It is tempting to assume that the existence of a promoting vibration suggests that the enzyme has evolved to utilise tunneling as part of the catalytic effect, but since it has not been demonstrated that tunneling is less extensive in solution, it is not

possible to comment on the role of tunneling in catalysis. However, this is not the question of interest here: in any case, the reaction rate will be far greater in the enzyme, which means that the probability of achieving successful proton transfers is greater in the enzyme. Therefore, regardless of the ratios of tunneling transfers to classical transfers in solution, the tunneling probability will be greater in the enzyme – 99.9% of enzymic proton transfers occur via tunneling (Masgrau, Roujeinikova et al. 2006). The primary question here is therefore how the enzyme promotes, not enhances (see Section 1.7), tunneling. As discussed in Chapter 5, reducing the H1-O2 distance reduces both the barrier height and width, while motion along the reaction coordinate, which corresponds to the 165 cm^{-1} promoting vibration, leads to motion up the barrier towards the point of tunneling.

The geometry of the donor group appears to be essential for the reaction. In the β monomer, the equilibrium orientation of C1/H1 resembles the momentary orientation of C1/H1 at the point of tunneling in the heterotetramer, following the rotation associated with the promoting vibration. However, this is actually detrimental to the proton transfer event: the reactant well in the isolated β monomer is far narrower and steeper than that in the heterotetramer, which means that motion along the reaction coordinate is more difficult, and reducing the O2-H1 distance requires additional C1-H1 bond stretching. This illustrates the importance of the C1/H1 rotation in promoting tunneling (as well as classical proton transfer) as a dynamical event, rather than an equilibrium reorganisation of the active site geometry.

The fact that the promoting vibration only involves a few atoms has important consequences for our perception of vibrationally coupled tunneling, since it means that this mechanism does not require extensive vibration of the protein scaffold to reconcile the temperature-dependence of the rates with the fact that the reaction

occurs via tunneling. Furthermore, while there is compelling evidence that certain enzymes do employ a large network of motions to assist the tunneling step, notably in dihydrofolate reductase (Radkiewicz and Brooks 2000; Agarwal, Billeter et al. 2002), and horse liver alcohol dehydrogenase (Mincer and Schwartz 2003; Mincer and Schwartz 2003), this result shows that this is in fact not necessary. Instead, in the case of AADH, the enzyme appears to have evolved to position the donor and acceptor groups such that the vibrations inherent in the donor group, which couples to the vibration of the acceptor atom, are focused in the direction required for proton transfer to occur.

The structure of the active site is clearly very important for the success of the proton transfer reaction – the quinone is held in place by multiple backbone hydrogen bonds, the indole ring is kept in the correct orientation by the proximity of hydrophobic residues from both the α and β subunits, and Asp128β is positioned by hydrogen bonding to the Thr102β sidechain and the Trp160β backbone. A more surprising observation was the role of active site residue Phe169β, which pushes against Asp128β O2 (Chapter 5, e.g. Figure 5.26a). By pushing against O2, it makes it more difficult for O2 to achieve the position required for tunneling to occur (Figure 4.5b), and in the unrestrained transition state simulation Phe169β rapidly changes conformation so that it moves away from O2. However, if Phe169β adopts this alternate conformation, the O2-Thr102β hydrogen bond is not broken as readily in the product (Section 5.5) and Asp128β cannot move away from C1, which has previously been suggested as a requirement for product stabilisation in MADH (Nunez, Tresadern et al. 2006). This is further supported by simulations of the proton transfer in the β monomer, where Phe169β has adopted this alternate conformation and the reaction is no longer exothermic. It therefore seems that there is a compromise

between Phe169β destabilising the transition state and stabilising the product. The role of this residue could be further elucidated by stopped-flow experiments on Phe169β mutants.

7.2. Relating to Tunneling in Other AADH and MADH Substrates

Kinetic data is available for the proton transfer in multiple AADH and MADH substrates (Basran, Sutcliffe et al. 1999; Basran, Patel et al. 2001; Masgrau, Basran et al. 2004; Masgrau, Roujeinikova et al. 2006), although tryptamine is the first for which computational analysis has diagnosed the role of dynamics in promoting the reaction. Nevertheless, it is possible to gain insight into the differences in kinetic data by comparing with the tryptamine data, although future computational analyses will be invaluable to understanding these variations.

The enthalpies of activation $(\Delta H^{\ddagger})$ for proto- and deutero-tryptamine are similar to those for dopamine, while those for benzylamine are elevated (Table 7.1).

Substrate	k_H (s^{-1}), 25 °C	KIE	$\Delta H^{\ddagger H}$ / kJ mol^{-1}	$\Delta H^{\ddagger D}$ / kJ mol^{-1}
Tryptamine[1]	~ 3500	54.7 ± 1.0	57.3 ± 3.4	53.5 ± 1.2
Dopamine[2]	132 ± 1.0	12.9 ± 0.2	50.9 ± 0.7	51.6 ± 0.7
β-phenylethylamine[3]	45.56 ± 0.3	15.3 ± 0.3	54.7 ± 0.6	54.3 ± 0.7
Benzylamine[3]	1.47 ± 0.01	4.7 ± 0.1	63.6 ± 0.6	65.0 ± 0.7
p-fluoro-benzylamine[3]	5.51 ± 0.04	6.08 ± 0.4	62.4 ± 0.7	65.4 ± 1.0
p-methoxy-benzylamine[3]	5.09 ± 0.04	5.03 ± 0.2	66.4 ± 0.5	69.7 ± 0.8

Table 7.1. Kinetic and thermodynamic parameters determined from stopped-flow reactions of AADH with protiated and deuterated substrates.
[1] Data taken from (Masgrau, Roujeinikova et al. 2006)
[2] Data taken from (Basran, Patel et al. 2001)
[3] Personal communication with Nigel S. Scrutton and Parvinder Hothi; work in progress.

This is consistent with a promoting vibration that arises from the flexibility around the donor carbon: dopamine shares the same linker region as tryptamine, whereas the donor carbon of benzylamine is directly bound to the benzyl ring (Figure 7.1). This means that rotation of the C1/H1 group will be coupled to motion of the benzyl ring. Of course, QM/MM calculations of the proton transfer step in benzylamine are necessary to confirm the requirement for a rotation of the benzyl ring.

More recently, kinetic data for β-phenylethylamine and various p-substituted benzylamines have become available[1] (Table 7.1). The KIEs for most of the p-substituted benzylamines are close to unity because the proton transfer step for these is not truly rate limiting. However, $\Delta H^{\ddagger}$ values for p-fluoro and p-methoxy-benzylamine (Table 7.1) reflect the reorganization energies associated with tunneling. Fluoro-substituted benzylamine has the same $\Delta H^{\ddagger}$ value (within experimental error) as benzylamine, while the methoxy-substitution caused a significant increase in the $\Delta H^{\ddagger}$ value. This is in accord with a promoting vibration that involves a C1/H1 rotation,
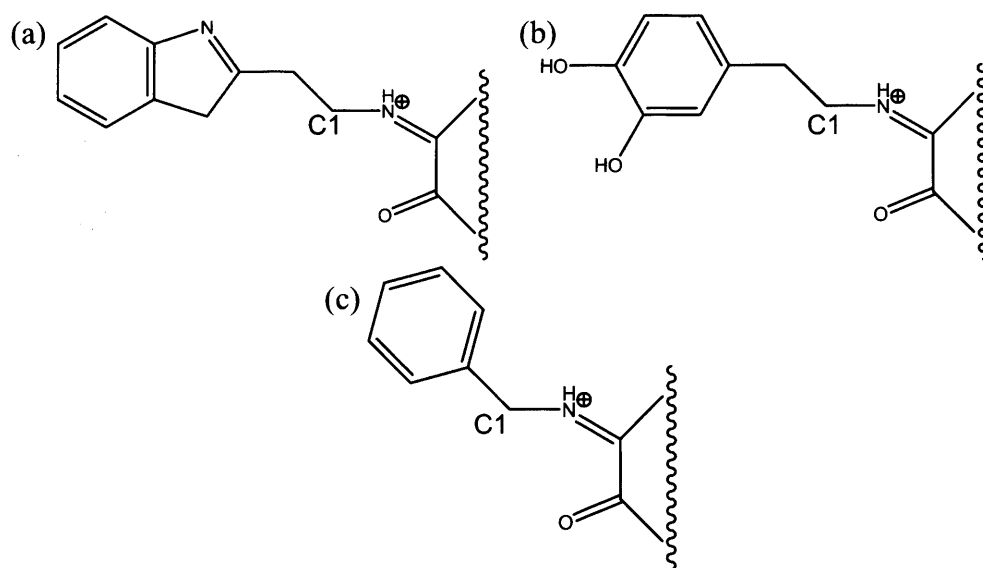
Figure 7.1. Iminoquinone adducts of (a) tryptamine, (b) dopamine and (c) benzylamine. C1 is the donor carbon in each case.

---

[1] Personal communication with Nigel S. Scrutton and Parvinder Hothi; work in progress.

since this rotation will require a repositioning of the benzyl ring and its substituent – fluorine is very similar in size to a hydrogen, while a methoxy group is significantly larger, thus making the necessary reorganization more difficult. On the other hand, $\Delta H^{\ddagger}$ for dopamine is slightly lower than that for β-phenylethylamine – the opposite trend than would be expected if motion of the phenyl ring was required for tunneling to occur. This can be explained by the flexible linker region which allows C1/H1 rotation to occur independently of the phenyl ring.

Further understanding of the different $\Delta H^{\ddagger}$ values will require QM/MM simulations of the proton transfer step. As previously mentioned (Section 1.5.1), the rates for the p-substituted benzylamines are strongly dependent on the inductive effect of the substituent, but this is not the case for β-phenylethylamine or dopamine, since the donor carbon is separated from the phenyl ring by one sp^3 carbon atom and is therefore not conjugated with the aromatic phenyl ring. For these substrates, spectral density analysis coupled with VTST/MT calculations will be invaluable for understanding why the rates are lower than those for tryptamine.

7.3. Comparing to Vibrationally Assisted Hydrogen Tunneling in Other Enzymes

The role of enzyme dynamics in vibrationally assisted hydrogen tunneling has been most extensively studied in DHFR (see Section 1.5.3). In this enzyme, strong cross-correlation corresponds to evolutionarily conserved residues (Radkiewicz and Brooks 2000), and motions of many of these, ranging from active site residues to distal residues on the enzyme surface, have been shown to be involved in the hydrogen tunneling step (Agarwal, Billeter et al. 2002). There is also evidence for the involvement of long-range dynamical effects in HLADH (Bahnson, Park et al. 1993;

Bahnson, Colby et al. 1997; Chin and Klinman 2000; Mincer and Schwartz 2003; Mincer and Schwartz 2003). The short-range promoting vibration in AADH is not consistent with these results; intuitively, one might expect similar degrees of protein involvement in the motions that promote tunneling in different enzymes. There are, however, significant differences between the tunneling reaction catalysed by AADH and those catalysed by DHFR and HLADH, which might explain the different scales of involvement of enzyme dynamics. It is worth mentioning that active-site mutations on soybean lipoxygenase-1 (SLO-1) have shed light on the role of dynamics in tunneling in this enzyme (Knapp and Klinman 2002; Knapp, Rickert et al. 2002), but these experiments do not offer direct evidence that the mutated residues are themselves dynamically involved, i.e. that the vibrations involved in the tunneling step extend beyond the donor / acceptor groups.

Perhaps the most obvious difference between the tunneling step in AADH and DHFR/HLADH is that, while they all involve the breaking of a carbon-hydrogen bond, the former involves transfer of a proton whereas the latter two involve transfer of a hydride. A proton transfer may be facilitated by withdrawal of electron density from the donor-hydrogen bond, which polarises and weakens this bond. In AADH, this effect is undertaken by the electron-poor iminoquinone, so that an electrostatic attraction or even a hydrogen-bond may form between the strongly polarised C1/H1 and the negatively charged O2, which helps couple the vibration of C1/H1 to O2. In DHFR/HLADH, the vibrations of the donor or acceptor groups will not be so readily coupled, because a hydride transfer cannot be facilitated by such an effect – a partial negative charge will not reside on the transferring hydrogen. Therefore, a promoting vibration will not arise from electrostatic interactions, and will instead require mechanical effects to drive the donor and acceptor groups together.
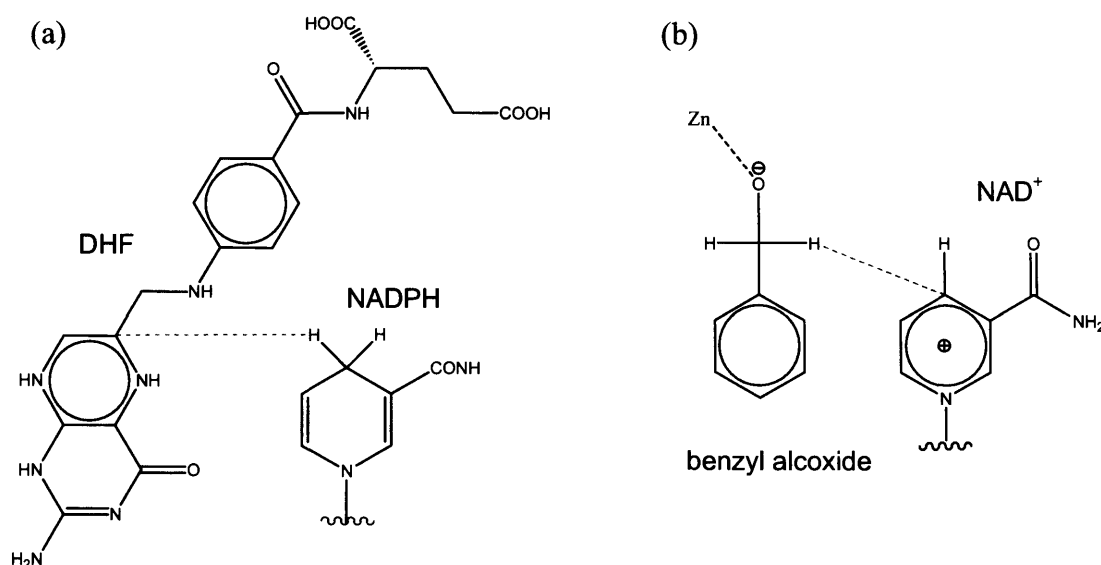
Figure 7.2. Hydride transfer schemes for (a) DHFR and (b) LADH. The grey dotted lines represent the hydride transfer.

The 165 cm^{-1} promoting vibration in AADH:tryptiminoquinone arises from the flexibility of the linker region connecting the indole and quinone. On the other hand, the substrates of DHFR and HLADH have less flexible donor and acceptor functional groups than the tryptiminoquinone: the hydride transfer in DHFR occurs between NADPH and DHF, and that in HLADH between benzyl alcoxide and NAD$^+$ (Figure 7.2). This means that a motion that reduces the transfer distance is more likely to involve the entire donor and/or acceptor moieties, driven by forces external to these moieties. The substrates in DHFR/HLADH are not covalently bound to the enzymes, as is the case in AADH, so that the donor and acceptor groups are replaced in subsequent catalytic cycles. In AADH, on the other hand, once the iminoquinone has been reduced, the electron gained is transferred to electron acceptor enzyme azurin. Because of this evolutionary pressure to successfully interact with azurin, and also the complexity of the overall mechanism of the reaction catalysed by AADH (Figure 1.8), it is less likely that AADH would have evolved to utilise large-scale motions to drive specifically the proton tunneling step.

7.4. Concluding Remarks and Future Perspectives

Using a combination of a variety of computational methods, the processes involved in promoting proton tunneling in AADH have been studied at the atomic level, and invaluable insight has been obtained into the precise nature of the mechanism. A gating mode has been identified, and its three dimensional characteristics have been studied. The effect of this gating mode on the potential energy barrier has been observed, as have the importance of the corresponding motions as a dynamical rather than an equilibrium effect. The role of the enzyme in promoting the tunneling event by reducing the tunneling distance appears to be, in this case, that of a stationary scaffold, holding the donor and acceptor groups in the correct orientation for the vibration inherent in the donor group to couple with the vibration of the acceptor. This is different to the long-range motions that have been identified in certain other enzymes, which emphasises how modest our understanding of the role of enzyme dynamics in hydrogen tunneling is, and how much further work in this field is necessary.

The identified gating mode fits well within the Kuznetsov and Ulstrup model for vibrationally assisted tunneling, although it appears that tunneling reactions governed by passive reorganisations can have very similar reaction kinetics, making it difficult to determine experimentally which tunneling regime – active or passive – is most prevalent. However, the results from the work presented in this thesis suggest a different, complementary approach to studying the role of enzymic vibrations in tunneling, using THz spectroscopy. By obtaining high resolution spectra for AADH with different substrates and different intermediates during the catalytic cycle, the modes important in the H-tunneling reaction could be identified. For example, by comparing a spectrum for AADH without substrate to one for AADH with bound

tryptamine, the vibrational frequencies within the tryptiminoquinone adduct can be identified. Specific vibrational frequencies can be excited using the THz radiation source during stopped-flow experiments (using so-called pump probe methods), to identify those modes that act as rate-promoting vibrations. For example, as previously discussed, the 100 cm^{-1} (3 THz) and 165 cm^{-1} (5 THz) vibrations are expected to be the two main rate-promoting modes in AADH with tryptamine, but exciting the 165 cm^{-1} vibration is expected to lead to the stronger temperature-dependence (although, as was discussed in Chapter 6, this temperature-dependence might not be experimentally observable). Furthermore, exciting specific vibrations – selective excitation – within the enzyme system could potentially provide a means of controlling enzyme activity with concomitant impact on the use of enzymes in biocatalysis. The hypothesised role of specific vibrations in AADH is about to be investigated experimentally (by the groups of Scrutton, Sutcliffe and Gardner) using the THz testing station at the Energy Recovery Linac prototype on the Synchrotron Radiation Source (SRS) at Daresbury. If these experiments prove successful, then this could pave the way for the development of new desktop applications for studying the role of enzyme dynamics in hydrogen tunneling reactions and potentially for exploiting enzymes by selectively exciting specific vibrations.

References

Agarwal, P. K., Billeter, S. R. and Hammes-Schiffer, S. (2002a). "Nuclear quantum effects and enzyme dynamics in dihydrofolate reductase catalysis." *J. Phys. Chem. B* **106**: 3283-3293.

Agarwal, P. K., Billeter, S. R., Rajagopalan, P. T., Benkovic, S. J. and Hammes-Schiffer, S. (2002). "Network of coupled promoting motions in enzyme catalysis." *Proc. Natl. Acad. Sci. U S A* **99**: 2794-2799.

Alhambra, C., Sanchez, M. L., Corchado, J., Gao, J. L. and Truhlar, D. G. (2001). "Quantum mechanical tunneling in methylamine dehydrogenase." *Chem. Phys. Lett.* **347**: 512-518.

Antoniou, D., Abolfath, M. R. and Schwartz, S. D. (2004). "Transition path sampling study of classical rate-promoting vibrations." *J. Chem. Phys.* **121**: 6442-6447.

Antoniou, D., Caratzoulas, S., Kalyanaraman, C., Mincer, J. S. and Schwartz, S. D. (2002). "Barrier passage and protein dynamics in enzymatically catalyzed reactions." *Eur. J. Biochem.* **269**: 3103-3112.

Antoniou, D. and Schwartz, S. D. (1997). "Large kinetic isotope effects in enzymatic proton transfer and the role of substrate oscillations." *Proc. Natl. Acad. Sci. U. S. A.* **94**: 12360-12365.

Bahnson, B. J., Colby, T. D., Chin, J. K., Goldstein, B. M. and Klinman, J. P. (1997). "A link between protein structure and enzyme catalyzed hydrogen tunneling." *Proc Natl Acad Sci U S A* **94**: 12797-802.

Bahnson, B. J., Park, D. H., Kim, K., Plapp, B. V. and Klinman, J. P. (1993). "Unmasking of hydrogen tunneling in the horse liver alcohol dehydrogenase reaction by site directed mutagenesis." *Biochemistry* **32**: 5503-5507.

Ball, P. (2004). "Enzymes: by chance, or by design?" *Nature* **431**: 396-397.

Basner, J. E. and Schwartz, S. D. (2005). "How enzyme dynamics helps catalyze a reaction in atomic detail: A transition path sampling study." *Journal of the American Chemical Society* **127**: 13822-13831.

Basran, J., Patel, S., Sutcliffe, M. J. and Scrutton, N. S. (2001). "Importance of barrier shape in enzyme-catalyzed reactions - Vibrationally assisted hydrogen tunneling in tryptophan tryptophylquinone-dependent amine dehydrogenases." *J. Biol. Chem.* **276**: 6234-6242.

Basran, J., Sutcliffe, M. J. and Scrutton, N. S. (1999). "Enzymatic H-transfer requires vibration-driven extreme tunneling." *Biochemistry* **38**: 3218-3222.

Bell, R. P. (1980). The application of tunnel corrections in chemical kinetics. The Tunnel Effect in Chemistry. London, Chapman and Hall: 51-140.

Bennet, W. S. and Steitz, T. A. (1978). "Glucose-induced conformational change in yeast hexokinase." *Proc. Natl. Acad. Sci. USA* **75**: 4848–4852.

Berendsen, H. J. C., Postma, J. P. M., van Gunsteren, W. F., DiNola, A. and Haa, J. R. (1984). "Molecular dynamics with coupling to an external bath." *J Chem Phys* **81**: 3684-3690.

Boyd, R. H. (1968). "Method for Calculation of the Conformation of Minimum Potential-Energy and Thermodynamic Functions of Molecules from Empirical Valence-Force Potentials—Application to the Cyclophanes." *J Phys Chem* **49**: 2574-2583.

Brinkley, D. W. and Roth, J. P. (2005). "Determination of a large reorganization energy barrier for hydride abstraction by glucose oxidase." *J Am Chem Soc* **127**: 15720-1.

Brooks, B. R., Bruccoleri, R. E., Olafson, B. D., States, D. J., Swaminathan, S. and Karplus, M. (1983). "CHARMM - a program for macromolecular energy, minimization, and dynamics calculations." *J. Comput. Chem.* **4**: 187-217.

Brooks, H. B., Jones, L. H. and Davidson, V. L. (1993). "Deuterium kinetic isotope effect and stopped-flow kinetic-studies of quinoproptein methylamine dehydrogenase." *Biochemistry* **32**: 2725-2729.

Bruno, W. J. and Bialek, W. (1992). "Vibrationally enhanced tunneling as a mechanism for enzymatic hydrogen transfer." *Biophys. J.* **63**: 689-699.

Caldin, E. F. (1969). "Tunneling in Proton-Transfer Reactions in Solution." *Chem. Rev.* **69**: 135-156.

Caratzoulas, S., Mincer, J. S. and Schwartz, S. D. (2002). "Identification of a protein-promoting vibration in the reaction catalyzed by horse liver alcohol dehydrogenase." *J. Am. Chem. Soc.* **124**: 3270-3276.

Caratzoulas, S. and Schwartz, S. D. (2001). "A computational method to discover the existence of promoting vibrations for chemical reactions in condensed phases." *J. Chem. Phys.* **114**: 2910-2918.

Careri, G. (1974). Quantum Statistical Mechanics in the Natural Sciences. New York, Plenum.

Cha, Y., Murray, C. J. and Klinman, J. P. (1989). "Hydrogen tunneling in enzyme reactions." *Science* **243**: 1325-1330.

Chen, J. T., Taira, K., Tu, C. P. D. and Benkovic, S. J. (1987). "Probing the Functional-Role of Phenylalanine-31 of Escherichia- Coli Dihydrofolate-Reductase by Site-Directed Mutagenesis." *Biochemistry* **26**: 4093-4100.

Chin, J. K. and Klinman, J. P. (2000). "Probes of a role for remote binding interactions on hydrogen tunneling in the horse liver alcohol dehydrogenase reaction." *Biochemistry* **39**: 1278-84.

Chistoserdov, A. Y., Tsygankov, Y. D. and Lidstrom, M. E. (1990). "Cloning and sequencing of the structural gene for the small subunit of methylamine dehydrogenase from Methylobacterium extorquens AM1: evidence for two tryptophan residues involved in the active center." *Biochem Biophys Res Commun* **172**: 211-6.

Cornell, W. D., Cieplak, P., Bayly, C. I., Gould, I. R., Merz, K. M., Ferguson, D. M., Spellmeyer, D. C., Fox, T., Caldwell, J. W. and Kollman, P. A. (1996). "A second generation force field for the simulation of proteins, nucleic acids, and organic molecules." *J Am Chem Soc* **117**: 5179-5197.

Dewar, M. J. S., Zoebisch, E. G., Healy, E. F. and Stewart, J. J. P. (1985). "The development and use of quantum-mechanical molecular-models.76. AM1 - a new general-purpose quantum-mechanical molecular- model." *J. Am. Chem. Soc.* **107**: 3902-3909.

Dogonadze, R. R. and Kuznetsov, A. M. (1977). "Conformational dynamics in biological electron and atom transfer reactions." *J Theor Biol* **69**: 239-63.

Doll, K. M., Bender, B. R. and Finke, R. G. (2003). "The first experimental test of the hypothesis that enzymes have evolved to enhance hydrogen tunneling." *J. Am. Chem. Soc.* **125**: 10877-10884.

Doll, K. M. and Finke, R. G. (2003). "A compelling experimental test of the hypothesis that enzymes have evolved to enhance quantum mechanical tunneling in hydrogen transfer reactions: The beta-neopentylcobalamin system combined with prior adocobalamin data." *Inorg. Chem.* **42**: 4849-4856.

Farnum, M. F., Magde, D., Howell, E. E., Hirai, J. T., Warren, M. S., Grimsley, J. K. and Kraut, J. (1991). "Analysis of hydride transfer and cofactor fluorescence decay in mutants of dihydrofolate reductase: possible evidence for participation of enzyme molecular motions in catalysis." *Biochemistry* **30**: 11567-11579.

Field, M. J., Bash, P. A. and Karplus, M. (1990). "A combined quantum-mechanical and molecular mechanical potential for molecular-dynamics simulations." *J. Comput. Chem.* **11**: 700-733.

Fischer, E. (1894). "Einfluss der Configuration auf die Wirkung den Enzyme." *Ber. Dtsch. Chem. Ges.* **27**: 2985–2993.

Frisch, M. J., Trucks, G. W., Schlegel, H. B., Scuseria, G. E., Robb, M. A., Cheeseman, J. R., Zakrzewski, V. G., J. A. Montgomery, J., Stratmann, R. E., Burant, J. C., Dapprich, S., Millam, J. M., Daniels, A. D., Kudin, K. N., Strain, M. C., Farkas,

O., Tomasi, J., Barone, V., Cossi, M., Cammi, R., Mennucci, B., Pomelli, C., Adamo, C., Clifford, S., Ochterski, J., Petersson, G. A., Ayala, P. Y., Cui, Q., Morokuma, K., Rega, N., Salvador, P., Dannenberg, J. J., Malick, D. K., Rabuck, A. D., Raghavachari, K., Foresman, J. B., Cioslowski, J., Ortiz, J. V., Baboul, A. G., Stefanov, B. B., Liu, G., Liashenko, A., Piskorz, P., Komaromi, I., Gomperts, R., Martin, R. L., Fox, D. J., Keith, T., Al-Laham, M. A., Peng, C. Y., Nanayakkara, A., Challacombe, M., Gill, P. M. W., Johnson, B., Chen, W., Wong, M. W., Andres, J. L., Gonzalez, C., Head-Gordon, M., Replogle, E. S. and Pople, J. A. (2002). Gaussian 98. Pittsburgh PA, Gaussian, Inc.

Garcia-Viloca, M., Alhambra, C., Truhlar, D. G. and Gao, J. (2001). "Inclusion of quantum-mechanical vibrational energy in reactive potentials of mean force." *J. Chem. Phys.* **114**: 9953-9958.

Garcia-Viloca, M., Truhlar, D. G. and Gao, J. L. (2003). "Importance of substrate and cofactor polarization in the active site of dihydrofolate reductase." *J. Mol. Biol.* **327**: 549-560.

Govindaraj, S., Eisenstein, E., Jones, L. H., Sanders-Loehr, J., Chistoserdov, A. Y., Davidson, V. L. and Edwards, S. L. (1994). "Aromatic amine dehydrogenase, a second tryptophan tryptophylquinone enzyme." *J. Bacteriol.* **176**: 2922-2929.

Grant, K. L. and Klinman, J. P. (1989). "Evidence that protium and deuterium undergo significant tunneling in the reaction catalyzed by bovine serum amine oxidase." *Biochemistry* **28**: 6597-6605.

Haldane, J. B. S. (1930). Enzymes. London, Longmans, Green.

Hockney, R. W. and Eastwood, J. W. (1981). Computer Simulations Using Particles. New York, McGraw-Hill.

Hohenberg, P. and Kohn, W. (1964). "Inhomogeneous Electron Gas." *Phys. Rev.* **136**: B864-B871.

Hur, S. and Bruice, T. C. (2003). "Enzymes do what is expected (chalcone isomerase versus chorismate mutase)." *Journal of the American Chemical Society* **125**: 1472-1473.

Hwang, J. K. and Warshel, A. (1996). "How important are quantum mechanical nuclear motions in enzyme catalysis?" *J. Am. Chem. Soc.* **118**: 11745-11751.

Hyun, Y. L. and Davidson, V. L. (1995). *Biochim. Biophys. Acta* **1251**: 198-200.

Iwaki, M., Yagi, T., Horiike, K., Saeki, Y., Ushijima, T. and Nozaki, M. (1983). "Crystallization and properties of aromatic amine dehydrogenase from Pseudomonas sp." *Arch Biochem Biophys* **220**: 253-62.

Jencks, W. P. (1975). "Binding energy, specificity and enzymatic catalysis: the circe effect." *Adv. Enymol.* **43**: 219-310.

Jensen, F. (2001). Introduction to Computational Chemistry. Chichester, UK, John Wiley & Sons.

Karplus, M. and McCammon, J. A. (1983). "Dynamics of proteins: elements and function." *Annu Rev Biochem* **52**: 263-300.

Kim, H. S., Damo, S. M., Lee, S. Y., Wemmer, D. and Klinman, J. P. (2005). "Structure and hydride transfer mechanism of a moderate thermophilic dihydrofolate reductase from Bacillus stearothermophilus and comparison to its mesophilic and hyperthermophilic homologues." *Biochemistry* **44**: 11428-39.

Kim, Y. H. and Kreevoy, M. M. (1992). "The Experimental Manifestations of Corner-Cutting Tunneling." *J. Am. Chem. Soc.* **114**: 7116-7123.

Knapp, M. J. and Klinman, J. P. (2002). "Environmentally coupled hydrogen tunneling. Linking catalysis to dynamics." *Eur. J. Biochem.* **269**: 3113-3121.

Knapp, M. J., Rickert, K. and Klinman, J. P. (2002). "Temperature-dependent isotope effects in soybean lipoxygenase- 1: Correlating hydrogen tunneling with protein dynamics." *J. Am. Chem. Soc.* **124**: 3865-3874.

Kohen, A., Cannio, R., Bartolucci, S. and Klinman, J. P. (1999). "Enzyme dynamics and hydrogen tunnelling in a thermophilic alcohol dehydrogenase." *Nature* **399**: 496-499.

Kohen, A. and Klinman, J. (2000). *J. Am. Chem. Soc.* **122**: 10738-10739.

Kohen, A. and Klinman, J. P. (1999). "Hydrogen tunneling in biology." *Chem. Biol.* **6**: R191-R198.

Kohn, W. and Sham, L. J. (1965). "Self-Consistent Equations Including Exchange and Correlation Effects." *Phys. Rev.* **140**: A1133-A1138.

Koshland, D. E. J. (1973). "Protein and biological control." *Sci. Am.* **229**: 52-64.

Kraut, J. (1988). "How do enzymes work?" *Science* **242**: 533-540.

Kuznetsov, A. M. and Ulstrup, J. (1999). "Proton and hydrogen atom tunnelling in hydrolytic and redox enzyme catalysis." *Can. J. Chem.* **77**: 1085-1096.

Lad, C., Williams, N. H. and Wolfenden, R. (2003). "The rate of hydrolysis of phosphomonoester dianions and the exceptional catalytic proficiencies of protein and inositol phosphatases." *Proc Natl Acad Sci U S A* **100**: 5607-10.

Leach, A. R. (2001). Molecular Modeling: Principles and Applications. Englewood Cliffs, NJ, Prentice-Hall.

Lewars, E. (2003). Computational Chemistry: Introduction to the Theory and Applications of Molecular and Quantum Mechanics. London, Kluwer Academic Press.

MacKerell, A. D., Bashford, D., Bellott, M., Dunbrack, R. L., Evanseck, J. D., Field, M. J., Fischer, S., Gao, J., Guo, H., Ha, S., Joseph-McCarthy, D., Kuchnir, L., Kuczera, K., Lau, F. T. K., Mattos, C., Michnick, S., Ngo, T., Nguyen, D. T., Prodhom, B., Reiher, W. E., Roux, B., Schlenkrich, M., Smith, J. C., Stote, R., Straub, J., Watanabe, M., Wiorkiewicz-Kuczera, J., Yin, D. and Karplus, M. (1998). "All-atom empirical potential for molecular modeling and dynamics studies of proteins." *J. Phys. Chem. B* **102**: 3586-3616.

Maglia, G. and Allemann, R. K. (2003). "Evidence for environmentally coupled hydrogen tunneling during dihydrofolate reductase catalysis." *J Am Chem Soc* **125**: 13372-3.

Marcus, R. A. and Sutin, N. (1985). "Electron Transfers in Chemistry and Biology." *Biochim. Biophys. Acta* **811**: 265-322.

Masgrau, L., Basran, J., Hothi, P., Sutcliffe, M. J. and Scrutton, N. S. (2004). "Hydrogen tunneling in quinoproteins." *Arch. Biochem. Biophys.* **428**: 41-51.

Masgrau, L., Roujeinikova, A., Johannissen, L. O., Hothi, P., Basran, J., Ranaghan, K. E., Mulholland, A. J., Sutcliffe, M. J., Scrutton, N. S. and Leys, D. (2006). "Atomic Description of an Enzyme Reaction Dominated by Tunneling." *Science* **312**: 237-241.

McQuarrie, D. A. (2000). Statistical Mechanics. Sausalito, CA, University Science Books.

Melander, L. and Sauders, W. H. (1980). Reaction Rates of Isotopic Molecules. New York, John Wiley & Sons.

Meyer, M. P. and Klinman, J. P. (2005). "Modeling temperature dependent kinetic isotope effects for hydrogen transfer in a series of soybean lipoxygenase mutants: The effect of anharmonicity upon transfer distance." *Chem. Phys.* **319**: 283-296.

Mincer, J. S. and Schwartz, S. D. (2003). "A computational method to identify residues important in creating a protein promoting vibration in enzymes." *J. Phys. Chem. B* **107**: 366-371.

Mincer, J. S. and Schwartz, S. D. (2003). "Protein promoting vibrations in enzyme catalysis--a conserved evolutionary motif." *J Proteome Res* **2**: 437-9.

Mincer, J. S. and Schwartz, S. D. (2004). "Rate-promoting vibrations and coupled hydrogen–electron transfer reactions in the condensed phase: A model for enzymatic catalysis." *J. Chem. Phys.* **120**: 7755-7760.

Nunez, S., Antoniou, D., Schramm, V. L. and Schwartz, S. D. (2004). "Promoting vibrations in human purine nucleoside phosphorylase. A molecular dynamics and hybrid quantum mechanical/molecular mechanical study." *Journal of the American Chemical Society* **126**: 15720-15729.

Nunez, S., Tresadern, G., Hillier, I. H. and Burton, N. A. (2006). "An analysis of reaction pathways for proton tunnelling in methylamine dehydrogenase." *Phil. Trans. R. Soc. B.* **361**: 1387.

Pauling, L. (1948). "The nature of forces between large molecules of biological interest." *Nature* **161**: 707-709.

Pechukas, P. (1981). "Transition-State Theory." *Annual Review of Physical Chemistry* **32**: 159-177.

Pu, J. Z., Ma, S. H., Gao, J. L. and Truhlar, D. G. (2005). "Small temperature dependence of the kinetic isotope effect for the hydride transfer reaction catalyzed by Escherichia coli dihydrofolate reductase." *J. Phys. Chem. B* **109**: 8551-8556.

Radkiewicz, J. L. and Brooks, C. L. (2000). "Protein dynamics in enzymatic catalysis: Exploration of dihydrofolate reductase." *J. Am. Chem. Soc.* **122**: 225-231.

Rajagopalan, P. T., Lutz, S. and Benkovic, S. J. (2002). "Coupling interactions of distal residues enhance dihydrofolate reductase catalysis: mutational effects on hydride transfer rates." *Biochemistry* **41**: 12618-12628.

Rickert, K. W. and Klinman, J. P. (1999). "Nature of hydrogen transfer in soybean lipoxygenase 1: separation of primary and secondary isotope effects." *Biochemistry* **38**: 12218-12228.

Romesburg, F. E. and Schowen, R. L. (2005). Advances in Physical Organic Chemistry. New York, Elsevier.

Scrutton, N. S., Basran, J. and Sutcliffe, M. J. (1999). "New insights into enzyme catalysis: ground state tunnelling driven by protein dynamics." *Eur. J. Biochem.* **264**: 666-671.

Sessions, R. B., Dauber-Osguthorpe, P. and Osguthorpe, D. J. (1989). "Filtering molecular dynamics trajectories to reveal low-frequency collective motions: phospholipase A2." *J Mol Biol* **210**: 617-33.

Siebrand, W. and Smedarchina, Z. (2004). "Temperature dependence of kinetic isotope effects for enzymatic carbon-hydrogen bond cleavage." *J. Phys. Chem. B* **108**: 4185-4195.

Siegbahn, P. E. (2003). "Mechanisms of metalloenzymes studied by quantum chemical methods." *Q Rev Biophys* **36**: 91-145.

Sikorski, R. S., Wang, L., Markham, K. A., Rajagopalan, P. T., Benkovic, S. J. and Kohen, A. (2004). "Tunneling and coupled motion in the Escherichia coli dihydrofolate reductase catalysis." *J Am Chem Soc* **126**: 4778-9.

Stewart, J. J. P. (1989). "Optimization of Parameters for Semiempirical Methods.1. Method." *J. Comput. Chem.* **10**: 209-220.

Sumi, H. and Ulstrup, J. (1988). "Dynamics of Protein Conformational Fluctuation in Enzyme Catalysis with Special Attention to Proton Transfers in Serine Proteinases." *Biochimica Et Biophysica Acta* **955**: 26-42.

Swaminathan, S., Harte, W. E. and Beveridge, D. L. (1991). "Investigation of Domain-Structure in Proteins Via Molecular-Dynamics Simulation - Application to Hiv-1 Protease Dimer." *J. Am. Chem. Soc.* **113**: 2717-2721.

Tresadern, G., Wang, H., Faulder, P. F., Burton, N. A. and Hillier, I. H. (2003). "Extreme tunnelling in methylamine dehydrogenase revealed by hybrid QM/MM calculations: potential energy surface profile for methylamine and ethanolamine substrates and kinetic isotope effect values." *Mol. Phys.* **101**: 2775–2784.

Truhlar, D. G., Garrett, B. C. and Klippenstein, S. J. (1996). "Current status of transition-state theory." *J. Phys. Chem.* **100**: 12771-12800.

Truhlar, D. G., Isaacson, A. D. and Garret, B. C. (1985). Generalized Transition State Theory. Theory of Chemical Reaction Dynamics. M. Baer. Boca Raton, FL, CRC Press. **IV**: 65-136.

van Gunsteren, W. F. and Berendsen, H. J. C. (1987). Groningen Molecular Simulation (GROMOS) Library Manual. Groningen, The Netherlands.

Warshel, A. (1991). Computer Modeling of Chemical Reactions in Enzymes and Solutions. New York, John Wiley & Sons.

Wiberg, K. B. (1965). "A Scheme for Strain Energy Minimization - Application to Cycloalkanes." *J Am Chem Soc* **87**: 1070-1078.

Wolfenden, R. and Snider, M. J. (2001). "The depth of chemical time and the power of enzymes as catalysts." **34**: 938-945.

Wu, N., Mo, Y. R., Gao, J. L. and Pai, E. F. (2000). "Electrostatic stress in catalysis: Structure and mechanism of the enzyme orotidine monophosphate decarboxylase." *Proceedings of the National Academy of Sciences of the United States of America* **97**: 2017-2022.

Publications

At the time of submission, the work presented in this thesis has contributed to the following publications:

Sutcliffe, M. J., Masgrau, L., Roujeinikova, A., Johannissen, L. O., Hothi, P., Basran, J., Ranaghan, K. E., Mulholland, A. J., Leys, D. and Scrutton, N. S. (2006). "Hydrogen tunnelling in enzyme-catalysed H-transfer reactions: flavoprotein and quinoprotein systems." *Philos. Trans. R. Soc. Lond. B. Biol. Sci.* **361**(1472): 1375-86.

Masgrau, L., A. Roujeinikova, L. O. Johannissen, P. Hothi, J. Basran, K. E. Ranaghan, A. J. Mulholland, M. J. Sutcliffe, N. S. Scrutton and D. Leys (2006). "Atomic Description of an Enzyme Reaction Dominated by Tunneling." *Science* **312**: 237-241.

Johannissen, L. O., Hay, S., Scrutton, N. S., Sutcliffe, M. J. (2006), "Proton Tunneling in Aromatic Amine Dehydrogenase is Driven by a Short-Range Sub-Picosecond Promoting Vibration: Consistency of Simulations and Theory with Experiment", *Submitted to J. Phys. Chem. B.*